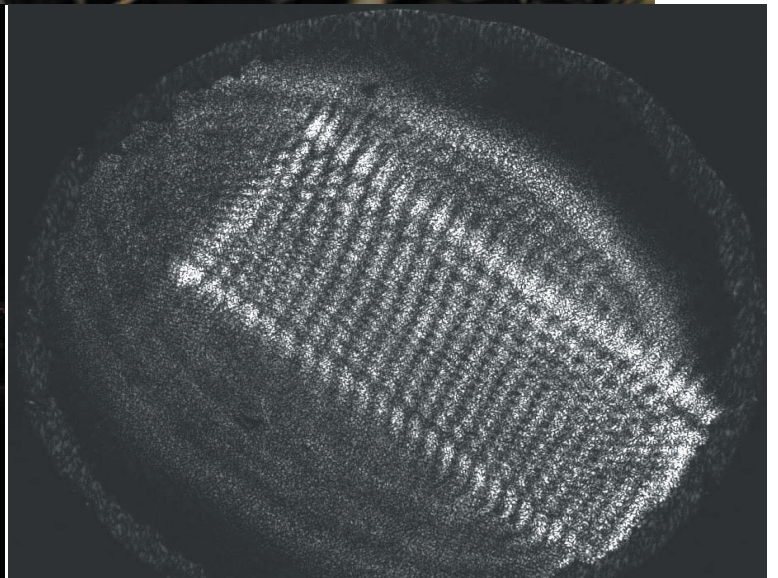
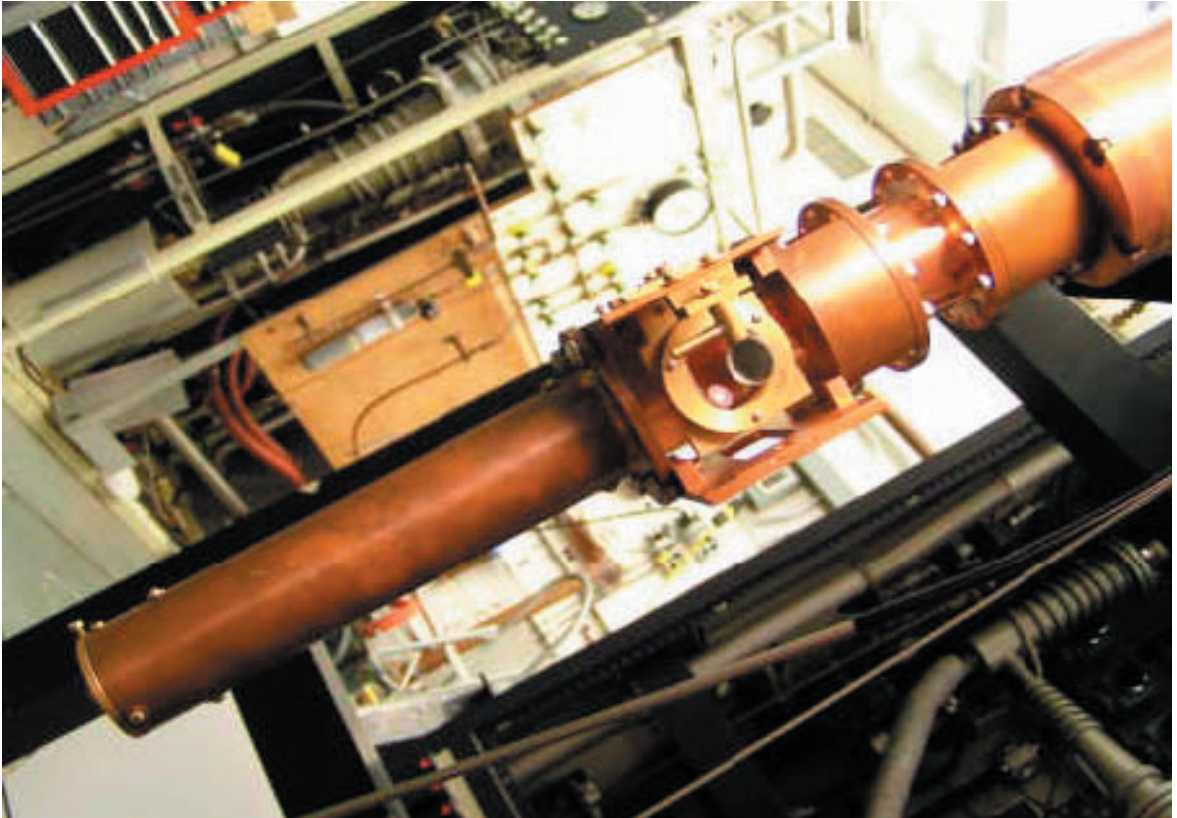


# Chapter 5

## *Low Temperature Condensed Matter Physics*



# Numerical studies of properties of confined Helium

Efstratios Manousakis  
Department of Physics and  
Center for Materials Research and Technology,  
Florida State University, Tallahassee, FL 32306-4350

July 1, 2003

## Abstract

We carry out state of the art simulations of properties of confined liquid helium near the superfluid transition to a degree of accuracy which allows to make predictions for the outcome of fundamental physics experiments in microgravity. First we report our results for the finite-size scaling behavior of heat capacity of superfluids for cubic and parallel-plate geometry. This allows us to study the crossover from zero and two dimensions to three dimensions. Our calculated scaling functions are in good agreement with recently measured specific heat scaling functions for the above mentioned geometries. We also present our results of a quantum simulation of sub-monolayer of molecular hydrogen deposited on an ideal graphite substrate using path-integral quantum Monte Carlo simulation. We find that the monolayer phase diagram is rich and very similar to that of helium monolayer. We are able to uncover the main features of the complex monolayer phase diagram, such as the commensurate solid phases and the commensurate to incommensurate transition, in agreement with the experiments and to find some features which are missing from the experimental analysis.

## 1 Specific Heat Scaling Function

First, we present the results of our simulation of the specific heat scaling function for superfluids confined in cubic and film geometries.

Even though earlier experiments on superfluid helium films of finite thickness [2] seemed to confirm the validity of the finite-size-scaling(FSS), there were later experiments[3, 4] where it was shown that the superfluid density of thick helium films does not satisfy FSS when the expected values of critical exponents were used. Similarly, in measurements of the specific heat of helium in finite geometries, other than the expected values for the critical exponents were found [5].

More recent experiments in microgravity environment[6] as well as earth bound experiments[7, 8] are consistent with scaling and they have determined the specific heat scaling function for the parallel plate (film) geometry (case (a)) and they are in reasonable agreement with the scaling function as was predicted by Monte Carlo simulations[9, 10] and renormalization group techniques[11]. While the specific heat scaling function for case (b) confinement has been theoretically determined[12] and it was found to be significantly suppressed relative to the case (a) there are so-far no experimental data to compare. More recently, the specific heat scaling function for the case (c) has been experimentally determined[13, 14].

The main goal of this part of this report is to present the results of our Monte Carlo simulations to determine the specific heat scaling function for cubes with open boundary conditions (BC) in all three directions (confining case (c)). In this case the scaling function characterizes the zero-dimensional to three-dimensional transition. Our results for the scaling function are compared to

the very recently obtained experimental results for specific heat scaling function in the case of cubic confinement[13, 14]. We find satisfactory agreement with no free parameters. In addition, we present results for the specific heat scaling function for the parallel plate geometry on lattices of size  $L_1 \times L_2 \times L$  with  $L_1 = L_2 \gg L$  where we have applied periodic BC along the  $L_{1,2}$ -directions and open BC along the film-thickness direction of size  $L$ . The latter case was carried out in order to compare the results for *Dirichlet BC* (on the top and bottom of the film) obtained earlier[9, 10]. In Refs [9, 10] it was found that while the results with periodic BC along the film-thickness direction were very different from those obtained with Dirichlet BC, the results obtained with Dirichlet BC fit the experimental results with no free parameter. In this paper we find that the scaling function obtained with open BC along the finite dimension is close to that obtained with Dirichlet and also fits reasonably well the experimental results obtained by the Confined Helium Experiment[6] (CHEX).

We have performed a numerical study of the scaling behavior of the specific heat of  $^4\text{He}$  in a cubic and in a film geometry at temperatures close to the critical temperature  $T_\lambda$ . The superfluid transition of liquid  $^4\text{He}$  belongs to the universality class of the three-dimensional  $x-y$  model, thus, we are going to use this model to compute the specific heat at temperatures near  $T_\lambda$  using the cluster Monte-Carlo method [15]. Using Wolff's cluster Monte Carlo updating algorithm[15], we computed

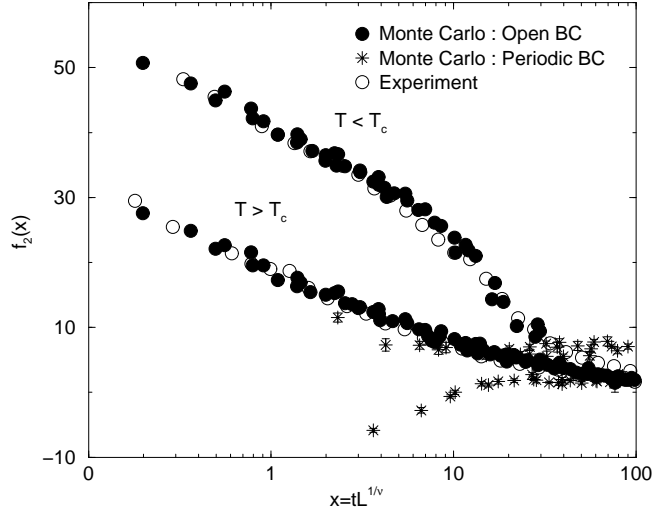


Figure 1: The computed universal function  $f_2(x)$  for open and periodic BC and for cubes is compared to the experimental results[13, 14]. We have used the experimental values for the critical exponents[17] to avoid the use of fitting parameters.

the specific heat  $c(T, L)$  of the  $x-y$  model as a function of temperature on several cubic lattices  $L^3$  (with  $L = 20, 30, 40, 50$ ). Open (free) boundary conditions were applied in all directions, namely the spins on the surface of the cube are free to take any value. These surface spins interact only with the 5 nearest neighbors, one in the interior and 4 on the surface of the cube and there is one missing neighbor. The results for the specific heat scaling function  $f_2$  for this geometry[19] and boundary conditions are compared with the experimental results in Fig. 1. Taking into consideration the fact that we have used no fitting parameter the agreement is excellent. To further investigate the role of open BC, we have also calculated the specific heat scaling function  $f_1(x)$  for the case of the parallel plate geometry  $L_1 \times L_2 \times L$  ( $L_{1,2} \gg L$ ) using periodic boundary conditions along the long directions of the film and *open* BC along the thickness direction  $L$ . For this case we need to take

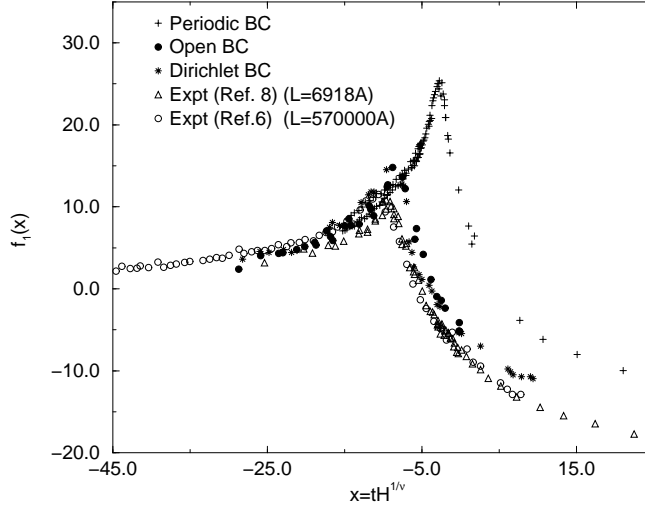


Figure 2: Film geometry: The computed universal function  $f_1(x)$  with open BC (solid circles) is compared to the previously calculated scaling function using Dirichlet BC[9](data shown as stars) and periodic BC (shown as plus signs) and the experimental results of Lipa *et al.*[6] (open circles) and those of Mehta *et al.*[8] (open triangles).

the limit  $L_{1,2} \rightarrow \infty$  first; in Ref. [10] it was found that using  $L_1 = L_2 = 5L$  was large enough, in the sense that systematic errors due to the finite-size effects from the fact that  $L_{1,2}$  are not infinite are smaller than the statistical errors for realistic computational time scales. The present simulations for films were done on lattices  $60 \times 60 \times 12$ ,  $70 \times 70 \times 14$ , and  $80 \times 80 \times 16$ . In Fig. 2 our results for films with various boundary conditions are compared with the experimental results. Notice that while periodic boundary conditions disagree with the experimental scaling function when more realistic boundary conditions, such as open or Dirichlet, are used the agreement becomes satisfactory.

## 2 Sub-monolayer $H_2$ on graphite

In this part of our report we present our results of our quantum simulation studies[20] of sub-monolayer molecular hydrogen on graphite in our effort to understand quantum films (helium and hydrogen).

The commensurate-incommensurate transition has been extensively studied in classical monolayer films both theoretically and experimentally. Monolayers of hydrogen or helium are quantum mechanical systems and, in principle, one might suspect a different behavior due to the effect of strong quantum fluctuations.

The monolayer phase diagram of molecular para-hydrogen adsorbed on graphite as inferred from experimental studies[21] is shown in Fig. 3. This phase diagram was originally drawn based on the anomalies found in the specific heat[22, 23, 24]; for the characterization of the various phases, low energy electron diffraction (LEED)[26, 27] as well as neutron diffraction[28, 21, 29] studies have been carried out. At  $1/3$  coverage the molecules condense on the surface of graphite in a  $\sqrt{3} \times \sqrt{3}$  commensurate solid. In the low coverage region ( $\rho < 0.6$ ) (in units of the  $\sqrt{3} \times \sqrt{3}$  commensurate density), it forms a commensurate solid-gas coexistence phase at low temperature and a 2D gas phase at higher temperature ( $T > 10K$ ). For coverages  $0.6 \lesssim \rho \lesssim 0.9$ , as a function of temperature, there is a transition from a commensurate solid cluster phase to a commensurate solid phase with



vacancies at higher temperature and to a 2D gas at even higher temperature. At density somewhat higher than unity the so-called  $\alpha$ -phase is formed which is believed to be a striped domain-wall solid phase and at higher temperature it transforms to the so-called  $\beta$ -phase and to a fluid phase at even higher temperature. At high densities a transition take place to a triangular incommensurate solid phase. We have recently studied[32] the phase diagram of molecular hydrogen on graphite at

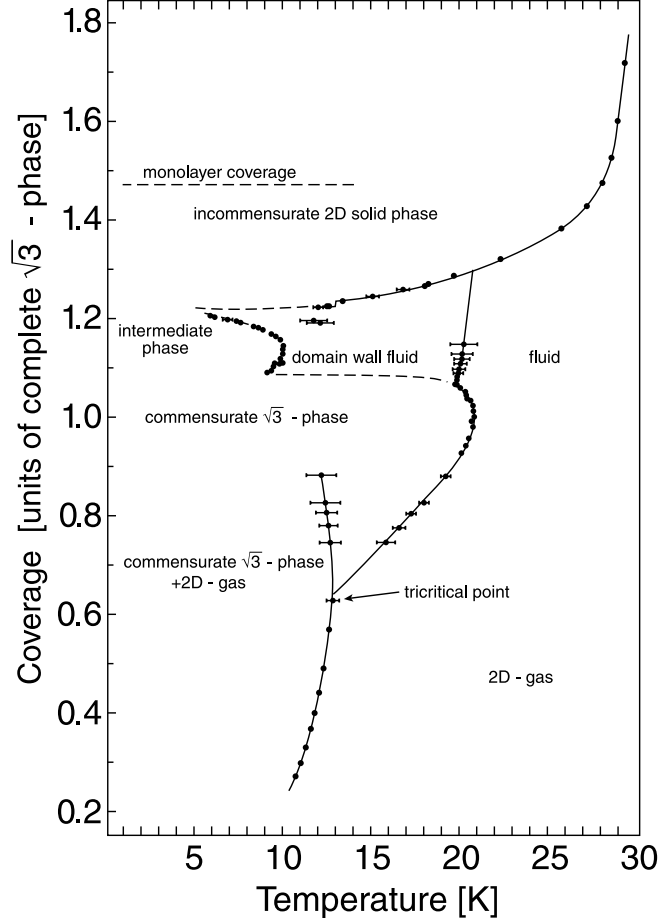


Figure 3: Phase diagram of molecular hydrogen adsorbed on graphite from Ref. [29] reproduced here for easy reference. Density 1.0 corresponds to the complete commensurate  $\sqrt{3} \times \sqrt{3}$  phase.

and below  $1/3$  coverage using Path Integral Monte Carlo (PIMC) simulation. Our computed phase diagram was in general agreement with that inferred from the experimental studies for this coverage range. Here we report our results obtained by PIMC calculation to study the phase diagram above the commensurate density which is less well understood both theoretically and experimentally. At coverages above  $\rho \simeq 1.05$  the monolayer undergoes a commensurate-incommensurate(C-IC) transition. While the existence of the so-called  $\alpha$  and  $\beta$  phases were known from the specific heat anomalies, their characterization came from LEED[26, 27] and neutron scattering[21] studies. Using LEED experiments Cui and Fain[26, 27] observed a uniaxial IC solid with *striped superheavy* domain walls and a rotated triangular IC solid at higher coverages  $\rho \geq 1.23$ . Freimuth, Wiechert, and Lauter[21] (FWL) presented a neutron diffraction study of the C-IC transition and their results are in agreement with the LEED results. They examined the commensurate-incommensurate solid transition, especially the striped domain-wall solid phase. In the  $\alpha$ -phase the diffraction intensity

has a main peak characteristic of a compressed lattice and a satellite peak on the lower side of the commensurate peak wave-vector position  $k_c = 1.703 \text{ \AA}^{-1}$  that arise from the spatial modulation due to ordered striped-domain walls. As coverage increases, the separation of the two peaks increases and the satellite intensity decreases. At higher temperatures the peak height drops and the satellite peak vanishes which implies that the commensurate domains vanish and the system becomes an isotropic fluid phase. As coverage increases, the first molecular hydrogen layer forms a rotated incommensurate solid (RIC) phase. Neutron diffraction studies show a sharp and intense peak at wave-vector  $k = 1.97 \text{ \AA}^{-1}$  at the density  $\rho = 1.34$  which reveals an IC equilateral triangular structure. This phase is continuously compressed as the coverage increases up to the highest density allowed before layer promotion.

In parallel to these experimental investigations several important theoretical studies were undertaken to understand the commensurate-incommensurate transition[33, 34, 35, 36, 37] in physisorbed systems. Molecular hydrogen and atomic helium physisorbed on graphite are quantum films characterized by strong zero point motion. Therefore, one could question the degree to which a classical picture might be valid and might expect new phenomena and phases to occur. Motivated by these thoughts we extended our earlier investigation[32] to study this system above  $1/3$  coverage up to layer completion starting from the known hydrogen molecule-molecule and hydrogen-graphite interactions[40, 41, 42, 43] and using the PIMC[39] which is a Quantum Monte Carlo technique adopted for the study of strongly interacting quantum films by Pierce and Manousakis[38].

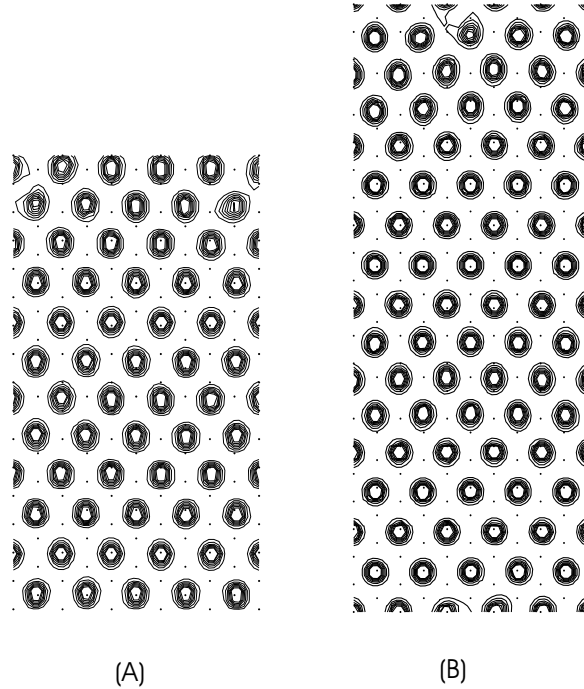


Figure 4: A(B) Contour plot of the probability distribution at the density  $0.0716 \text{ \AA}^{-2}$  ( $0.0694 \text{ \AA}^{-2}$ ) and  $T = 1.33 \text{ K}$ . The simulation cell contains 60 (80  $H_2$  molecules). The dots indicate graphite adsorption sites. The solid structure is uniaxially compressed along our y direction. In addition, in both case (A) and (B), two commensurate solid domains separated by the incommensurate solid domains can be seen which implies a mass density wave along the same direction.

We used simulation cells that can accommodate the structures that have been proposed by

FWL. a) First, we consider  $\rho = 0.0694 \text{ \AA}^{-2}$ . We have chosen a simulation cell with dimensions  $x = 5\sqrt{3} a_{gr}$  and  $y = 22 a_{gr}$ , where  $a_{gr} = 2.459 \text{ \AA}$  is the carbon-carbon distance on the graphite surface and 80 hydrogen molecules to produce the above density. In Fig. 4(B) we give the contour plot of the calculated probability distribution where we see that two commensurate-solid domains are separated by the incommensurate solid domains. The solid structure is uniaxially compressed along our  $y$  direction such that a new row of molecules is introduced for every 8 rows. Notice that the period in the  $x$ -direction is  $\sqrt{3}a_{gr}$  and there is modulation along the  $y$  direction with period  $11a_{gr}$ , so that the wavelength  $\lambda_s$  of this striped domain-wall modulation is  $\lambda_s = 27.049$ . b) Second, we have performed the simulation at the density  $\rho = 0.0716 \text{ \AA}^{-2}$ . We have chosen a simulation cell with dimensions  $x = 5\sqrt{3}a_{gr}$  and  $y = 16a_{gr}$  and 60 hydrogen molecules in order to achieve the above mentioned density. The calculated contour plot of the probability distribution is shown in Fig. 4(A). Notice that in this case also there is an ordered striped domain-wall solid phase along our  $y$  direction. Namely, the amplitude of the molecular density wave is modulated along the  $y$  axis with a period of about half our cell size along the  $y$  axis. Notice that there are two commensurate solid domains separated by denser regions.

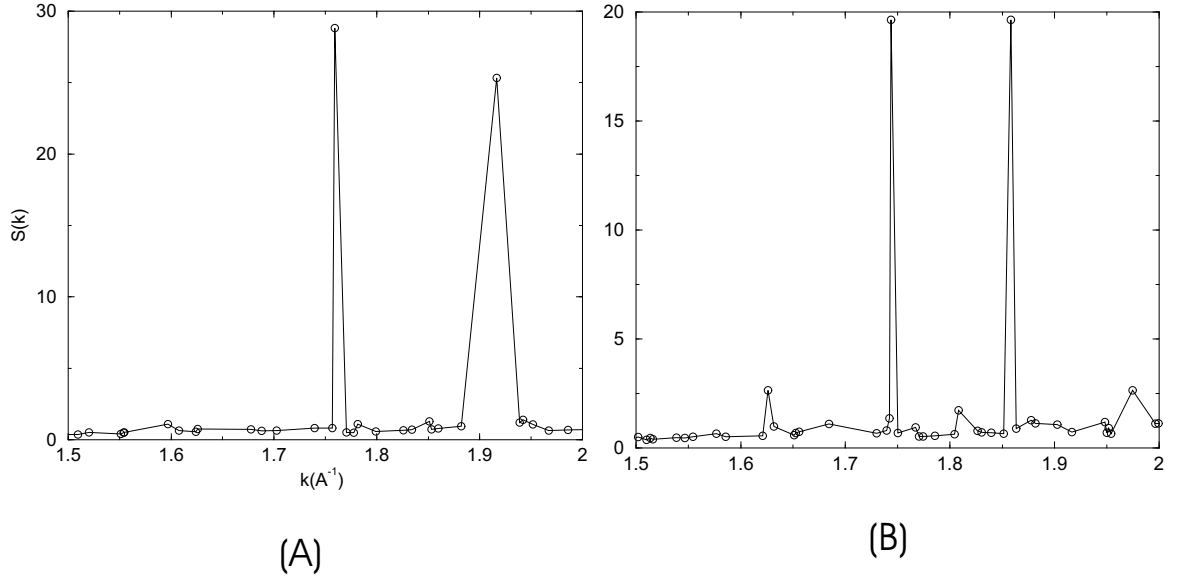


Figure 5: Static structure factor  $S(k)$  at the density  $0.0716 \text{ \AA}^{-2}$  ( $0.0694 \text{ \AA}^{-2}$ ) for  $T = 1.33 \text{ K}$  as a function of the magnitude of  $\vec{k}$ . The main Bragg peaks are at  $k_1 = 1.759 \text{ \AA}^{-1}$  and  $k_2 = 1.916 \text{ \AA}^{-1}$  ( $k_1 = 1.743 \text{ \AA}^{-1}$  and  $k_2 = 1.858 \text{ \AA}^{-1}$ ). There is a satellite peak located at  $k_{sat}^c = 1.597 \text{ \AA}^{-1}$  ( $k_{sat}^c = 1.626 \text{ \AA}^{-1}$ ). Notice that the satellite peak at in Fig. (A) is significantly weaker than the satellite peak at the lower density shown in Fig. (B)

Our computed static structure factor  $S(k)$  for  $\rho = 0.0694 \text{ \AA}^{-2}$  is shown in Fig. 4(A). The main Bragg peaks of this structure occur at  $\mathbf{k}_1 = (1.475 \text{ \AA}^{-1}, 0.929 \text{ \AA}^{-1})$  and  $\mathbf{k}_2 = (0, 1.858 \text{ \AA}^{-1})$ . The satellite peak occurs at  $\mathbf{k}_{sat}^c = (0, 1.626 \text{ \AA}^{-1})$ . The experimental values of the magnitude of the wave-vectors at the peaks are  $k_{main}^{exp} = 1.743 \text{ \AA}^{-1}$  and  $k_{sat}^{exp} = 1.632 \text{ \AA}^{-1}$ , which compare well with our computed values of  $k_1^c = 1.743 \text{ \AA}^{-1}$  and  $k_{sat}^c = 1.626 \text{ \AA}^{-1}$ . We believe that FWL could not observe the peak at  $\mathbf{k}_2$  because of the strong interference with the (002) graphite peak.

The interpretation of these results is as follows: Analyzing the contour plot of Fig. 4(B) we find that a) the solid appears uniaxially compressed along the  $y$  direction, by adding another row

for every 10 rows of molecules and spreading them evenly, while along the  $x$  direction the average spacing between the molecules remains that of the commensurate solid. b) superimposed there is a density modulation along the  $y$  direction which has wavelength several times greater than the average nearest neighbor distance but of small amplitude. The actual size of the wavelength  $\lambda_s$  of this striped domain-wall modulation is half of the length of our simulation cell in the  $y$ -direction, i.e.,  $\lambda_s = 27.05\text{\AA}$ , as discussed in the previous paragraph. The two main Bragg peaks correspond to the unit vectors which span the reciprocal space of this uniaxially compressed triangular solid structure. The satellite peaks are due to lateral modulation in our  $y$  direction and are located at  $\mathbf{k}_{sat} = \mathbf{k}_{1,2} - \mathbf{k}_s$ .  $\mathbf{k}_{1,2}$  correspond to the wave vector of each of the two main Bragg peaks and  $\mathbf{k}_s = (0, 2\pi/\lambda_s)$ , where  $\lambda_s$  is the wave length of a unit cell for the striped domain-wall solid structure in the modulated direction. Using this  $\lambda_s$  value,  $\mathbf{k}_2 = (0, 1.858\text{\AA}^{-1})$  and  $\mathbf{k}_s = (0, 0.232\text{\AA}^{-1})$  (obtained by using the values of  $\lambda_s = 27.049\text{\AA}$  found by inspection of Fig. 4(B)) we can find that the satellite peak position is at  $\mathbf{k}_{sat} = (0, 1.626\text{\AA}^{-1})$ , which agrees well with our peak value.

## 2.1 Domain Wall Melting

In Fig. 6 we present the contour plot of the the probability distribution where a striped domain-wall fluid phase (at  $T = 11.11K$ ) and a fluid phase (at  $T = 16.67$ ) are evident. Notice that the stripe domain-wall fluid phase (left part of Fig. 6) is characterized by mobile commensurate and incommensurate domains. To understand this contour plot we need to be reminded of the periodic boundary conditions used in our simulation and the fact that these domains cannot intersect each other. This implies that one domain will oscillate back and forth between the neighboring domains.

We would like to call the reader's attention on the presence of strong finite-size effects in this study of the domain wall melting. In addition, the domain boundary melting is analogous to the roughening of vicinal surfaces and meandering of steps, and our simulation cell is not wide enough to encompass formation of kink-pairs along the domain boundaries. We can very approximately determine the melting temperature of the domain-wall solid phase from the temperature dependence of the specific heat and from the temperature dependence of the peak height of the static structure factor  $S(k)$ .

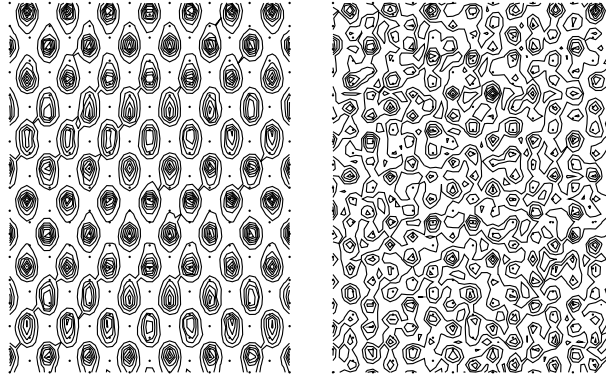


Figure 6: Contour plot of the probability distribution at the density  $0.0716\text{\AA}^{-2}$  at two temperatures  $11.11\text{ K}$  and  $16.67\text{ K}$ .

The calculated specific heat as a function of temperature is shown in Fig. 7 and is characterized by two peaks, the first corresponds to the melting of the domain-wall solid while the second peak

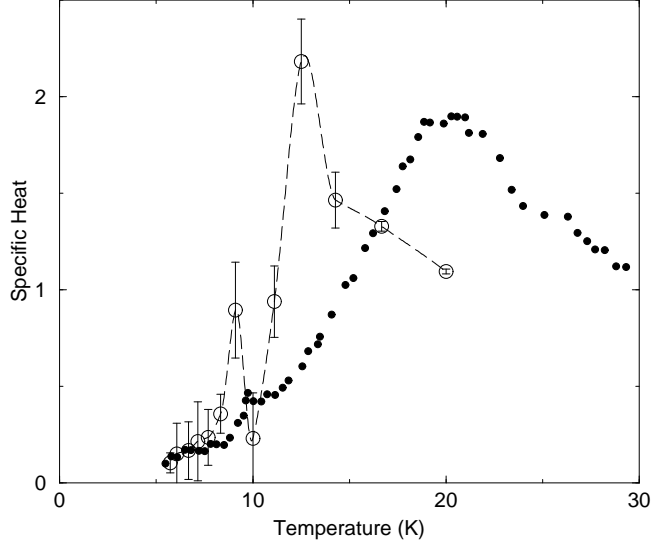


Figure 7: Specific heat versus temperature at the density  $0.0716 \text{ \AA}^{-2}$ . The long-dashed line is a spline fit to the specific heat values and is a guide to the eye. The filled circles are the experimental specific heat at the density  $0.0716 \text{ \AA}^{-2}$ . The simulation cell is  $29.813 \text{ \AA} \times 39.344 \text{ \AA}$  ( $84 H_2$  molecules). Our computed values for the melting and evaporation temperature are the peak positions,  $9.09 \text{ K}$  and  $12.5 \text{ K}$ , respectively.

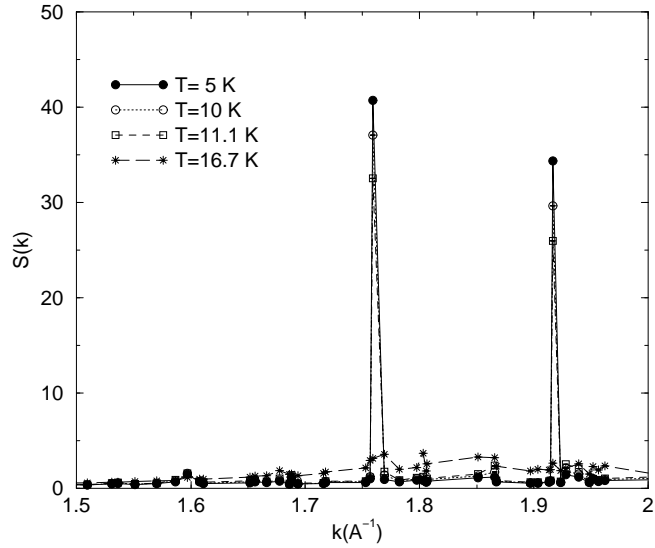


Figure 8: Static structure factor  $S(k)$  at the density  $0.0716 \text{ \AA}^{-2}$  for various temperatures.



indicates the melting of the stripes and the solid into a fluid. Our computed values for the melting temperature are generally lower than the experimental values. For example, for  $\rho = 0.0716 \text{\AA}^{-2}$  we find that at  $T = 9.09 \text{K}$  the striped domain-wall solid phase undergoes a transition to the domain-wall fluid phase and at  $T = 12.5 \text{K}$  the  $\beta$ -phase becomes an isotropic fluid phase. Factors for obtaining lower values for the critical temperature than the experimental values could be the finite-size effects and the interaction strength used to describe the hydrogen-graphite interaction. We also computed the static structure factor shown in Fig. 8 and we studied the temperature dependence of the height of its first main peak. The peak height significantly decreases near the melting temperature of the domain-wall solid and near the domain-wall evaporation temperature.

Clearly much larger size lattices are needed to study the nature of this phase transition. Such a study is beyond our current computational resources and we restrict ourselves to our qualitative results obtained here with full quantum mechanical treatment of the problem. In a different line of work one can use classical simulations of models of such stripe melting to carefully examine finite-size effects.

## 2.2 Rotated Incommensurate Solid

The first layer of molecular hydrogen adsorbed on graphite forms an incommensurate solid phase before the first layer is complete. We have carried out a simulation at the density  $\rho = 0.0849 \text{\AA}^{-2}$  using a simulation cell with dimensions  $x = 9 \sqrt{3} a_{gr}$  and  $y = 9 a_{gr}$ . The calculated probability distribution (Fig. 9) also clearly shows the presence of an equilateral triangular solid structure which is not registered with the underlying graphite lattice and it is rotated relative to the graphite lattice. This rotation was first predicted and discussed by Novaco and McTague[33]. The angle of the incommensurate lattice relative to the graphite lattice is approximately  $5^\circ$  in good agreement with the experimental value[27] for the above density. The calculated static structure factor has a single sharp peak at  $k = 1.99 \text{\AA}^{-1}$  corresponding to an unregistered equilateral triangular lattice in agreement with the value of  $k = 1.97 \text{\AA}^{-1}$  reported from the neutron diffraction experimental study[21].

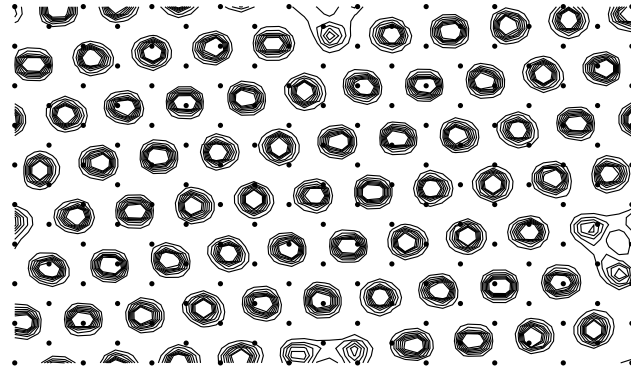


Figure 9: Contour plot of the probability distribution at the density  $0.0849 \text{\AA}^{-2}$ . The simulation cell is  $38.331 \text{\AA} \times 22.131 \text{\AA}$  ( $72 H_2$  molecules).

### 3 Acknowledgments

This work was supported by the National Aeronautics and Space Administration under grant No. NAG8-1773 and NAG8-2867.

### References

- [1] M. E. Fisher and M. N. Barber, Phys. Rev. Lett. **28** 1516 (1972); M. E. Fisher, Rev. Mod. Phys. **46** 597 (1974); V. Privman, Finite Size Scaling and Numerical Simulation of Statistical systems, Singapore: World Scientific 1990; E. Brezin, J. Physique **43** 15 (1982); V. Privman, J. Phys. **A23** L711 (1990).
- [2] J. Maps and R. B. Hallock, Phys. Rev. Lett **47** 1533 (1981); D. J. Bishop and J. D. Reppy, Phys. Rev. Lett. **40**, 1727 (1978).
- [3] I. Rhee, F. M. Gasparini, and D. J. Bishop, Phys. Rev. Lett. **63** 410 (1989).
- [4] I. Rhee, D. J. Bishop, and F. M. Gasparini, Physica **B165&166** 535 (1990).
- [5] T. Chen and F. M. Gasparini, Phys. Rev. Lett. **40** 331 (1978); F. M. Gasparini, T. Chen, and B. Bhattacharyya, Phys. Rev. **23** 5797 (1981).
- [6] J.A. Lipa, D.R. Swanson, J.A. Nissen, Z.K. Geng, P.R. Williamson, D.A. Stricker, T.C.P. Chui, U.E. Israelsson and M. Larsen, Phys. Rev. Lett. **84**, 4894 (2000); and J. Low Temp. Phys. **113**, 849 (1998).
- [7] S. Mehta and F.M. Gasparini, Phys. Rev. Lett. **78**, 2596 (1997).
- [8] S. Mehta, M.O. Kimball and F.M. Gasparini, J. Low Temp. Phys. **114**, 467 (1999).
- [9] N. Schultka and E. Manousakis, Phys. Rev. Lett. **75**, 2710 (1995).
- [10] N. Schultka and E. Manousakis, J. Low Temp. Phys. **109**, 733 (1997).
- [11] R. Schmolke, A. Wacker, V. Dohm, and D. Frank, Physica **B165 & 166** 575 (1990); V. Dohm, Physica Scripta **T49** 46 (1993); P. Sutter and V. Dohm, Physica **B194-196** 613 (1994); W. Huhn and V. Dohm, Phys. Rev. Lett. **61** 1368 (1988); M. Krech and S. Dietrich, Phys. Rev. **A46** 1886 (1992).
- [12] N. Schultka and E. Manousakis, J. Low Temp. Phys. **111**, 783 (1998).
- [13] M. O. Kimball, M. Diaz-Avila and F. M. Gasparini, Submitted to the editors of the LT23 conference in Hiroshima, Japan.
- [14] M. O. Kimball and F. M. Gasparini, Private Communication.
- [15] U. Wolff, Phys. Rev. Lett. **62**, 361 (1989).
- [16] N. Schultka and E. Manousakis, Phys. Rev. **B52**, 7528 (1995).
- [17] J. A. Lipa, J. A. Nissen, D. A. Stricker, D. R. Swanson, T. C. P. Chui, submitted for publication in Phys. Rev. **B**; J. A. Lipa, D. R. Swanson, J. A. Nissen, T. C. P. Chui, U. E. Israelsson, Phys. Rev. Lett, **76**, 944 (1996).

- [18] J. A. Lipa and T. C. P. Chui, Phys. Rev. Lett. **51**, 2291 (1983).
- [19] k. Nho and E. Manousakis, Submitted for publication. Archive cond-mat/0305500.
- [20] K. Nho and E. Manousakis, Phys. Rev. **B 67**, 195411 (2003).
- [21] H. Freimuth, H. Wiechert, and H. J. Lauter, Surf. Sci. **189& 190**, 548 (1987).
- [22] F. C. Motteler and J. G. Dash, Phys. Rev. B **31**, 346 (1985).
- [23] F. A. B. Chaves, M. E. B. P. Cortez, R. E. Rapp and E. Lerner, Surf. Sci. **150**, 80 (1985).
- [24] H. Freimuth and H. Wiechert, Surf. Sci. **162**, 432 (1985).
- [25] J. L. Seguin and J. Suzanne, Surf. Sci. **118**, L241 (1982).
- [26] J. Cui and S. C. Fain, Jr., Bull. Am. Phys. Soc. **31**, 376 (1986).
- [27] J. Cui and S. C. Fain, Jr., Phys. Rev. B **39**, 8628 (1989).
- [28] M. Nielsen, J. P. McTague, and W. Ellenson, J. Phys. (Paris) Colloq. **38**, C4-10 (1977).  
M. Nielsen, J. P. McTague, and L. Passell, in *Phase Transitions in Surface Films*, edited by J. G. Dash and J. Ruvalds (Plenum, New York, 1980).
- [29] H. Wiechert, Physica **B169**, 144 (1991).
- [30] H. Freimuth, H. Wiechert, H. P. Schildberg, and H. J. Lauter, Phys. Rev. B **42**, 587 (1990).
- [31] H. J. Lauter, H. Godfrin, V. L. P. Frank, and P. Leiderer, in *Phase Transitions in Surface Films 2*, edited by H. Taub, G. Torzo, H. J. Lauter, and S. C. Fain, Jr., (Plenum, New York, 1990).
- [32] K. Nho and E. Manousakis, Phys. Rev. **B 65**, 115409 (2002).
- [33] A. D. Novaco and J. P. McTague, Phys. Rev. Lett. **38**, 1286 (1977). J. P. McTague and A. D. Novaco, Phys. Rev. **B 19**, 5299 (1979).
- [34] J. Villain, Phys. Rev. Lett. **41**, 36 (1978).
- [35] P. Bak, D. Mukamel, J. Villain and K. Wentowska, Phys. Rev. **B 19**, 1610 (1979).
- [36] S. N. Coppersmith, D. S. Fisher, B. I. Halperin, P. A. Lee and W. F. Brinkman, Phys. Rev. Lett. **46**, 549 (1981); Phys. Rev. **B 25**, 349 (1982).
- [37] T. Halpin-Healy and M. Kardar, Phys. Rev. B **34**, 318 (1986).
- [38] M. Pierce and E. Manousakis, Phys. Rev. B **59**, 3802 (1999).
- [39] D. M. Ceperley, Rev. Mod. Phys. **67**, 279 (1995).
- [40] I. F. Silvera and V. V. Goldman, J. Chem. Phys. **69**, 4209 (1978).
- [41] A. D. Crowell and J. S. Brown, Surf. Sci. **123**, 296 (1982).
- [42] W. A. Steele, Surf. Sci. **36**, 317 (1973).
- [43] W. E. Carlos and M. W. Cole, Surf. Sci. **91**, 339 (1980).

## **Theoretical Analysis of Thermodynamic Measurements near a Liquid-Gas Critical Point**

M. Barmatz, Fang Zhong and Inseob Hahn  
Jet Propulsion Laboratory, California Institute of Technology

Over the years, many ground-based studies have been performed near liquid-gas critical points to elucidate the expected divergences in thermodynamic quantities. The unambiguous interpretation of these studies very near the critical point is hindered by a gravity-induced density stratification. However, these ground-based measurements can give insight into the crossover behavior between the asymptotic critical region near the transition and the mean field region farther away. We have completed a detailed analysis of heat capacity, susceptibility and coexistence curve measurements near the  $^3\text{He}$  liquid-gas critical point using the minimal-subtraction renormalization (MSR) scheme within the  $\phi^4$  model. This MSR scheme, using only two adjustable parameters, provides a reasonable global fit to all of these experimental measurements in the gravity-free region out to a reduced temperature of  $|t| \sim 2 \times 10^{-2}$ . Recently this approach has also been applied to the earlier microgravity measurements of Haupt and Straub in  $\text{SF}_6$  with surprising results. The conclusions drawn from the MSR analyses will be presented. Measurements in the gravity-affected region closer to the  $^3\text{He}$  critical point have also been analyzed using the recent crossover parametric model (CPM) of the equation-of-state. The results of fitting heat capacity measurements to the CPM model along the  $^3\text{He}$  critical isochore in the gravity-affected region will also be presented.

## **Measurement of critical adsorption of nitrogen near its liquid-vapor critical point**

Moses Chan  
Penn State University

The density profile of a critical fluid near a solid surface is expected to show an universal shape. This is known as critical adsorption (1). The measurement of this effect, especially close to the critical point, is often obscured by gravity. We were able to separate the gravitational effect from critical adsorption by using two capacitors, one with a large gap and one with a small gap of approximately 2  $\mu\text{m}$ . Within the uncertainty in the measurement, our data, which ranges between  $10^{-3}$  to  $2 \times 10^{-6}$  in reduced temperatures, is consistent with the predicted power law dependence. This work is carried out in collaboration with Rafael Garcia, Sarah Scheidemantel and Klaus Knorr. It is funded by NASA's office of Biological and Physical Research under grant NAG8-1761.

(1) M.E. Fisher and P.-G. deGennes, C.R. Acad.Sci.Paris, Ser.B 287, 209(1978).



## **Quartz microbalance study of 400-angstrom thick helium films near the lambda point**

Moses H.W. Chan  
Penn State University

In a recent measurement we observed the thinning of an adsorbed helium film induced by the confinement of critical fluctuations a few millikelvin below the lambda point. A capacitor set-up was used to measure this Casimir effect (1). In this poster we will present our measurement of an adsorbed helium film of 400 angstroms near the lambda point with a quartz microbalance. For films this thick, we must take into account the non-linear dynamics of the shear waves in the fluid. In spite of the added complications, we were able to confirm the thinning of the film due to the Casimir effect and the onset of the superfluid transition. In addition, we observe a sharp anomaly at the bulk lambda point, most likely related to critical dissipation of the first sound. This work is carried out in collaboration with Rafael Garcia, Stephen Jordon and John Lazzaretti. This work is funded by NASA's Office of Biological and Physical Research under grant NAG8-1761.

(1) R.Garcia and M.H.W.Chan, Phys.Rev. Lett. 83,1187(1999).

# Convection in a Very Compressible Fluid: Comparison of Simulations With Experiments

H. Meyer<sup>1</sup>, A. Furukawa<sup>2</sup>, A. Onuki<sup>2</sup> and A.B. Kogan<sup>1,\*</sup>

1. *Department of Physics, Duke University, Durham, NC 27708-0305, USA*

2. *Department of Physics, Kyoto University, Kyoto 606-8502, Japan .*

*\*Present address: Department of Physics, MIT, Cambridge, MA 02139-4307, USA.*

The time profile  $\Delta T(t)$  of the temperature difference, measured across a very compressible fluid layer of supercritical  $^3\text{He}$  after the start of a heat flow, shows a damped oscillatory behavior before steady state convection is reached. The results for  $\Delta T(t)$  obtained from numerical simulations and from laboratory experiments are compared over a temperature range where the compressibility varies by a factor of  $\approx 40$ . First the steady-state convective heat current  $j^{\text{conv}}$  as a function of the Rayleigh number  $Ra$  is presented, and the agreement is found to be good. Second, the shape of the time profile and two characteristic times in the transient part of  $\Delta T(t)$  from simulations and experiments are compared, namely 1)  $t_{\text{osc}}$ , the oscillatory period and 2)  $t_p$ , the time of the first peak after starting the heat flow. These times, scaled by the diffusive time  $\tau_D$  versus  $Ra$ , are presented. The agreement is good for  $t_{\text{osc}}/\tau_D$ , where the results collapse on a single curve showing a power-law behavior. The simulation hence confirms the universal scaling behavior found experimentally. However for  $t_p/\tau_D$ , where the experimental data also collapse on a single curve, the simulation results show systematic departures from such a behavior. A possible reason for some of the disagreements, both in the time profile and in  $t_p$  is discussed. In the Appendix a third characteristic time,  $t_m$ , between the first peak and the first oscillation minimum is plotted and a comparison between the results of experiments and simulations is made.

## I. INTRODUCTION

In a Raleigh-Bénard (RB) cell, the start of a constant heat flow across the fluid layer produces an initial rise in the temperature difference across this layer,  $\Delta T(t)$ , with a transient profile determined by the fluid convection dynamics, and which then tends to a steady state value, labeled  $\Delta T$ . Recently such heat flow experiments were carried out [1,2] on a very compressible fluid in its convective state, supercritical  $^3\text{He}$ , along the critical isochore  $\langle \rho \rangle = \rho_c$ , where the critical temperature is  $T_c = 3.318$  K. The fluid layer height in the experiments was  $L=0.106$  cm and the diameter of the cylindrical cell was 5.7cm. For this large aspect ratio, the predicted critical Rayleigh number is  $Ra_c=1708$ , as was confirmed by the experiments [1]. Over the reduced temperature range  $0.009 \leq \epsilon \equiv (T - T_c)/T_c \leq 0.2$  where the experiments were analyzed, the isothermal compressibility increases by a factor of  $\approx 40$  as  $T_c$  is approached. The substantial change in the fluid properties along  $\rho_c$  is reflected in large changes of the transient profile, where damped oscillations were observed after the first peak of  $\Delta T(t)$  for  $\epsilon \geq 0.009$ .

This paper compares the results of experimental data, and of simulations extending those of refs. [3,4], for the time profile  $\Delta T(t)$  in the regime where the fluid approaches steady-state convection. Reference is also made of recently published simulation results by Amiroudine and Zappoli [5]. In the simulations done in refs. [3,4], two new terms are added in the heat conduction equation; the first takes into account the adiabatic heating taking place throughout the cell (the “piston effect”), and the second accounts for the adiabatic temperature gradient effect within plumes leading to the Schwarzschild criterion of the convection onset in compressible fluids [6]. In the work of ref. [5] the Navier-Stokes (NS) equation, together with an enthalpy equation were used, without a specific term to simulate the piston effect, since the latter is implicitly taken into account in the work of the pressure forces term in the enthalpy equation. The simulations were made in two dimensions, where the fluid was contained in a cell with the same height  $L$  as in the experiment. The aspect ratio was 4 in refs. [3,4] and 2 in ref. [5] with the periodic boundary condition in the horizontal direction in order to reproduce the conditions of the experimental cell with a large aspect ratio. The simulations for  $\epsilon = 0.05$  in ref [4] extended until  $[Ra - Ra_c] \approx 4 \times 10^6$  and until  $\approx 1.7 \times 10^5$  for other values of  $\epsilon$ . Simulation results in this paper, except those of  $\epsilon = 0.05$  in refs. [3,4], are newly obtained using the scheme in ref. [4].

The outline for the remainder of this paper is as follows: First, a general discussion of the profiles  $\Delta T(t)$  will be made, with presentation of some examples and an appraisal of the degree of agreement between experiments and simulations. Second, a comparison of the steady state results from experiments and simulations will be presented, expressed in terms of the convection heat current  $j^{\text{conv}}$  versus the reduced Rayleigh number  $ra^* \equiv [Ra - Ra_c]/Ra_c$ . Third, a comparison of the transients from experiments and simulations will be made by the examination of two “characteristic times”, the time  $t_p$  of the first peak after the start of the heat current, and  $t_{\text{osc}}$ , the oscillation

period in the damped oscillatory decay. Both will be presented in a scaled form, again versus  $[Ra - Ra_c]$ . This quantitative comparison illustrates well the agreements and deviations between simulations and experiments, which will be discussed in the Conclusions. In the Appendix, a third characteristic time,  $t_m$ , between the first peak and the first minimum in the  $\Delta T(t)$  profile is shown for both the experiments and the simulations.

## II. GENERAL OBSERVATIONS ON THE PROFILES $\Delta T$ VERSUS TIME.

We briefly emphasize, as was done in refs [1,2], that the experiments were done under conditions where the stratification from gravity was small and where the temperature changes across the fluid were kept small enough that the changes in the fluid properties across the fluid layer were smaller than a few percent. Thus the conditions for the approximations in a Boussinesq-like fluid in the momentum equation were maintained. In Fig. 9 in ref. [1] a representative evolution is shown of the observed profile  $\Delta T(t)$  at  $\epsilon = 0.05$  as a function of the heat current  $q$ . Both experiments and simulations show over a certain range of heat flow  $Q$  and of temperature a damped oscillatory profile  $\Delta T(t)$  as shown in Figs. 1 and 2 of ref. [3], Figs. 1 of ref. [4], both at  $\epsilon = 0.05$  and Fig.2 of ref. [5] at  $\epsilon = 0.01$ , which are not reproduced here. Considering that the experimental data have not been corrected for the time lag introduced by the temperature recording instrumentation with a time constant of  $\tau = 1.3$  s., the qualitative agreement is quite satisfactory. However as  $\epsilon$  increases and the compressibility decreases, the disagreement between the transient regime of experiments and simulations becomes sizeable. This can be seen in Fig.1 at  $\epsilon = 0.2$  for two values of the heat flow  $q \approx 3.7 \times 10^{-7}$  and  $2.1 \times 10^{-7}$  W/cm<sup>2</sup>. By contrast the steady-state value for

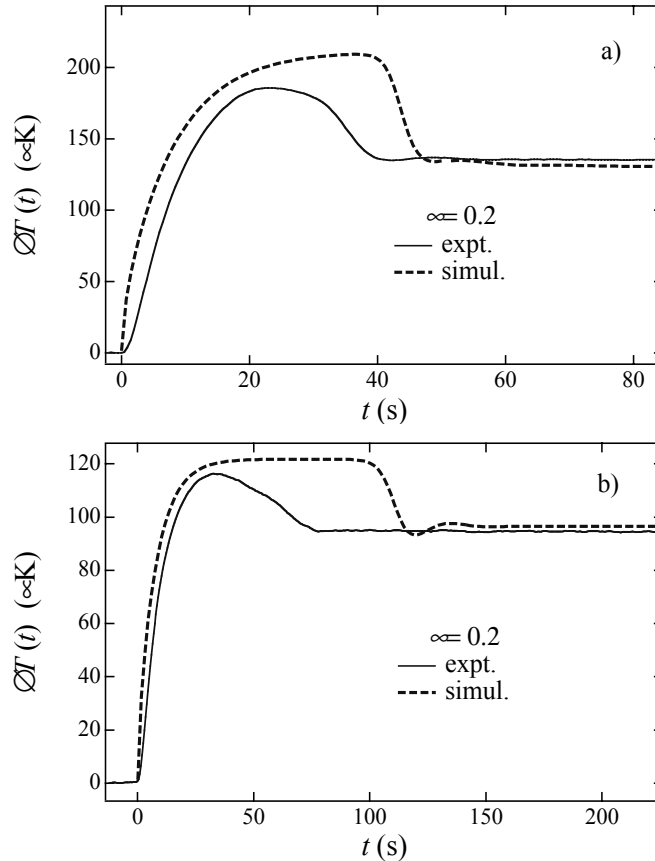


FIG. 1. Plots of the profile  $\Delta T(t)$  versus time for two values of the heat flow  $q$  (in  $10^{-7}$  W/cm<sup>2</sup>) at  $\epsilon = 0.2$  and comparison between experiments and simulations a)  $q = 3.89$  (expt),  $3.67$  (simul.) and b)  $q = 2.16$  (expt),  $2.10$  (simul.).

$\Delta T$  reached in both the experiments and in simulations for the same value of  $q$  remains closely the same. In the experimental trace for the lower value of  $q$ , no damped oscillations are seen, but rather a non-exponential decay of the overshoot. This is the regime labeled “truncated oscillations”, described in Fig.2 of ref. [2]. (See also Appendix A). Simulations, however, always show damped oscillations in the convective state.

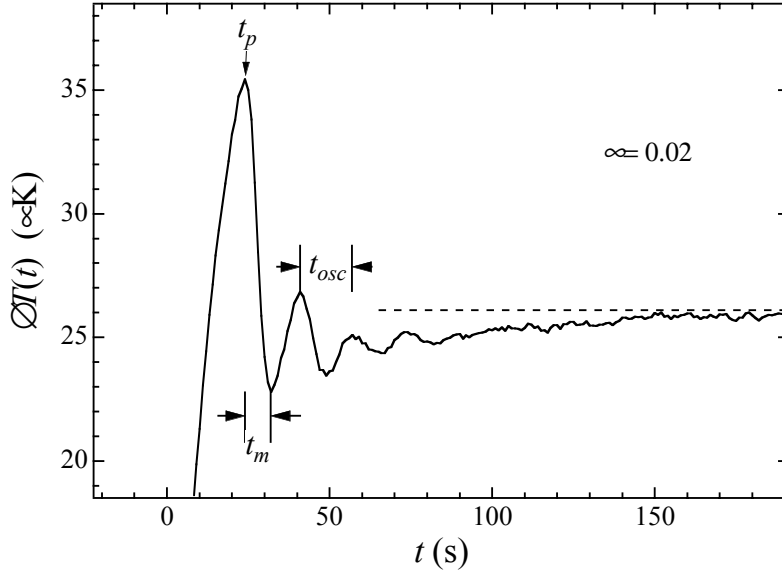


FIG. 2. A representative profile  $\Delta T(t)$  after starting the heat current, with the definition of the times  $t_p$ ,  $t_m$  and  $t_{osc}$  and the slow exponential relaxation to the steady-state value of  $\Delta T$  (dashed line) with a time constant  $\tau_{tail}$ . The recording is for  $\epsilon = 0.02$  with the heat flow  $q = 1.69 \cdot 10^{-7} \text{ W/cm}^2$ .

In Fig.2, we present an enlarged segment near the peak of  $\Delta T(t)$  for a representative trace at  $\epsilon = 0.02$ , which exhibits and defines various characteristic times in the transient. We will consider two of these times in the main part of this paper, namely 1) the peak  $t_p$  of the first peak after the start of the heat current and 2) the period  $t_{osc}$  of the damped oscillations.

Furthermore there is  $t_m$ , the interval between the first peak and the first minimum in the regime of damped oscillations or between the peak and the “kink” to the flat portion in the regime of “truncated oscillations”. The discussion of  $t_m$  is deferred to Appendix B, because it is more complex than for  $t_{osc}$  and  $t_p$ . Finally, the profile tends asymptotically from below to the steady state value  $\Delta T$  with a relaxation time  $\tau_{tail}$ , obtained by fitting this transient tail with a simple exponential, and we note that this feature has not been detected in the simulations either in ref. [4] or in ref. [5].

The transient shape, principally at short times where the changes in  $\Delta T(t)$  are rapid, is affected by the instrumentation time constant, and also the modulated minimum shown in Fig.2 makes an analysis of the oscillation amplitude decay rate uncertain. However inspection of the many recorded experimental traces shows that for a given  $\epsilon$  (or compressibility), the rates for both the oscillations and their amplitude decay increase with the heat current. For values large enough of  $q$  at a given  $\epsilon$ , the first peak and the oscillations become attenuated and averaged out. (See Fig. 4 of ref [2]). The likely cause for this observation is that  $t_{osc}$  becomes comparable or smaller than the instrumentation time constant. An averaging effect of the oscillations due to a negative interference between non-synchronous plumes that results from the large lateral dimension of the experimental cell was suggested in ref. [4]. This suggestion might be very relevant in the regime  $\epsilon < 0.009$  where no oscillations could be observed, even when their expected period was well above that of the instrumental time constant (See ref. [2], Section III).

### III. COMPARISON OF STEADY-STATE RESULTS IN EXPERIMENTS AND SIMULATIONS

In ref. [1] the steady-state experimental results were presented in terms of the dimensionless convective heat current  $j^{conv}$  versus  $ra^*$ . Here  $j^{conv}$  is the ratio of the convective portion of the heat current to that conducted through the fluid at the transition to convection, which leads to the relation [7]

$$j^{conv} \equiv (Nu - 1)(ra^* + 1) \quad (1)$$

where  $Nu$  is the Nusselt number. Along the critical isochore of a fluid, where the compressibility diverges as  $T_c$  is approached, Gitterman and Steinberg [8] have shown that for the fluid onset of mechanical instability there is a crossover from the Rayleigh - to the Schwarzschild (or “adiabatic temperature gradient”) criterion as  $T_c$  is approached. Then it has been shown ([9] and references therein) that at the onset of convection, the temperature drop across the fluid layer is given by

$$\Delta T_{onset} = \Delta T_R + \Delta T_{ad} \quad (2)$$

where  $\Delta T_R = Ra_c \times \nu D_T / \alpha_P g L^3$ , the familiar Rayleigh term, and  $\Delta T_{ad} = L g T \alpha_P / C_P$ , the adiabatic temperature difference contribution (for  $\Delta T_R$  and  $\Delta T_{ad}$  see for instance Tritton's monograph [10]). Here  $\nu$  is the kinematic viscosity,  $D_T$  the thermal diffusivity,  $\alpha_P$  the isobaric thermal expansion coefficient,  $g$  the gravity acceleration,  $L$  the height of the fluid layer and  $C_P$  the specific heat at constant pressure.

As has been described in some detail in refs. [1,2],  $Nu$  and  $Ra$  have to be corrected for the contribution from the adiabatic temperature gradient. One then obtains

$$Ra_{corr} = \frac{Ra(\Delta T - \Delta T_{ad})}{\Delta T} \quad \text{and} \quad Nu_{corr} = \frac{(\Delta T_{diff} - \Delta T_{ad})}{(\Delta T - \Delta T_{ad})} \quad (3)$$

and hence

$$ra_{corr}^* \equiv (Ra_{corr}/Ra_c - 1) \quad \text{and} \quad j_{corr}^{conv} \equiv (Nu_{corr} - 1)(ra_{corr}^* + 1) \quad (4)$$

Here  $\Delta T_{diff}$  is the temperature drop across the fluid in the diffusive regime for the same heat current producing the observed  $\Delta T$ . Because both  $j_{corr}^{conv}$  and  $ra_{corr}^*$  vary over about five orders of magnitude for the range covered by the data, a more sensitive way is to present the ratio  $j_{corr}^{conv}/ra_{corr}^*$  versus  $ra_{corr}^*$ . Furukawa and Onuki [4] theoretically justified the validity of the scaling relations in terms of these corrected quantities. This is done in Fig.3a where the points recorded close to the transition to convection and showing rounding instead of a sharp convection onset, have been omitted. Furthermore the data for  $\epsilon < 0.009$ , where no damped oscillations were obtained in the transients, and for which no simulations were carried out, have not been used in this figure. As can be seen, within the scatter all the data points nearly collapse on a common curve. For  $ra_{corr}^* < 1$ , the data extrapolate to a horizontal line with an amplitude of  $1.3 \pm 0.1$ . This asymptotic result,  $j_{corr}^{conv} = 1.3ra_{corr}^*$ , which represents data slightly above the onset of convection, has been discussed in ref. [1] where it had been concluded that the amplitude is consistent with a straight roll convection prediction [11]. In Fig. 3b, the experimental data are replaced by a solid curve representing its average, and the results from simulations are shown by the symbols at various values of  $\epsilon$ . In the intermediate range of  $ra_{corr}^*$  these data points collapse on a curve slightly above the experimental average, and also within their scatter they tend to the same limiting amplitude of 1.3, as do the experiments. Therefore they also imply straight roll convection, a picture which is plausible in the 2D simulation which represents a cross-section of rolls in a geometry with parallel vertical periodic boundaries.

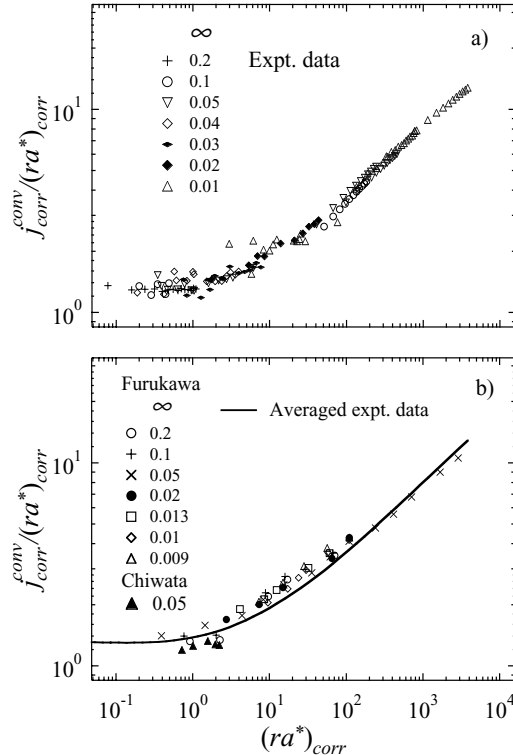




FIG. 3. The convective heat current  $j_{\text{corr}}^{\text{conv}}$  divided by  $ra_{\text{corr}}^* = [Ra_{\text{corr}} - Ra_c]/Ra_c$ , versus  $ra_{\text{corr}}^*$ , both corrected for the adiabatic temperature gradient contribution. a) Experimental data at various values of  $\epsilon$ . b) Data from simulations at different values of  $\epsilon$  shown by symbols. The solid line is the average of the experimental data in a).

#### IV. TRANSIENT CHARACTERISTIC TIMES IN EXPERIMENTS AND SIMULATIONS

##### A. Background information

The mechanism responsible for the damped oscillations for a highly compressible fluid at constant average density has been discussed most recently by Furukawa and Onuki [4] and by Amiroudine and Zappoli [5]. From their simulations, these authors presented a detailed analysis of the time evolution of the temperature in various locations in the fluid layer. We refer to their description on how maxima and minima of  $\Delta T(t)$  are produced by the “piston effect” that leads to the vertical flow of successive “warm” and “cold” fluid masses. The snapshots of the simulations by Chiwata and Onuki [3] had already pictured the formation of plumes during these processes, and the evidence of warm and cold vertical flows.

In the analysis of the experimental data [2], two characteristic times describing the remarkable oscillatory behavior,  $t_m$  and  $t_{\text{osc}}$ , were discussed, which are shown in Fig.2 for a representative  $\Delta T(t)$  profile. The experimental results for the time  $t_p$  have not been analyzed before and are presented here for the first time. In order to keep the analysis of the results tractable, their discussion will not include  $t_m$ , which will be dealt with in Appendix A. In the experimental data analysis, the relaxation time  $\tau_{\text{tail}}$  to the steady state convection was also presented in ref. [2]. All the data of  $t_{\text{osc}}$  and  $\tau_{\text{tail}}$  at the various reduced temperatures  $\epsilon$ , scaled by the diffusion time  $t_D \equiv L^2/4D_T$ , and plotted versus the Rayleigh number difference  $[Ra_{\text{corr}} - Ra_c]$  were found to collapse within a scatter of  $\pm 15\%$  on two respective curves, an unexpected result.

$\epsilon$	$C_p/C_v \equiv \gamma$	$B(\gamma) \equiv \tau_D/t_D$	$\tau_D$ (s.)
0.01	119	1.01	265
0.02	57.7	1.03	134
0.03	38.1	1.06	92.0
0.04	28.5	1.08	69.9
0.05	22.8	1.10	57.0
0.07	16.5	1.13	42.2
0.10	11.8	1.19	31.8
0.20	6.48	1.35	19.8

Table 1. The ratio  $C_p/C_v \equiv \gamma$  for  $^3\text{He}$  along its critical isochore for several values of the reduced temperature  $\epsilon$ , the ratio  $B(\gamma)$  of the diffusive times, calculated from Fig.2 ref.12 (Behringer et al.) and the diffusive time  $\tau_D$ .

We now discuss the choice of the scaling time in the data for  $t_{\text{osc}}$  and  $t_p$  versus the Rayleigh number. As mentioned above, the diffusion time  $t_D$  was used as the scale for  $t_{\text{osc}}$  in the plot versus  $[Ra_{\text{corr}} - Ra_c]$ . This time  $t_D$  was first used in the Navier Stokes equation leading to the simulations of ref. [3] under the conditions of constant average density and valid for  $C_p/C_v \equiv \gamma \gg 1$ . In the absence of convection,  $t_D$  can be related to the relaxation time  $\tau_0 = L^2/\pi^2 D_T$  of the lowest diffusion mode in a RB - or in a standard thermal conductivity cell [12]. However over the experimental and simulation range where  $0.2 \geq \epsilon \geq 0.009$ , the condition  $\gamma \gg 1$  is only progressively realised as  $\epsilon$  decreases to 0.01. In ref. [12] expressions for the solution of  $\tau_0$  as a function of  $\gamma$  were derived. As  $\gamma \rightarrow 1$ ,  $\tau_0 \rightarrow 4L^2/\pi^2 D_T$ , and this last value is the same as for a fluid relaxing at constant pressure. In general  $\tau_0(\gamma) = B(\gamma)L^2/\pi^2 D_T$ , where  $B(\gamma) = (\pi/q_0 L)^2$ , obtained from Fig.2 of ref [12] with  $q_0$  the wave number of the lowest mode.  $B(\gamma)$  is presented in Table 1 for several values of  $\epsilon$  relevant to the experiments and simulations in this paper. As can be seen in this Table, the ratio  $\tau_0(\gamma)/\tau_0(\gamma = \infty)$  decreases with  $\epsilon$  and tends to 1 for  $\epsilon < 0.01$ . The use of the time  $\tau_D \equiv \tau_0(\gamma)\pi^2/4$  as a scale for the convection transient characteristic times is therefore preferable to  $t_D$ . It turns out that the choice of  $\tau_D$  as the scaling time improves the collapsing of the experimental data points for both  $t_{\text{osc}}$  and  $t_p$ . In the following subsections we present and compare these times obtained experimentally and from simulations.

##### B. the oscillatory period $t_{\text{osc}}$

In ref. [2], Fig.4 presented  $t_{\text{osc}}$  scaled by  $t_D$  and plotted versus  $[Ra_{\text{corr}} - Ra_c]$ . The substitution of  $\tau_D$  as a scale gives a better collapsing of the data points than does  $t_D$ , particularly at the lower values of  $[Ra_{\text{corr}} - Ra_c]$  where most of the data points at the higher values of  $\epsilon$  lie. Within the scatter of  $\pm 15\%$  the data for  $10^3 < [Ra_{\text{corr}} - Ra_c] < 5 \times 10^5$

can be represented by a power law with an exponent of  $-0.52 \pm 0.02$ . In Fig. 4a we present these data and in Fig.4b its average, obtained by a fit to a power law with a corrective term for the larger  $Ra$  values. Also in Fig. 4b we show by symbols the results from the simulations by the Kyoto group (two of the present authors, A.F. and A.O. and Chiwata) and by Amiroudine and Zappoli [5] at various values of  $\epsilon$ . The agreement appears to be good, though the simulations indicate some small systematic deviations from collapse on a single “universal” line. The basic reason for the apparent power law with an exponent of  $-1/2$  remains to be understood.

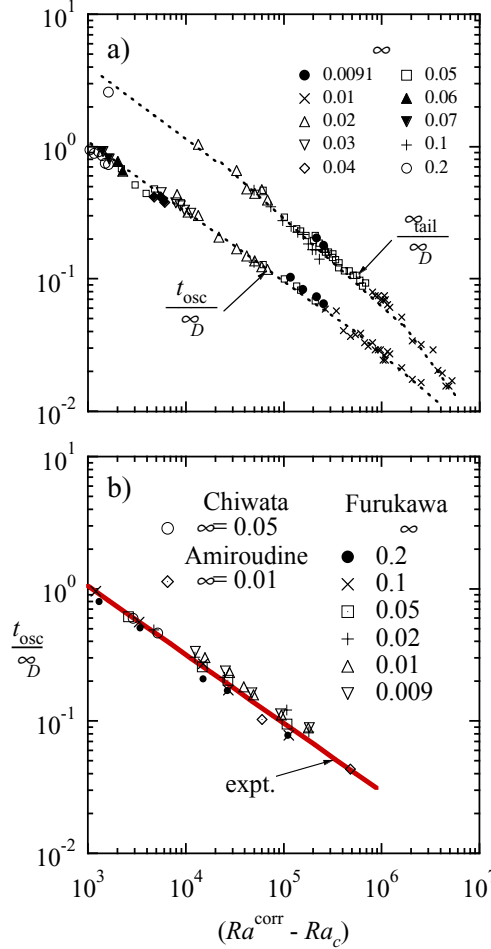


FIG. 4. The oscillation period  $t_{osc}$  and the time  $\tau_{tail}$  for the relaxation to the steady-state, both scaled by the diffusion time  $\tau_D$ , versus  $[Ra^{corr} - Ra_c]$ . a): Experimental data at various values of  $\epsilon$ . b): Symbols show the simulation data at different values of  $\epsilon$ , and the solid line is the average of the experimental data in a).

### C. The location of the first peak at $t_p$

In the experiments, the initial rise of the measured transient  $\Delta T(t)$  after the start of the heat flow across the fluid layer is affected by the time constant of the thermometer circuitry,  $\tau = 1.3$  s. as described in ref. [1]. This is especially so at short times, when the  $\Delta T(t)$  increases rapidly, and as a result the measured value of the time at the first peak has to be corrected. This was done by comparing the shift in time between the calculated rise of  $\Delta T(t)$  in the conducting regime (Eq.3.3 of ref. [4]) and the recorded curve for several values of  $\epsilon$  and  $q$ . This shift was between 2 and 3 s. and  $t_p$  was obtained after a crude correction was made by subtracting  $\delta t = 2$  s. from the measured time at the peak. The times  $t_p$  used in this analysis ranged from  $\approx 100$  to  $\approx 7$  s. Fig.5a shows the scaled representation  $t_p/\tau_D$  of the experimental times versus  $[Ra_{corr} - Ra_c]$ . There is excellent collapse of the data for all the values of  $\epsilon$ , even extending to the region of  $\epsilon < 0.009$  where no damped oscillations are observed [2]. In Fig.5b the solid curve represents the average of the experimental data, as obtained by a polynomial fit. Symbols show the results from simulations at various values of  $\epsilon$ . The data from ref. [3] at  $\epsilon = 0.05$

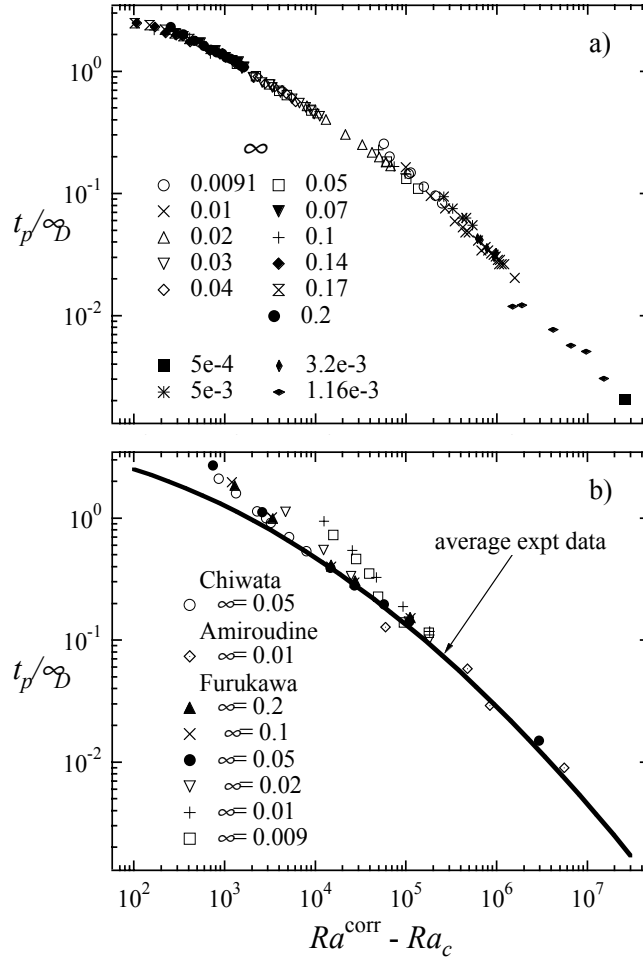


FIG. 5. The time of the first peak  $t_p$ , scaled by the diffusion time  $\tau_D$ , versus  $[Ra_{\text{corr}} - Ra_c]$ . a): The experimental data, where the symbols denote the various values of  $\epsilon$  at which the experiments were carried out. b): The curve representing the average of the experimental data from 5 a), compared with the results from simulations, shown as symbols at the various values of  $\epsilon$ .

and those in the present research are found to be internally consistent. However, contrary to the experimental results, the simulation data do not collapse on a single curve. This discrepancy is expected from the profiles  $\Delta T(t)$  shown in fig.1 where the peak in the simulations lies at substantially longer times  $t_p$  than for the experiments. A possible source for the discrepancy between simulations and experiments will be considered below.

## V. DISCUSSION

First we present general comments on transient observations in Rayleigh-Bénard convection. After the start of a heat current at constant pressure, an overshoot in  $\Delta T(t)$  is routinely observed in Boussinesq fluids. The origin of the overshoot is a certain “inertia” of the fluid immediately after the heat flux is applied: Even though the final state is convection, initially the fluid remains stationary and  $\Delta T(t)$  follows the solution of the thermal diffusion equation. As the fluid begins to move, the trace shows an overshoot with a peak at  $t_p$  followed by a transition to the steady state value in the convective regime as described, for example, by Behringer [13]. Thus,  $t_p$  approximately describes the time that it takes for the layer to develop convective motion.

In a compressible fluid, the non-convecting state during the initial transient is expected to persist up to a value  $\Delta T_{\text{instab}}$  greatly exceeding the stability threshold  $\Delta T_{\text{ons}}$  given by Eq.2, derived for a linear temperature and density distribution in the vertical direction. This result for  $\Delta T_{\text{instab}}$  was obtained by El Khouri and Carlès [14] via a linear stability analysis and is a direct consequence of the strongly inhomogeneous vertical density and temperature distribution with pronounced boundary layers generated by the Piston effect [15]. A clear example can be seen in Fig. 1(a) of ref. [4], which presents transient curves for  $\epsilon = 0.05$ . The simulated trace essentially coincides with the

zero-gravity result (Eq.3.3 in ref [4]) up to  $\Delta T(t)$  of order 280  $\mu\text{K}$ , while the stability criterion (Eq.2 in the present paper) gives only 7  $\mu\text{K}$ . Another example is obtained by comparing the simulations in Fig.2 of ref [5] at  $\epsilon = 0.01$  with calculations under zero gravity, which also shows the two curves coinciding until close to  $t_p$ . Hence the simulations [4,5] are qualitatively consistent with the predictions of linear stability analysis.

We now recapitulate the main findings of the comparison between experimental data and simulations for a supercritical very compressible fluid,  $^3\text{He}$ . Starting with  $t_{\text{osc}}$ , which is the characteristic time determined farthest away from the start of the heat flow, both experiments and simulations in the scaled representation are in good agreement. By contrast, as shown in Fig.5,  $t_p$  is systematically larger in the simulations than in the experiments, the difference becoming more important as  $\epsilon$  increases. An intriguing puzzle is why all the experimental  $t_p$  data at the various values of  $\epsilon$  can be cast into a scaling representation, while the simulation data cannot.

This disagreement for  $t_p$  is surprising: at large  $\epsilon$  where the compressibility of the fluid has become smaller, a “simple” Boussinesq behavior should be recovered. A possible origin of this discrepancy is the imperfection of the temperature control of the top plate during the experiment. The signal from the control thermometer [1] is recorded by a circuit with a time constant of 1.25 seconds and 6 dB/octave rolloff. Therefore, temperature fluctuations with frequencies above a few Hz cannot be detected. The average temperature noise is estimated to be about 1  $\mu\text{K}/\sqrt{Hz}$  r.m.s. Because of very high thermal conductivity of the top plate material (OFHC copper) it seems reasonable to assume that this perturbation produces no horizontal temperature gradients. It is therefore possible that small parasitic fluctuations of the top plate temperature could speed up the development of the convecting state, hence producing an overshoot with a smaller  $t_p$  than the simulations do, which have no noise. We would anticipate that once the convection is almost fully developed, the influence of the fluctuations mentioned above would not be noticeable any more. Hence they might not affect the period  $t_{\text{osc}}$  of the damped oscillations, which would explain the good agreement between experiment and simulations and also that in the steady-state condition [16].

We mention here that in the experiments [1] a rounding of the onset point on the steady-state  $\Delta T(q)$  measurements was reported and also attributed to the top plate noise. The rounding was found to become more and more pronounced as the critical point was approached, i.e. the effect of the fluctuations would have to be increasing with decreasing  $\epsilon$ . The effect of time-dependent boundary conditions on convection in a compressible fluid appears to be an interesting and open question. We suggest future studies, both experimental and numerical ones, that would focus on the transient response of a fluid layer in a R-B cell to an externally imposed perturbation of the top surface temperature.

## VI. CONCLUSIONS

A systematic comparison of the results from experimental and 2D simulation convection studies of a compressible fluid has been reported. This fluid is supercritical  $\text{He}^3$  along the critical isochore and over a temperature range where the compressibility varies by a factor of  $\approx 40$ . The temperature profile  $\Delta T(t)$  across the fluid layer in a Rayleigh-Bénard cell after the start of a heat flow was investigated in both experiments and simulations. The damped oscillations in the transient after the start of the heat flow, and with a period  $t_{\text{osc}}$  are of particular interest. They are a consequence of vertical mass flows that result from the “piston effect” triggered by the plumes - both moving up and down.

The comparison of the steady-state results, expressed in terms of the convection current versus the Rayleigh number, shows good agreement in general. However, the comparison of the transient results shows some systematic discrepancies, which appear to become more important as the compressibility decreases (i.e as the distance from the critical point increases). This can be seen clearly by examining the respective  $\Delta T(t)$  profiles at various temperatures. The agreement is best for the oscillation period where the simulation results and the experimental data can be represented in scaled form versus the Rayleigh number. The absence of noise in the simulations, in contrast to a physical system, might be a possibility for the discrepancy. In addition, as mentioned earlier in this paper, the simulations carried out independently by two research groups [4,5] do not detect the slow relaxation of  $\Delta T(t)$  to the steady state, or the region of “truncated oscillations” observed in the experiments. These discrepancies remain to be understood.

## VII. ACKNOWLEDGMENTS

The authors thank Fang Zhong for his efficient help with the formatting of several figures in this paper and the fitting of data sets. One of the authors (HM) is greatly indebted to S. Amiroudine and to P. Carlès for correspondence and discussions. The helpful comments of R. P. Behringer and P. Carlès on the manuscript have been greatly appreciated. The work is supported by the NASA grant NAG3-1838 and by the Japan Space forum H12-264.

## VIII. APPENDIX

### A. Boundary between regimes with damped and “truncated” oscillations.

It is useful to present this boundary in terms of the Rayleigh number difference  $[Ra_{\text{corr}}^{\text{bound}} - Ra_c]$  versus  $\epsilon$ , where the transformation from the former representation  $\Delta T_{\text{bound}}(\epsilon)$  to the present one was done via Eq.6 of ref. [2]. The zone diagram in this format shows that the boundary height remains constant at  $[Ra_{\text{corr}}^{\text{bound}} - Ra_c] = 700 \pm 200$  for  $0.05 < \epsilon < 0.2$ , and then rises steeply as  $\epsilon$  further decreases. This is shown in Fig.7.

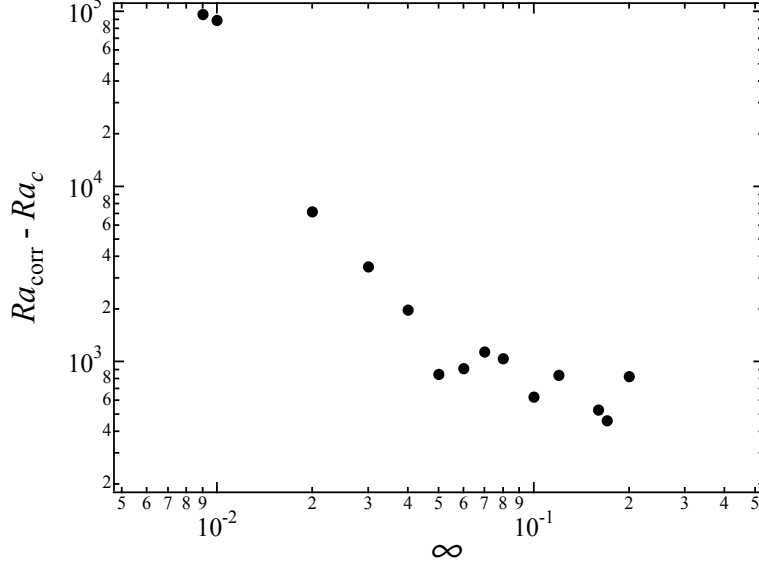


FIG. 6. The boundary between the regimes showing damped oscillations (top region) and truncated oscillations (bottom region), expressed in terms of  $[Ra_{\text{corr}} - Ra_c]$  versus  $\epsilon$ .

### B. The time $t_m$ in the profile $\Delta T(t)$

The discussion of  $t_m$ , the time defined in Fig.2, is more complex than for  $t_{\text{osc}}$  and  $t_p$ . In Fig. 7, both the results for  $t_m/\tau_D$  versus  $[Ra_{\text{corr}} - Ra_c]$  from the analysis of the experimental and the simulated transient profiles  $\Delta T(t)$  are presented. Both sets of results are clearly separated by a roughly constant amount on the vertical logarithmic scale. Hence we can use the same symbols for the values of  $\epsilon$  for the experiments and the simulation. For the sake of simplicity, we do not distinguish between the various authors in this figure. We note, however, that the simulation points for  $[Ra_{\text{corr}} - Ra_c] = 5.96 \times 10^4$  and  $4.78 \times 10^5$  at  $\epsilon = 0.01$  are those by Amiroudine [5]. Here, in contrast with  $t_{\text{osc}}$ , the  $t_m$  data from experiments show a small but systematic departure from collapsing on a single curve at the lower values of  $[Ra_{\text{corr}} - Ra_c]$ . However the scaled results from simulations at the various values of  $\epsilon$  collapse on one curve within the scatter. The trend is the same for both experimental and simulation data : the limiting slopes of the curves at the extremities of  $[Ra_{\text{corr}} - Ra_c]$  correspond to power laws with exponents of approximately  $n = -1$  and  $n = -0.5$ , respectively, at the low - and at the high end of the  $Ra$  numbers. This is shown in Fig.7.

We note that 1) the experimental data points for  $[Ra_{\text{corr}} - Ra_c]$  below the values of the boundary shown in Fig. 6 are in the regime of “truncated” oscillations. They form a smooth continuation of the curves at higher values of  $[Ra_{\text{corr}} - Ra_c]$ , namely in the regime of damped oscillations. 2) The experimental data for  $\epsilon \geq 0.07$ , which collapse on a single curve are those where the boundary in Fig.6 is at  $[Ra_{\text{corr}} - Ra_c] \approx \text{const} = 700$ . The departure from collapse from the first onto a second curve takes place when the boundary in Fig.6 begins to rise steeply for  $\epsilon \leq 0.07$ . 3) It is intriguing that the logarithmic vertical separation of the experimental and simulation curves corresponds to roughly a factor of 2. This means that for the same value of  $[Ra_{\text{corr}} - Ra_c]$ , the observed  $t_m$  has roughly twice the value of  $t_m$  from simulations.

The analysis of the experimental  $t_m$  data for the limit of low values of  $[Ra_{\text{corr}} - Ra_c]$  and the comparison with a simple predicted expression by Chiwata and Onuki [3] was already presented in Figs. 7 and 8 of ref. [2]. The exponent of -1 found both for the experiments and the simulations is consistent with the simple prediction.

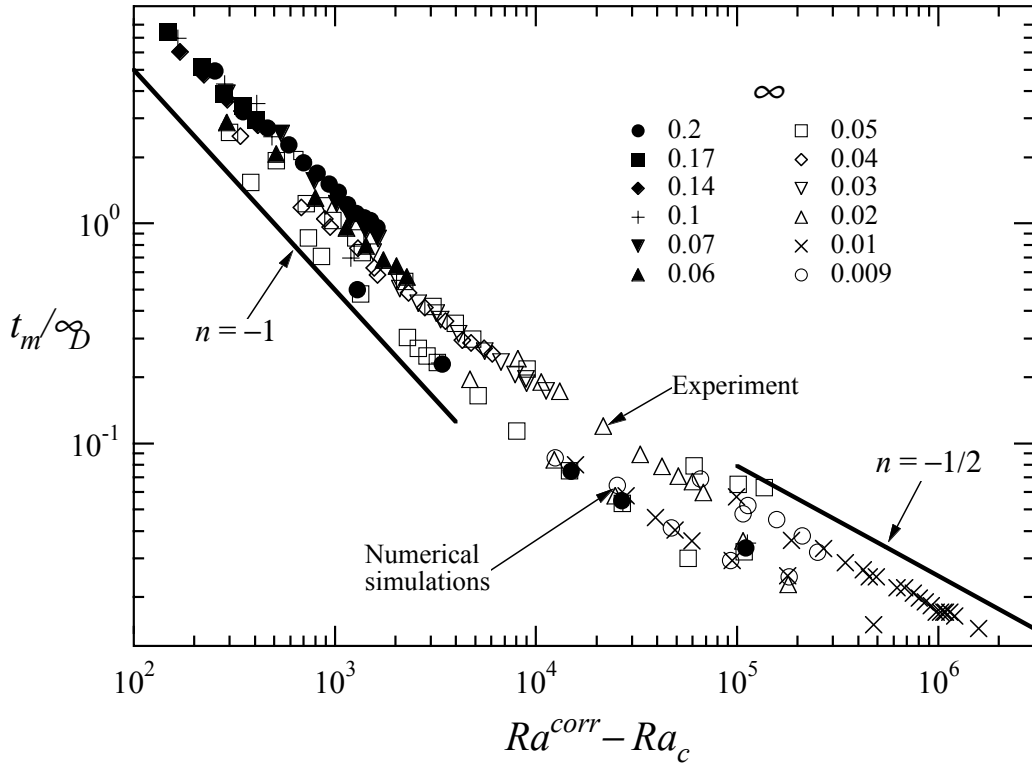


FIG. 7. The time  $t_m$  between the first peak and the first minimum, scaled by the diffusion time  $\tau_D$ , versus  $[Ra_{corr} - Ra_c]$ . The experimental data are located on the upper two almost overlapping trajectories of symbols. Those from the simulation, showing a collapse, are located on the lower trajectory of symbols. The symbols denote the various values of  $\epsilon$  at which both experiments and simulations were carried out.

- 
- [1] A.B. Kogan and H. Meyer, Phys. Rev. E **63**, 056310 (2001).
  - [2] H. Meyer and A.B. Kogan, Phys. Rev. E **66**, 056310 (2002).
  - [3] Y. Chiwata and A. Onuki, Phys. Rev. Lett. **87**, 144301 (2001).
  - [4] A. Furukawa and A. Onuki Phys. Rev. E **66**, 016302 (2002).
  - [5] S. Amiroudine and B. Zappoli, Phys. Rev. Lett. **90**, 105303 (2003), and S. Amiroudine (private communication).
  - [6] L.D. Landau and E.M. Lifshitz, Course of Theoretical Physics: Vol.6 Fluid Mechanics (Pergamon, Oxford, 1959)
  - [7] G. Ahlers, M. Cross, P. Hohenberg and S. Safran. J. Fluid Mech. **110**, 297 (1982).
  - [8] M. Gitterman and V. Steinberg, J. Appl. Math. Mech. USSR **34**, 305 (1971). M. Gitterman, Rev. Mod. Phys. **50**, 85 (1978).
  - [9] P. Carlès and B. Ugurtas, Physica D **126**, 69 (1999).
  - [10] D.J. Tritton, Physical Fluid Dynamics (Oxford Science, Oxford, 1988), Section 14.6.
  - [11] A. Schlueter, D. Lortz and F. Busse, J. Fluid Mech. **23**, 129 (1965).
  - [12] R.P. Behringer, A. Onuki and H. Meyer, J. Low Temp. Phys. **81**, 71, (1990).
  - [13] R.P. Behringer, Rev. Mod. Phys. **57**, 657 (1985).
  - [14] L. El Khouri and P. Carlès, Phys. Rev. E **66**, 066309 (2002).
  - [15] These authors have also estimated  $\Delta T_{instab}$  from an analysis of experimental data corrected for the instrumental time lag, and have found them to be consistent with their calculations for scenarios (a) and (b) where the initial rise of  $\Delta T(t)$  is not too rapid and the correction can be carried out (L. El Khouri and P. Carlès, to be published, private communication).
  - [16] The absence of noise in simulations, its presence in a physical system, and the resulting impact on the growth of perturbations in the convective state was pointed out to one of us (HM) by P. Carlès (private communication).

# **Fluctuations of the Phase Difference across an Array of Josephson Junctions in Superfluid $^4\text{He}$**

T. Chui, W. Holmes and K. Penanen  
Jet Propulsion Laboratory, California Institute of Technology

April 15, 2003

We present a formal thermodynamic treatment of superfluid flow in a Josephson junction. We show that the current and the phase difference are thermodynamic conjugate variables. We derive quantitative expressions for the rms fluctuations of these variables. Also, we discuss the thermodynamic stability and the thermal activation to the phase slip region. We apply the developed formalism to show why an array of apertures in  $^4\text{He}$  can exhibit the Josephson effect near the Lambda transition despite strong thermal fluctuations.

## **Metglas 2714A for Low Temperature Transformer Core and EMI Filter**

Hung Quach and Talso Chui

Jet Propulsion Laboratory, California Institute of Technology

April 14, 2003

We have measured the real and imaginary parts of the relative permeability of Metglas 2714A. The magnetization noise density of a toroid made of this material is also measured with a SQUID magnetometer. This noise density is found to agree very well with the fluctuation dissipation theorem, implying that superconducting transformers with predictable noise characteristic can be designed. We also find that the relative permeability is larger than 10,000 at liquid helium temperature and at frequencies from DC to 100 kHz, making it suitable to be used as EMI filter material. Its usage should be similar to that of ferrites, with the exception that it is also effective at low temperatures.



# ‘Heat from Above’ heat capacity measurements in liquid $^4\text{He}$

R. A. M. Lee(1), A. Chatto(1), D. A. Sergatskov(2), A. V. Babkin(2), S. T. P. Boyd(2)  
A. M. Churilov(2), T. D. McCarson(2), T. C. P. Chui(3), P. K. Day(3), R. V. Duncan(2)  
and D. L. Goodstein(1)

(1) *California Institute of Technology (Pasadena, USA)*, (2) *University of New Mexico (Albuquerque, USA)*,  
(3) *Jet Propulsion Laboratory, California Institute of Technology (Pasadena, USA)*

We have made heat capacity measurements of superfluid  $^4\text{He}$  at temperatures very close to the lambda point,  $T_\lambda$ , in a constant heat flux,  $Q$ , when the helium sample is heated from above. In this configuration the helium enters a self-organized (SOC) heat transport state [1] at a temperature  $T_{SOC}(Q)$ , which for  $Q \geq 100 \text{ nW/cm}^2$  lies below  $T_\lambda$ . At low  $Q$  we observe little or no deviation from the bulk  $Q = 0$  heat capacity up to  $T_{SOC}(Q)$ ; beyond this temperature the heat capacity appears to be sharply depressed, deviating dramatically from its bulk behaviour. This marks the formation and propagation of a SOC/superfluid two phase state, which we confirm with a simple model. The excellent agreement between data and model serves as an independent confirmation of the existence of the SOC state. As  $Q$  is increased (up to  $6 \mu\text{W/cm}^2$ ) we observe a  $Q$  dependant depression in the heat capacity that occurs just below  $T_{SOC}(Q)$ , when the entire sample is still superfluid. This is due to the emergence of a large thermal resistance in the sample, which we have measured and used to model the observed heat capacity depression. Our measurements of the superfluid thermal resistivity are a factor of ten larger than previous measurements by Baddar *et al.*[2].

[1] W. A. Moeur, P. K. Day, F-C. Liu, S. T. P. Boyd, M. J. Adriaans and R. V. Duncan, *Phys. Rev. Lett.* **78**, 2421 (1997).

[2] H. Baddar, G. Ahlers, K. Kuehn and H. Fu, *J. Low Temp. Phys.* **119**, 1 (2000).



The University of New Mexico

# 'Heat from Above' heat capacity measurements in liquid in $^4\text{He}$

Richard A. M. Lee (Caltech)

-----

This work has resulted from development of:

## **The CQ Experiment**

David L. Goodstein (Caltech) – Principal Investigator

Robert V. Duncan (U.N.M.)

Talso C. P. Chui (J.P.L.)

Peter K. Day (J.P.L.)

-----

Andrew R. Chatto, Dmitri A. Sergatskov, Alex V. Babkin,  
Stephen T. P. Boyd, Alexander M. Churilov, 'T. D.' McCarson

# The CQ Experiment:

## Enhanced Heat Capacity of Superfluid Helium in a Heat Flux

---

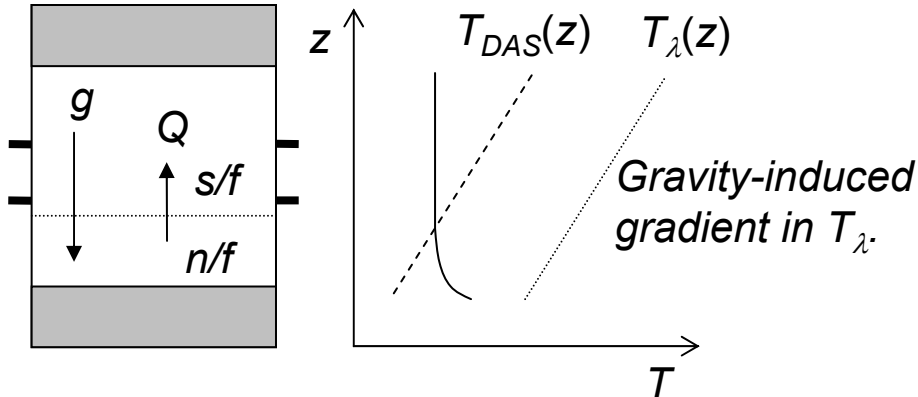
- Guest experiment on DYNAMX (critical dynamics in  $\mu\text{g}$ ).
- NASA flight experiment.
- 2008 flight on International Space Station ( $\mu\text{g}$  environment).

### Purpose:

- Test predictions of the dynamic renormalization group theory.
- When one applies a heat flux,  $Q$ , to a sample of superfluid:
  - Transition temperature is depressed,  $T_c(Q) < T_\lambda$
  - Heat capacity is enhanced,  $\Delta C_Q = C_Q - C_0$ , and diverges at  $T_c(Q)$
- Ground-based experiments (disagree with theory):
  - $T_{DAS}(Q) < T_c(Q)$ , **D**uncan, **A**hlers and **S**teinberg, *PRL*, **60**, 1522(1988).
  - $\Delta C_{Q\_Harter.} \approx 10 \times \Delta C_{Q\_theory}$ , Harter *et al.*, *PRL*, **84**, 2195 (2000).

# 'Heat from Below or Above' – ground based

## – 'Heat from Below' configuration

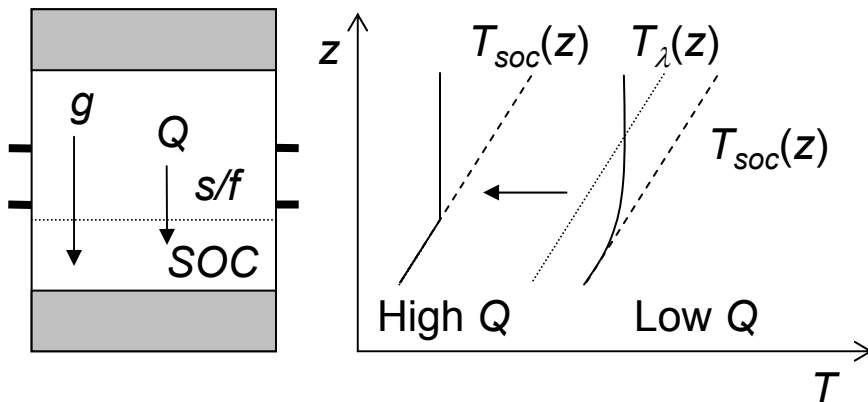


$g$  = gravity,  $Q$  = Heat flux,  $z$  = height

- 'Heat from Above' produces:
- **Self Organized Critical State:**  
Mouere *et. al.*, *PRL*, **78**, 2421 (1997)
- At low  $Q$  the SOC state exists on the normal-fluid side of  $T_{\lambda}$ , where the diverging thermal conductivity causes the sample to 'self-organize' at a fixed reduced temperature from  $T_{\lambda}$ .

– For  $Q < 0.1 \mu\text{W}/\text{cm}^2$ :  $T_{\text{soc}} > T_{\lambda}$

## – 'Heat from Above' configuration



$$\kappa(Q, t_{\text{soc}}) = \frac{|Q|}{\nabla T_{\lambda}}$$

– For  $Q > 0.5 \mu\text{W}/\text{cm}^2$ :  $T_{\text{soc}} \approx T_{\text{DAS}}$

$$t_{\text{soc}}(Q) = \frac{T_{\lambda} - T_{\text{soc}}}{T_{\lambda}} = \left( \frac{Q}{638 \text{ W}/\text{cm}^2} \right)^{0.813}$$

# Measurement technique

- Heat pulse method

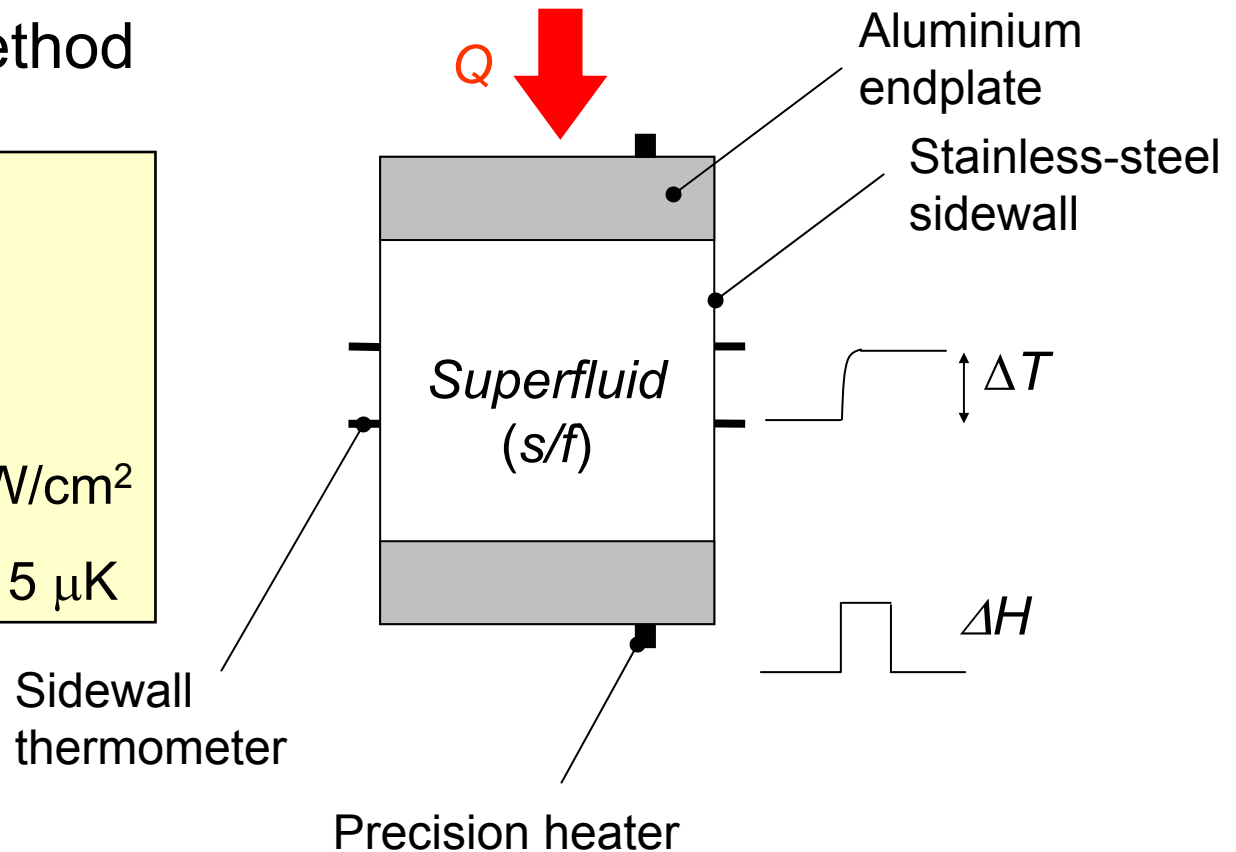
$$C = \Delta H / \Delta T$$

$$\Delta H = 500 \text{ nJ}$$

$$\Delta T = 30 \text{ nK}$$

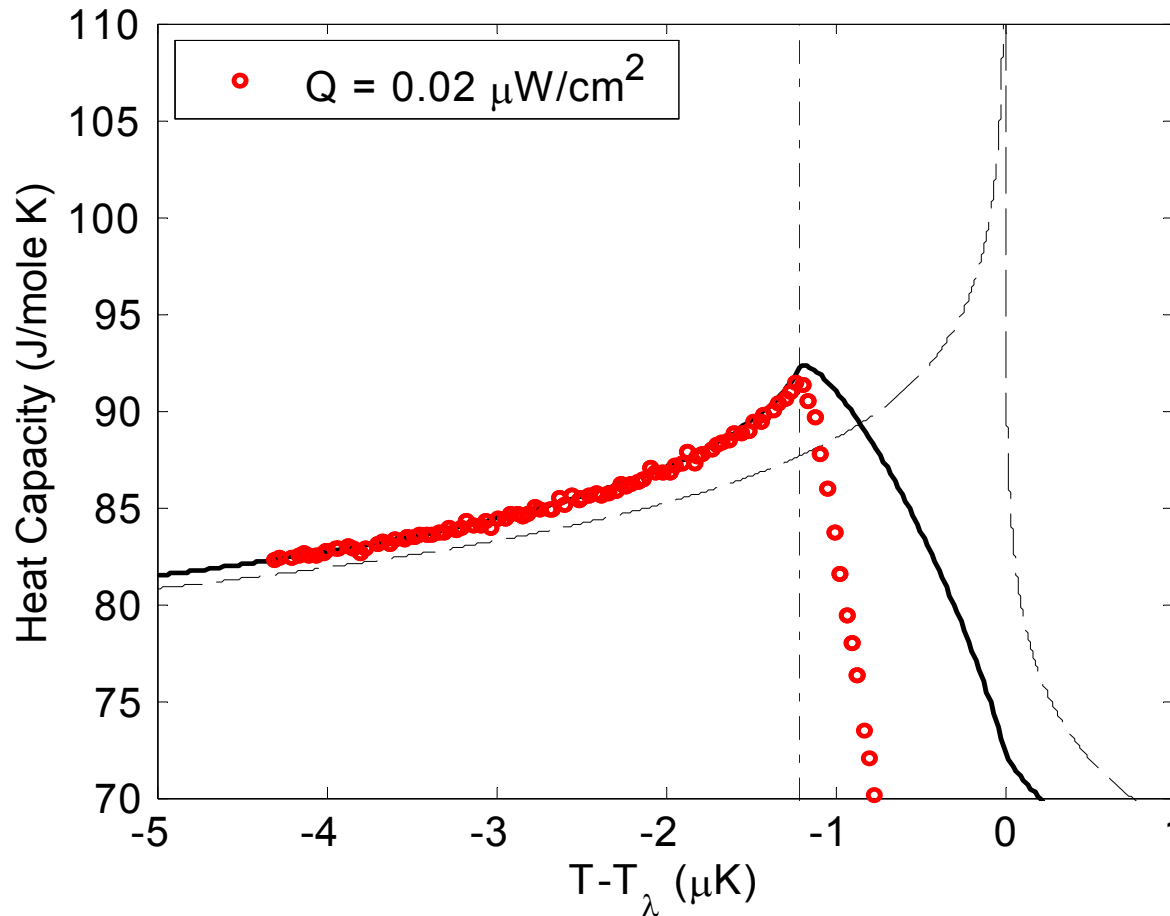
$$Q \text{ range: } 0 - 6 \text{ } \mu\text{W}/\text{cm}^2$$

$$T \text{ range: } T_\lambda - T \leq 5 \text{ } \mu\text{K}$$



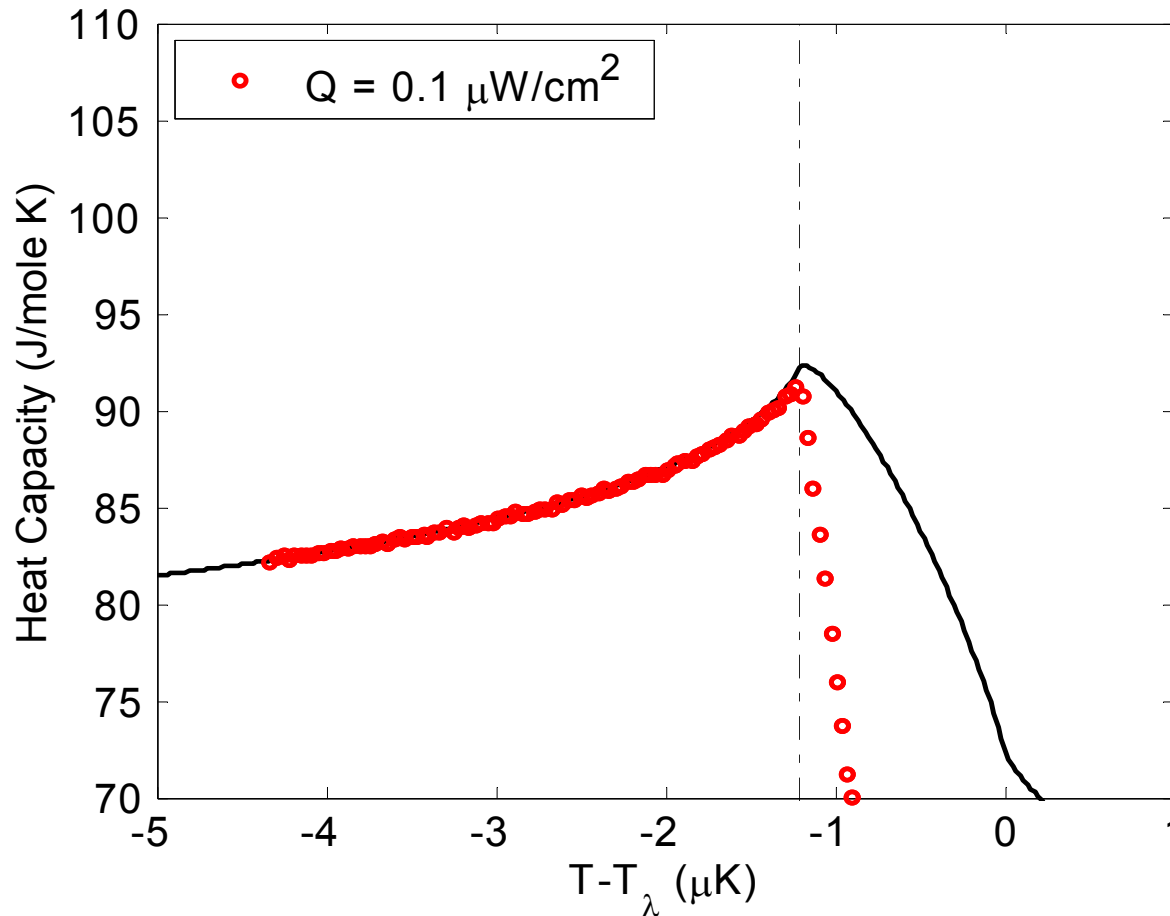
- Pulse sample, raising its temperature, until  $T = T_{soc}(Q)$ , and look for  $\Delta C_Q$ .

# Results - 'Heat from Above'



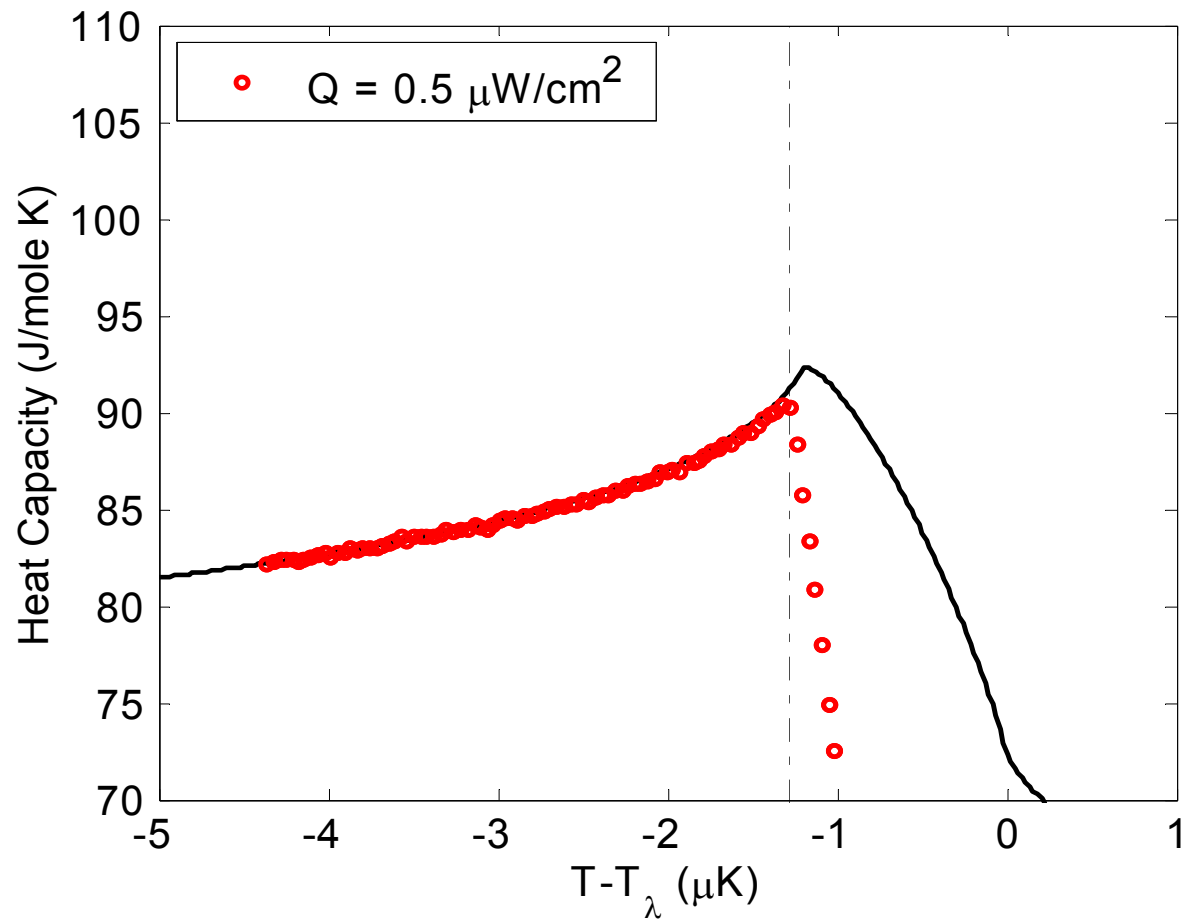
- Sample depth = 9 mm, so  $T_\lambda(\text{top}) - T_\lambda(\text{bottom}) = 1.2 \mu\text{K}$
- Severe gravity rounding (black line). Compare with  $\mu g$  (dashed line).

# Results - 'Heat from Above'



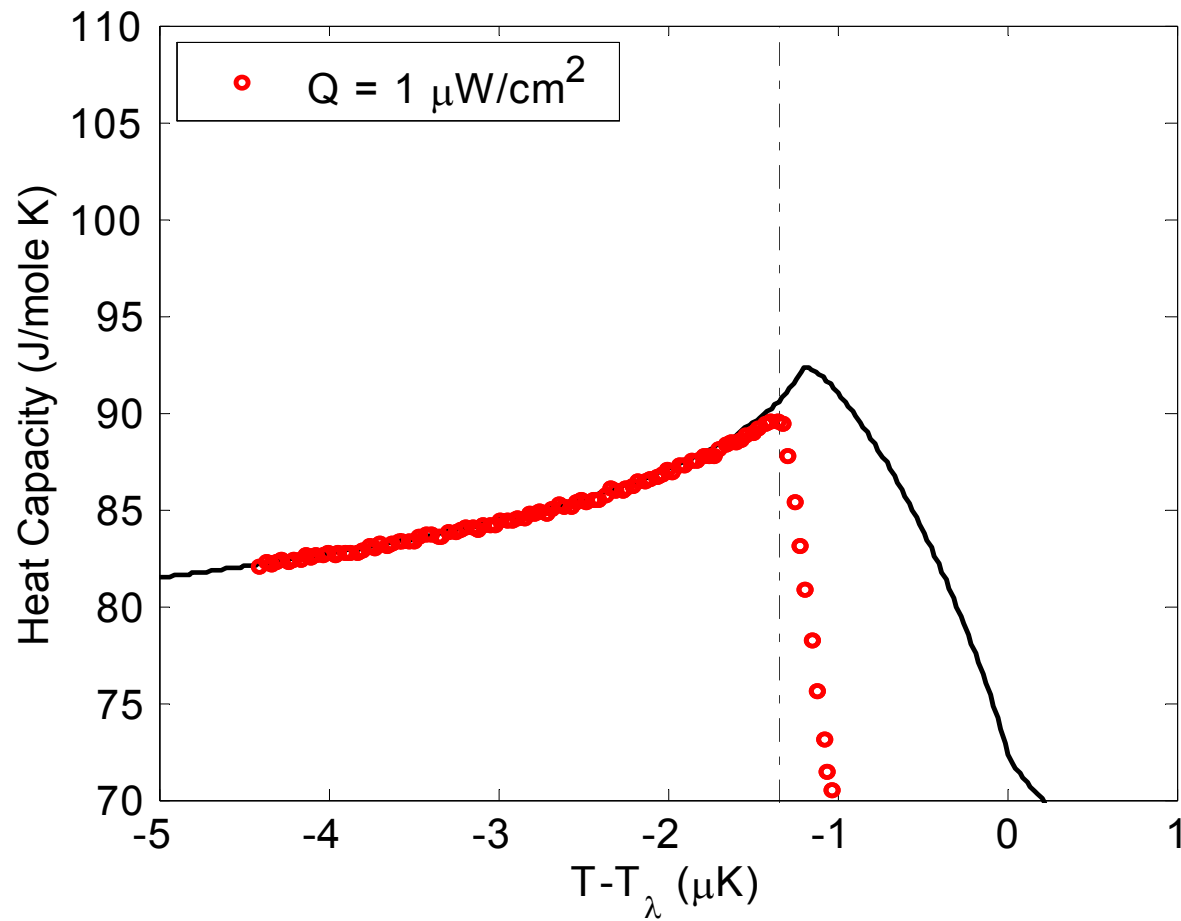
- Red circle points = 'Heat from Above' heat capacity data.
- Black line = calculated gravity rounded,  $Q = 0$ , heat capacity
- Dot-dashed line = measured  $T_{\text{soc}}^{34}(Q)$ .

# Results - 'Heat from Above'

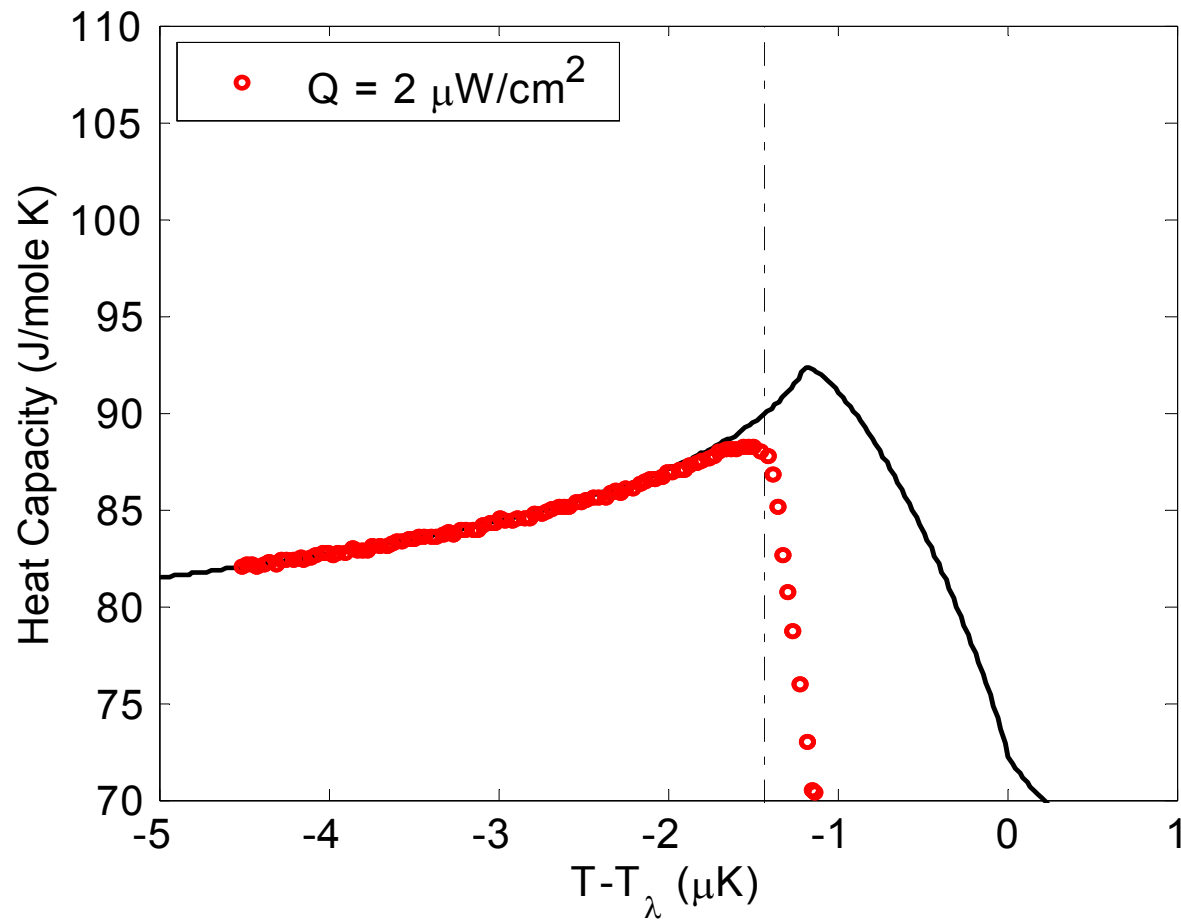




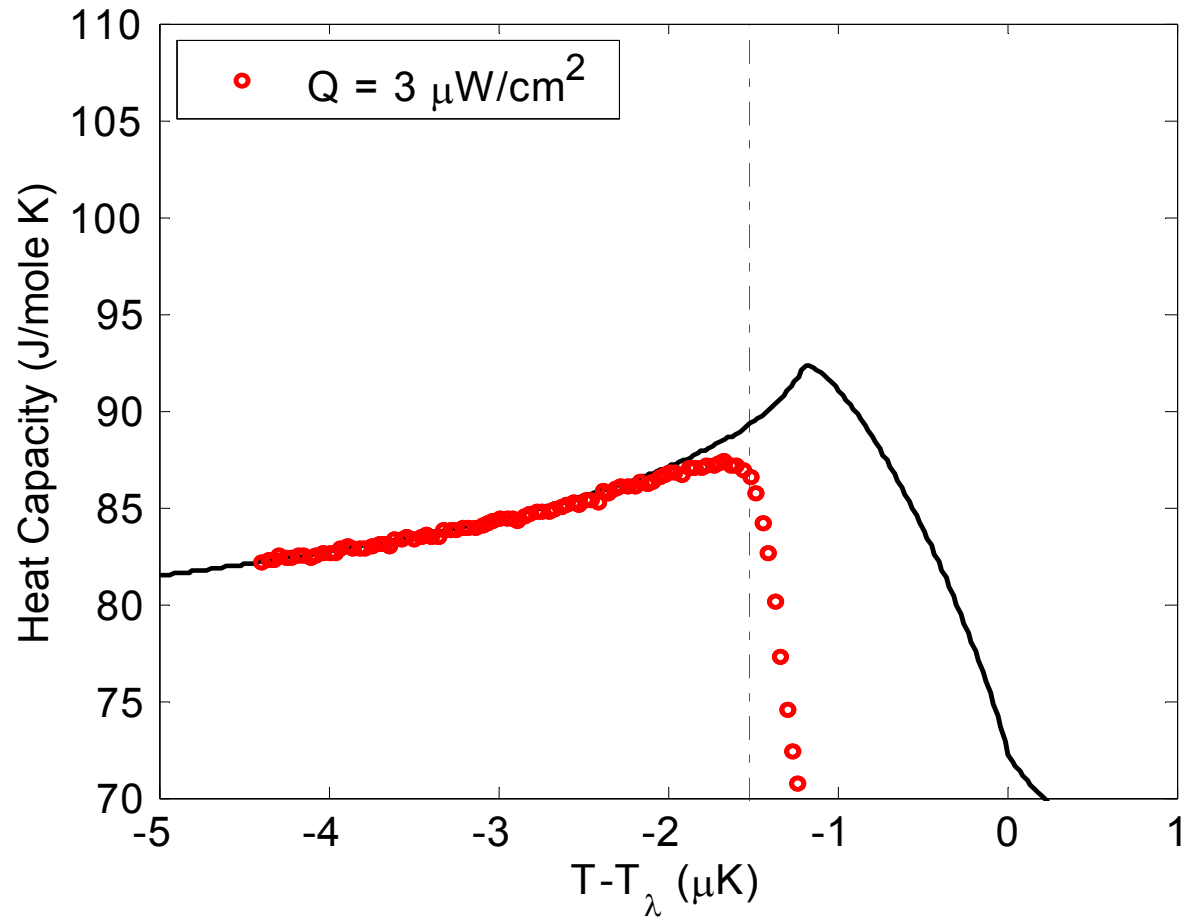
# Results - 'Heat from Above'



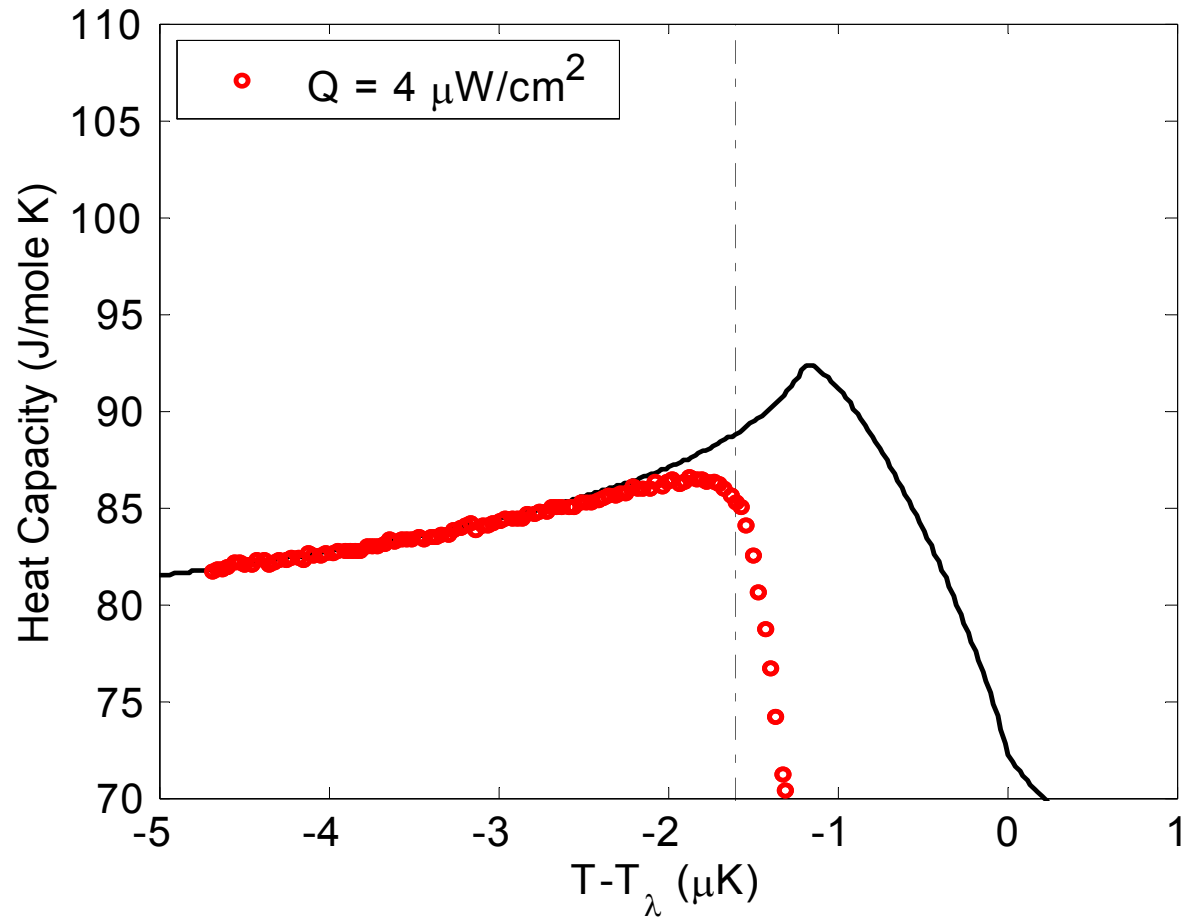
# Results - 'Heat from Above'



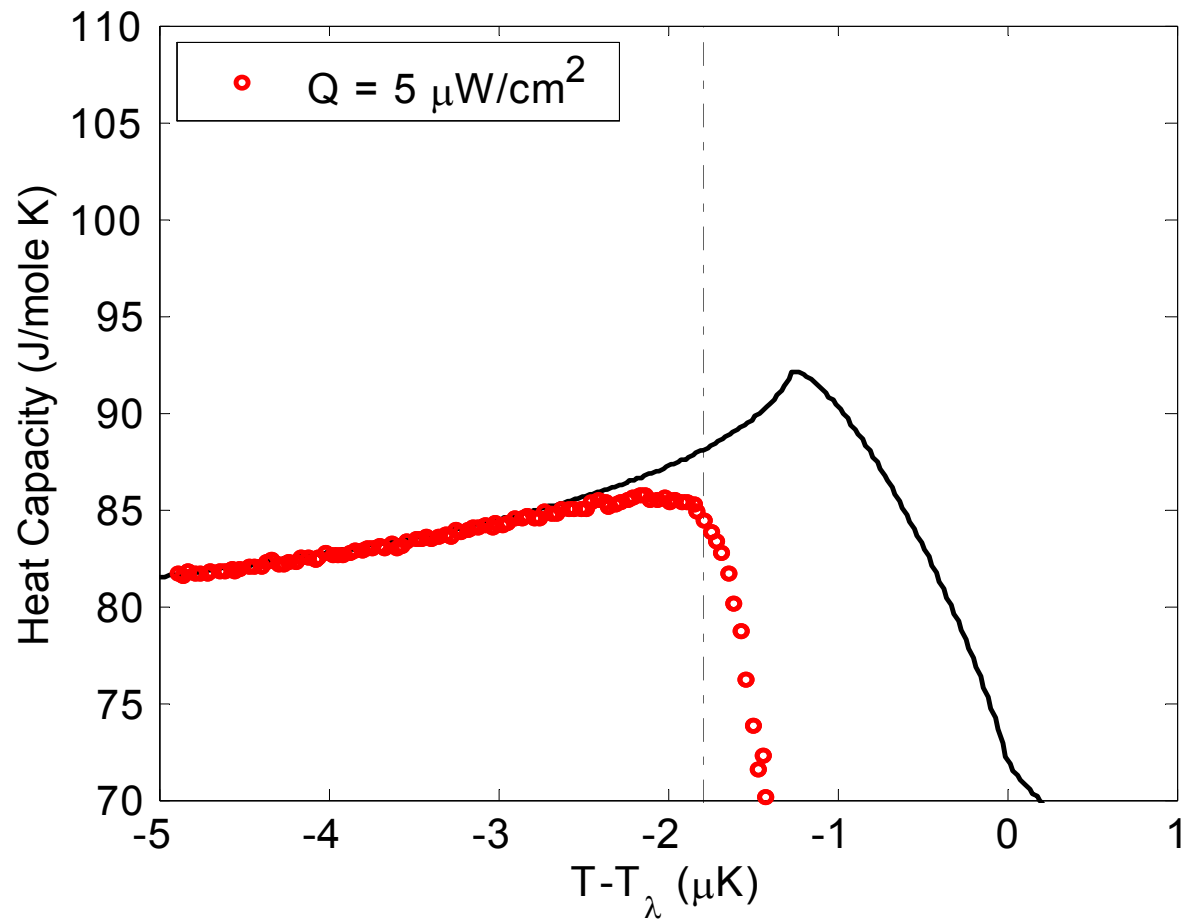
# Results - 'Heat from Above'



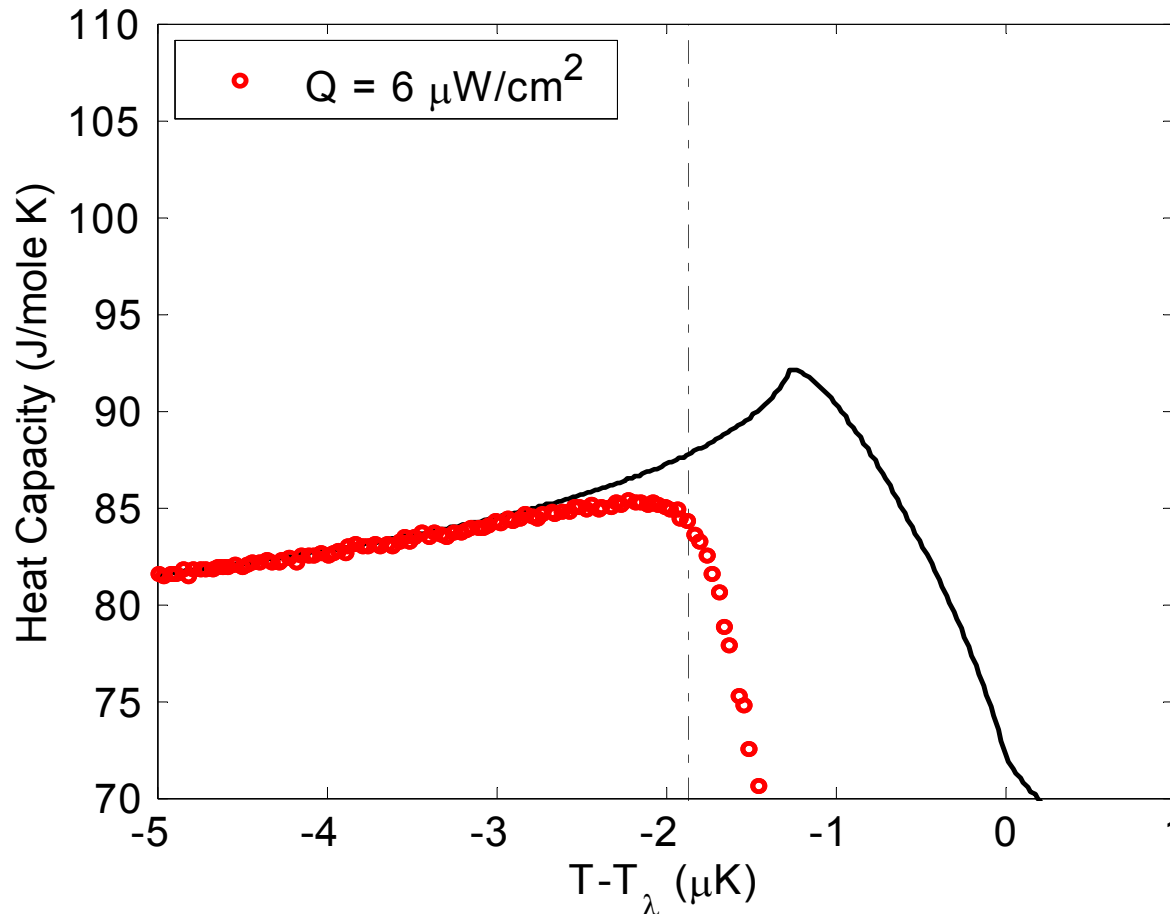
# Results - 'Heat from Above'



# Results - 'Heat from Above'



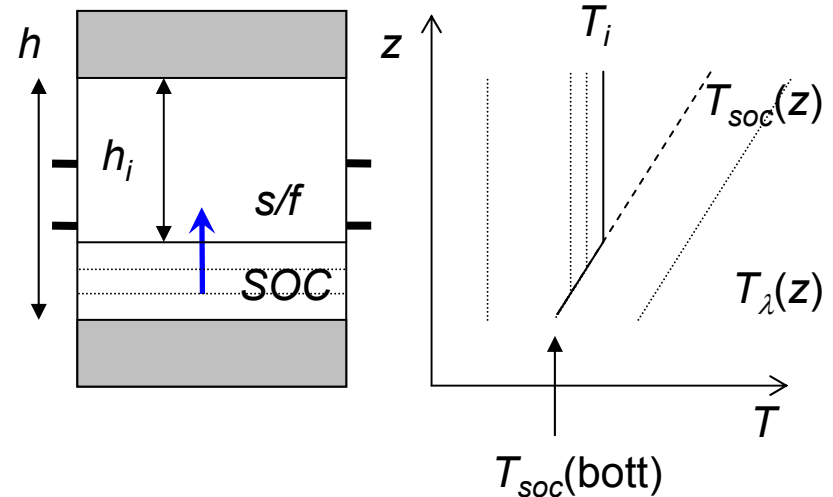
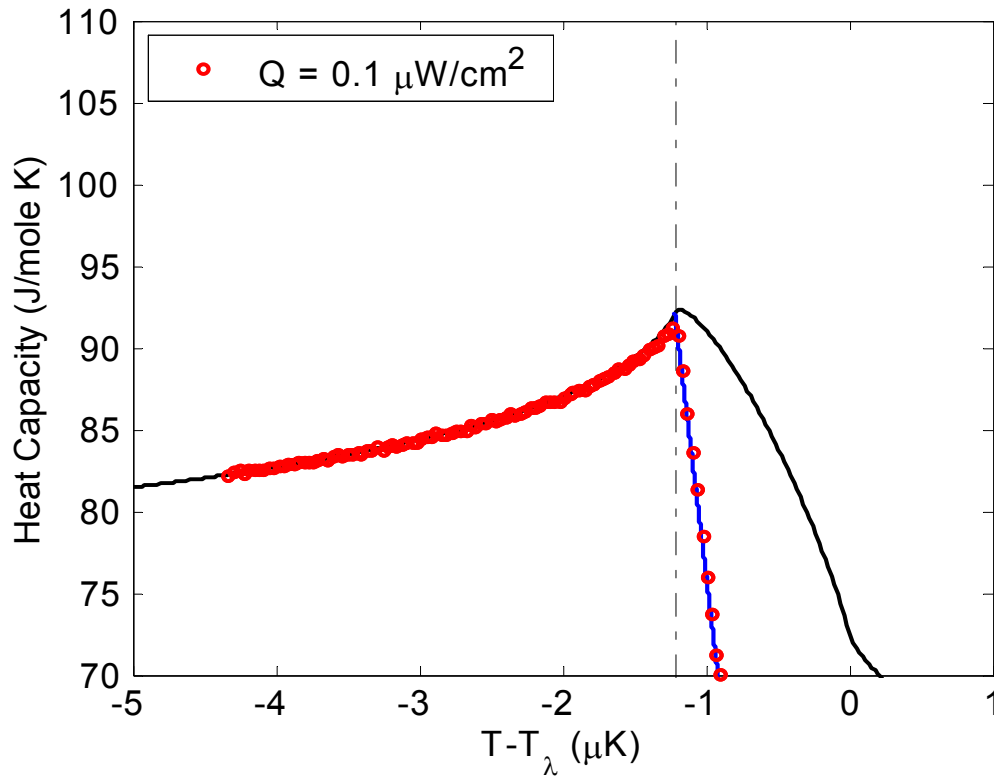
# Results - 'Heat from Above'



- Our measured  $T_{\text{soc}}(Q)$  agrees with Moeur *et al.*, for  $Q > 0.5 \mu\text{W}/\text{cm}^2$ :

$$t_{\text{soc}}(Q) = \left( \frac{Q}{Q_0} \right)^{0.813}, \quad Q_0 = 745 \pm 39 \text{ W}/\text{cm}^2, \quad Q_0 = 638 \pm 178 \text{ W}/\text{cm}^2 \text{ (Moeur et al.)}$$

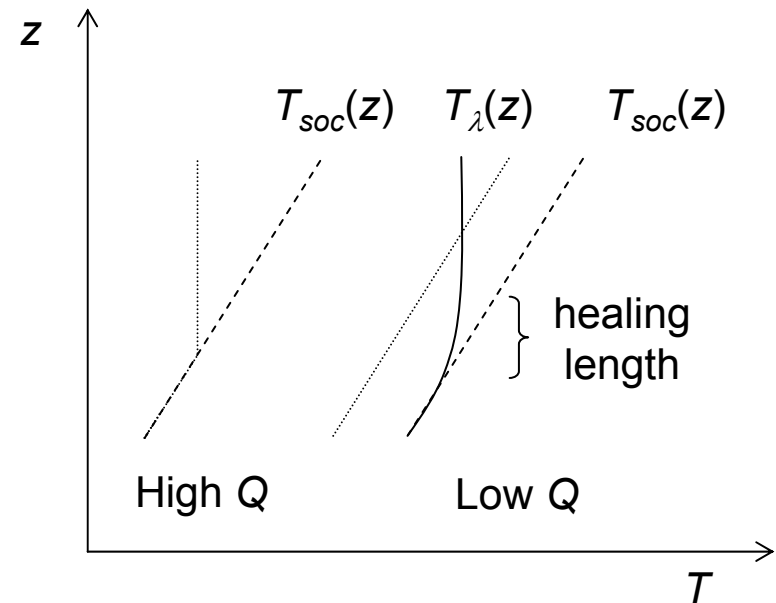
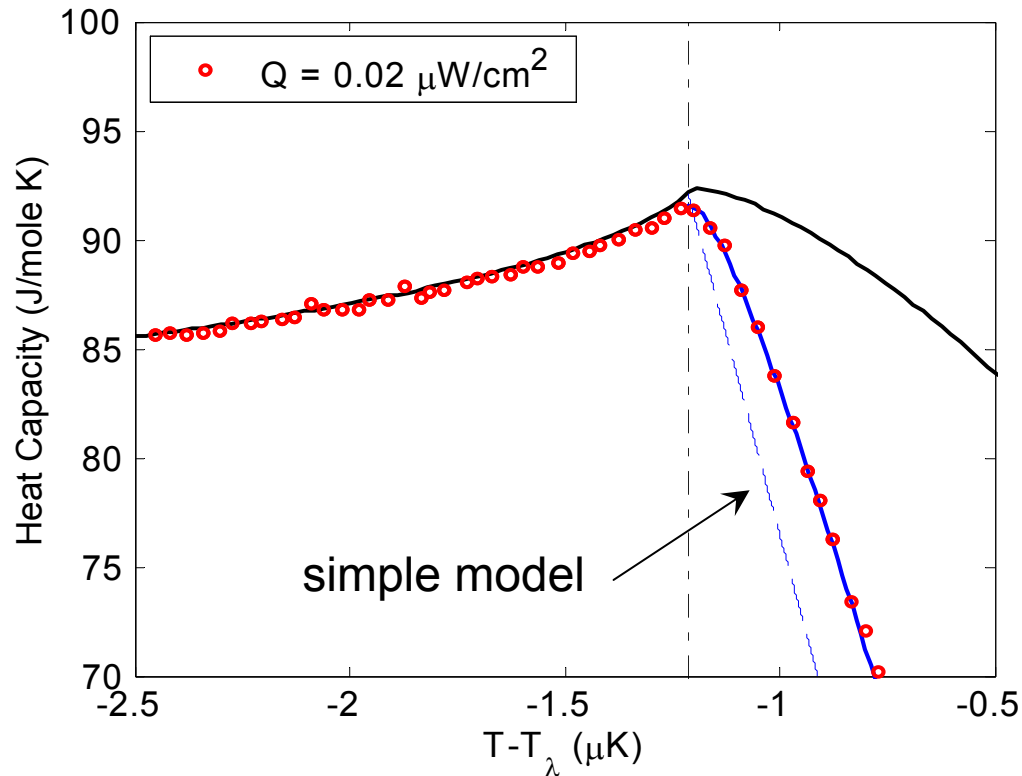
# Explanation – the sharp depression



$$c_{\text{model}}(T_i) = c_{s/f}(T_i, h_i) \cdot \frac{V_i}{V}$$

- This is due to an advancing SOC/superfluid interface. We can model this:
  - Assume the sample's heat capacity is dominated by the shrinking superfluid phase, with zero heat capacity contribution from the SOC phase.
  - Reasonable assumption:  $t_{\text{SOC}}$  is fixed because  $Q$  is fixed, therefore the SOC state does not absorb any of the heat pulse energy.
  - The model (blue line) works very well for  $Q = 1$  to  $0.1 \mu\text{W}/\text{cm}^2$ , however ...

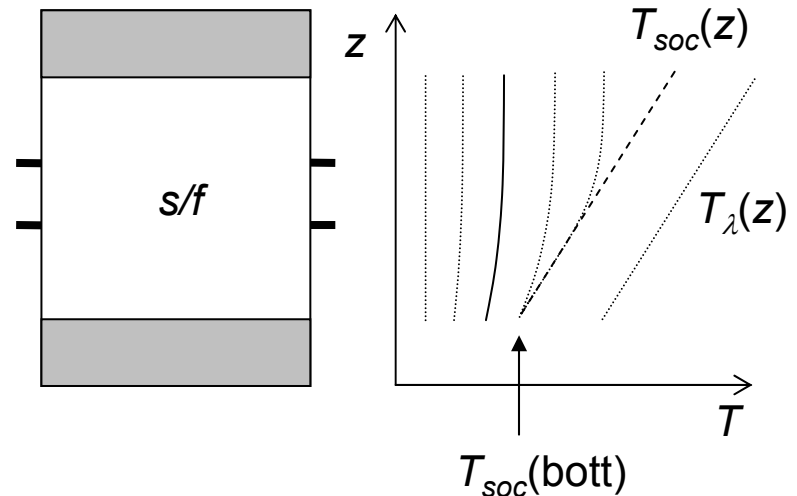
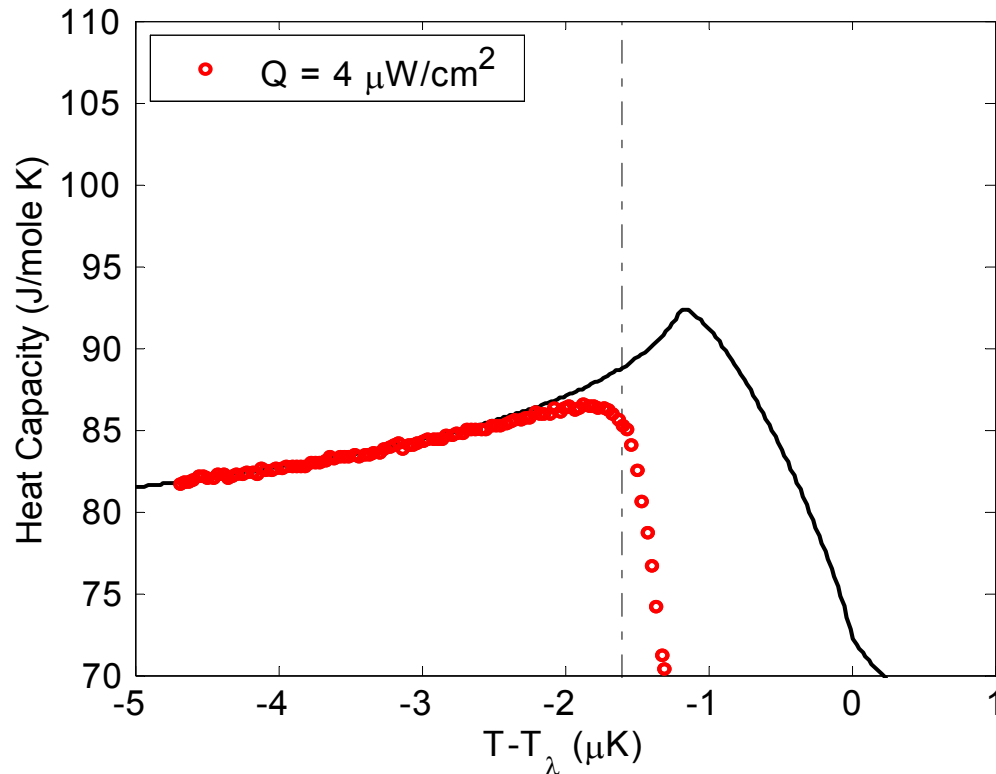
# Simple model fails at low Q due to the 'healing length'



- For  $Q < 0.1 \mu\text{W}/\text{cm}^2$  ( $T_{\text{soc}} > T_\lambda$ ) develop a 'healing length' between SOC/normal-fluid, due to the finite  $\kappa$ . Also observed by Moeur *et al.*
- We can model this:
  - Integrate the heat flow equation:  $\nabla T = -Q/\kappa(Q, t)$ , using  $\kappa(t) = \kappa_0 t^{-x}$ .
  - We generate a thermal profile  $\rightarrow$  increment  $T \rightarrow$  generate a new thermal profile  $\rightarrow$  integrate total energy  $\rightarrow$  compute heat capacity point  $\rightarrow$  repeat ...
  - Improved model = **blue line**.  $\kappa_0$  the only adjustable parameter.



# The Q dependant depression

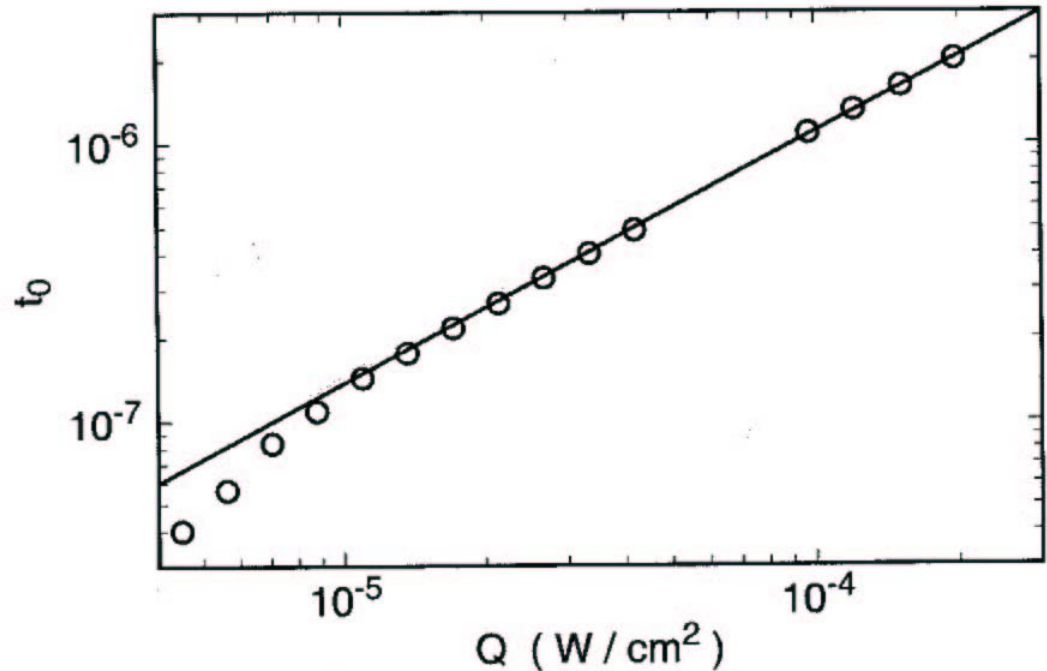


- Remember CQ is looking for an enhancement and we see a depression, why?
- Well, the depression occurs in the superfluid phase for  $T < T_{\text{soc}}(\text{bott})$ 
  - Maybe it's due to a large superfluid thermal resistivity causing a thermal gradient in the sample and a reduced bulk heat capacity?

# Previous s/f thermal resistivity measurements

- Baddar *et al.*, *J. Low Temp. Phys.*, **119**, 1 (2000)
  - ‘Heat from Below’ experiment. For  $Q \geq 10 \mu\text{W}/\text{cm}^2$ , they observed a power law behaviour:

$$R = \left( \frac{t}{t_0} \right)^{-2.8} \text{ K cm/W}$$
$$t_0 = \left( \frac{Q}{393 \text{ W/cm}^2} \right)^{0.904}$$



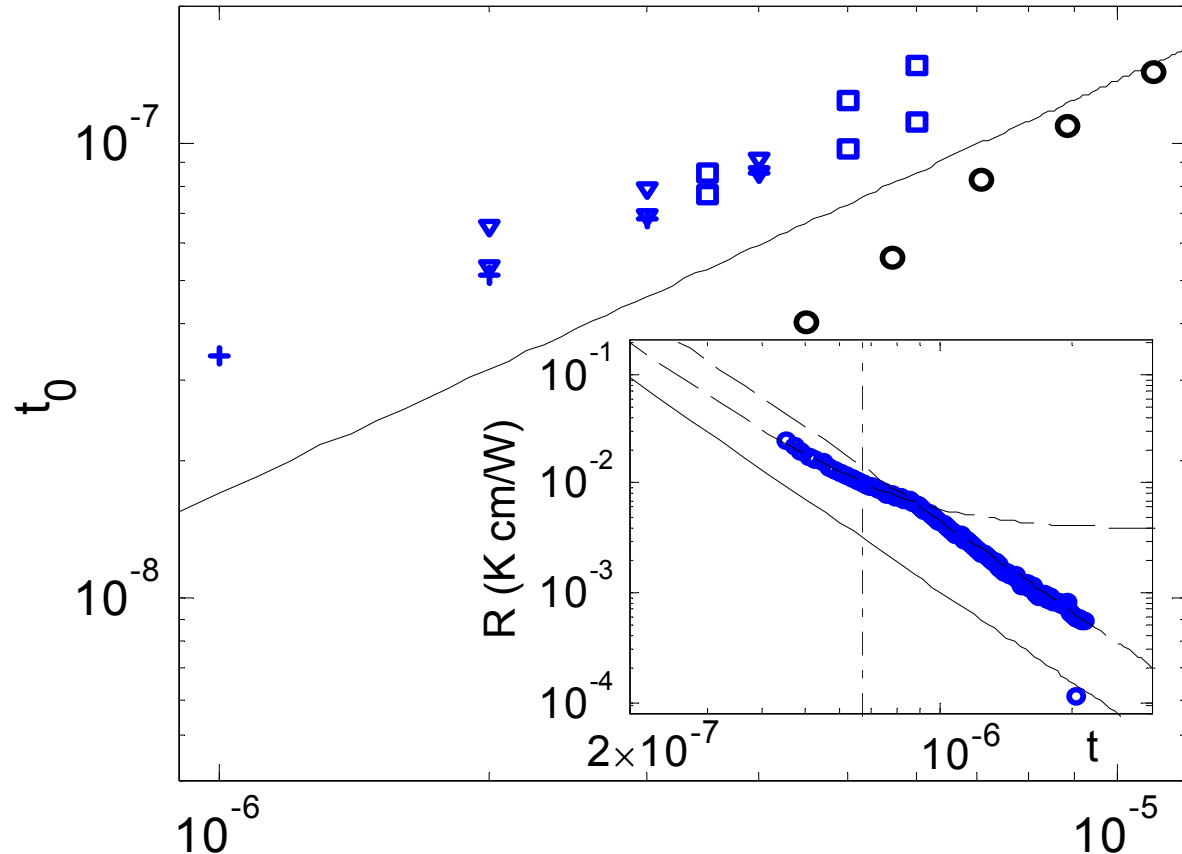
- However, these previous measurements proved to be too small to explain our observed depression.
- We made our own measurements, using the sidewall thermometers.

# s/f thermal resistivity measurements

- We fit our data to  $R = (t/t_0)^{-2.8}$  and extracted  $t_0$  at each value of  $Q$ .

Sample heights:

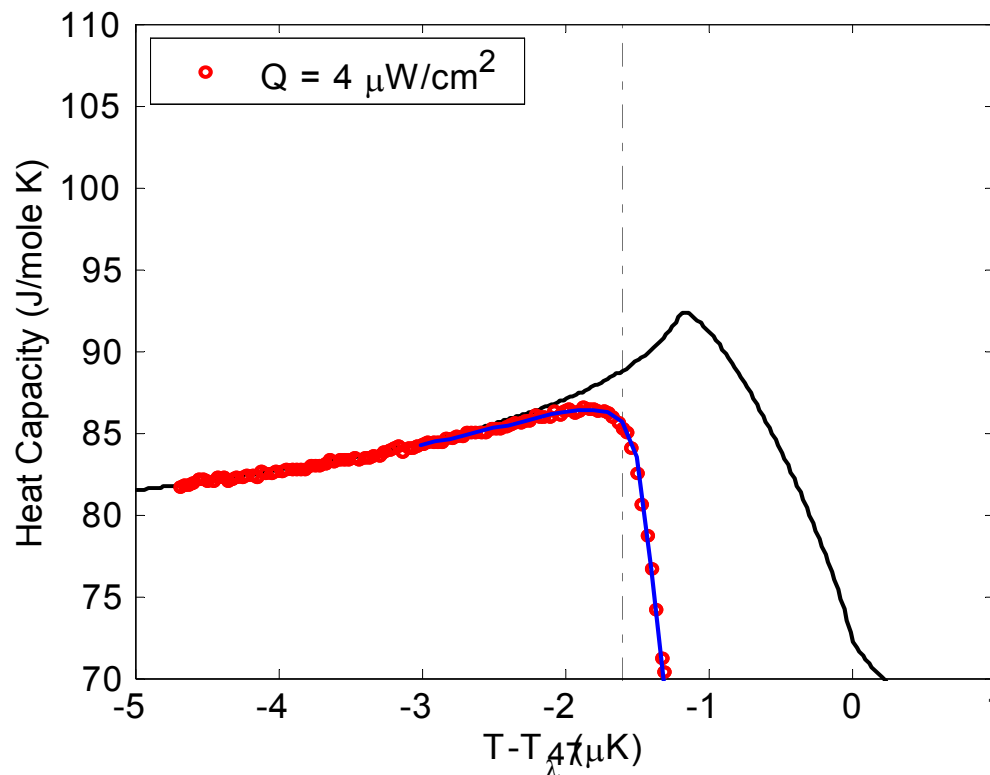
- 1.060 cm
- ▽ 0.989 cm
- + 0.940 cm



- We observe a larger  $R \sim t_0^{2.8} \approx 10 \times R_{Baddar}$
- In addition, our high  $Q$  data show a clear change in thermal resistivity (insert: data at  $Q = 6 \mu\text{W}/\text{cm}^2$ ), giving two values of  $t_0$  at each value of  $Q$ .

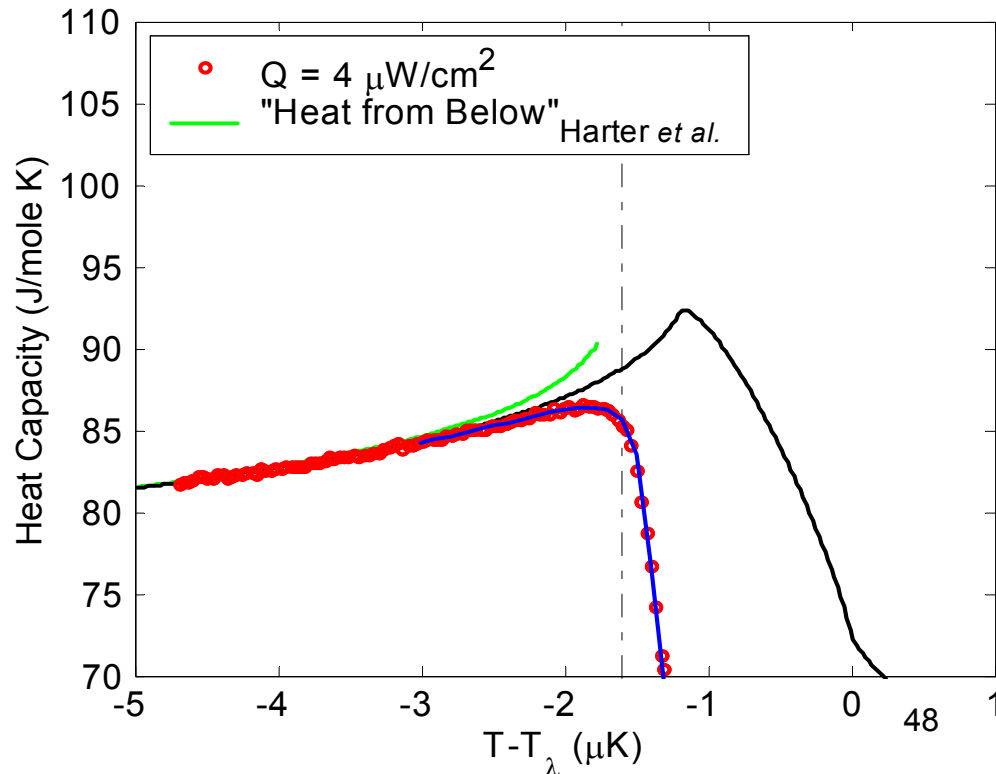
# Explanation – the $Q$ dependant depression

- So the depression is due to an anomalously large superfluid thermal resistivity. Again, we can model this:
  - As before we integrate the heat flow equation,  $\nabla T = -Q/\kappa(Q, t)$ , using our measured  $\kappa(Q, t)$ .
  - The model works very well for all of our data (blue line).



# Interesting implication

- In our model, when we integrate the total energy, we use the  $c_{Q=0}$  (black line) and not the enhanced  $c_{Q\_Harter}$  (green line) - Harter *et al.*, *PRL*, **84**, 2195 (2000).
  - This implies that in ‘Heat from Above’ experiments there is no, or very little, heat capacity enhancement.
  - It does not rule out  $c_{Q\_theory}$  that may still be there, but which would be too small to resolve due to gravity rounding.



$$c_{\text{model}} = \frac{\text{Total Energy}}{n \cdot \Delta T}$$

$$c_{\text{model}} = \frac{1}{n \cdot \Delta T} \cdot \sum_i^N n_i \cdot \Delta T_i \cdot c_{Q=0}(T_i)$$

# Conclusions

---

We have made the first measurements of the heat capacity of liquid  $^4\text{He}$  in a 'Heat from Above' configuration:

- We can explain all the features of our data.
- Our measurements provide independent confirmation of the existence of the Self Organized Critical state.
- We are in agreement with Mouer *et al.*, *PRL*, **78**, 2421 (1997).
  - We measure the same  $t_{\text{soc}}(Q)$  dependence,
  - and observe 'healing length' effects at low  $Q$  values.

# Conclusions

---

Our 'Heat from Above' measurements differ with those made in 'Heat from Below' as follows:

1. Our modelling implies no large heat capacity enhancement
  - Harter *et al.*, *PRL*, **84**, 2195 (2000).
2. We observe a large superfluid thermal resistivity
  - 10x larger than Baddar *et al.*, *J. Low Temp. Phys.*, **119**, 1 (2000).
3. We observe a sharp kink/change in  $R$ , seen clearly in our deeper samples and at large  $Q$  values.

This leads to the question:

- Why do such seemingly similar experimental configurations produce such different behaviour .... ?

## Specific Heat and Second Sound Measurements with the DYNAMIX Instrument

Joel Nissen  
Stanford University

In addition to its primary role of studying non-linear heat transport effects near the lambda transition of  $^4\text{He}$ , the DYNAMIX apparatus is suitable for measurements of the specific heat and the velocity of second sound. We plan to take advantage of available time on orbit to make measurements in these areas near to the lambda transition. The specific heat work would be similar to LPE, aimed at improving our knowledge of the singularity in the bulk heat capacity at the transition, but would provide more accurate results close to the transition. It would focus roughly equally on each side of the transition and would be synergistic with the CQ experiment, providing wider-range data at  $Q = 0$ . The second sound measurements are made possible by the fast time constant and high resolution of the DYNAMIX thermometers, which allow accurate time-of-flight measurements of second sound pulses. It appears possible to measure the second sound velocity to about 1% at a reduced temperature of  $t = 5 \times 10^{-8}$  by averaging over a moderate number of pulses. The data would complement and extend earlier ground-based measurements, leading to improved tests of the theory of static critical phenomena at the lambda transition.



## **Nonlinear Dynamics of the Superfluid Transition: What may we learn on orbit?**

Rob Duncan  
University of New Mexico

Linear response (specifically, Fourier's Law) in  $^4\text{He}$  has been observed to fail in heat flow experiments near the superfluid transition. A detailed analysis of the data suggests that the hydrostatic pressure gradient across the helium column limits the divergence of the correlation length in our earth-based experiments. This is consistent with other observations, such as the surprising lack of mutual friction and hysteresis near the superfluid transition, and a 'rounding' of the transition that appears to be independent of heat flux in the low heat flux limit. I will discuss these unusual results from earth-based measurements, and will show predictions for the very different results that may result when we make our measurements on orbit as part of the M1 Mission of the Low-Temperature, Microgravity Physics Facility. This work has been funded by the Fundamental Physics Discipline within the Physical Sciences Research Office of NASA, and is conducted by the DYNAMX (UNM) and CQ (Caltech) Groups, with assistance from the Low Temperature Science and Quantum Sensors Group at JPL.

## Precise heater control with rf-biased Josephson junctions

Colin J. Green, Dmitri A. Sergatskov, and R. V. Duncan,  
University of New Mexico

Paramagnetic susceptibility thermometers used in fundamental physics experiments are capable of measuring temperature changes with a precision of a part in  $2 \times 10^{10}$ . However, heater controllers are only able to control open-loop power dissipation to about a part in  $10^5$ .

We used an array of rf-biased Josephson junctions to precisely control the electrical power dissipation in a heater resistor mounted on a thermally isolated cryogenic platform. Theoretically, this method is capable of controlling the electrical power dissipation to better than a part in  $10^{12}$ . However, this level has not yet been demonstrated experimentally.

The experiment consists of a liquid helium cell that also functions as a high-resolution PdMn thermometer, with a heater resistor mounted on it. The cell is thermally connected to a temperature-controlled cooling stage via a weak thermal link. The heater resistor is electrically connected to the array of Josephson junctions using superconducting wire.

An rf-biased array of capacitively shunted Josephson junctions drives the voltage across the heater. The quantized voltage across the resistor is  $V_n = nf(h/2e)$ , where  $h$  is Planck's constant,  $f$  is the array biasing frequency,  $e$  is the charge of an electron, and  $n$  is the integer quantum state of the Josephson array. This results in an electrical power dissipation on the cell of  $P_n = (V_n)^2/R$ , where  $R$  is the heater resistance.

The change of the quantum state of the array changes the power dissipated in the heater, which in turn, results in the change of the cell temperature. This temperature change is compared to the expected values based on the known thermal standoff resistance of the cell from the cooling stage. We will present our initial experimental results and discuss future improvements.

This work has been funded by the Fundamental Physics Discipline of the Microgravity Science Office of NASA, and supported by a no-cost equipment loan from Sandia National Laboratories.

## **Vortex Loops at the Superfluid Lambda Transition: An Exact Theory?**

Gary A. Williams  
UCLA

A vortex-loop theory of the superfluid lambda transition has been developed over the last decade, with many results in agreement with experiments. It is a very simple theory, consisting of just three basic equations. When it was first proposed the main uncertainty in the theory was the use Flory scaling to find the fractal dimension of the random-walking vortex loops. Recent developments in high-resolution Monte Carlo simulations have now made it possible to verify the accuracy of this Flory-scaling assumption. Although the loop theory is not yet rigorously proven to be exact, the Monte Carlo results show at the least that it is an extremely good approximation. Recent loop calculations of the critical Casimir effect in helium films in the superfluid phase  $T < T_c$  will be compared with similar perturbative RG calculations in the normal phase  $T > T_c$ ; the two calculations are found to match very nicely right at  $T_c$ .

# **Response of Solid $^4\text{He}$ to External Stress: Interdigital Capacitor Solid Level Detector and Optical Interferometer**

**J. Fay, Y. Wada\*, R. Masutomi, T. Elkholy and H. Kojima**

Serin Physics Laboratory  
Rutgers University  
Piscataway, New Jersey 08854

## **abstract**

Two experiments are being conducted to observe the liquid/solid interface of  $^4\text{He}$  near 1 K. Interesting instabilities are expected to occur when the solid is non-hydrostatically stressed. (1) A compact interdigital capacitor is used as a level detector to observe solid  $^4\text{He}$  to which stresses are applied externally. The capacitor consists of 38 interlaced  $50\text{ }\mu\text{m}$  wide and  $3.8\text{ mm}$  long gold films separated by  $50\text{ }\mu\text{m}$  and deposited onto a  $5\text{ mm}$  by  $5\text{ mm}$  sapphire substrate. The capacitor is placed on one flat end wall of a cylindrical chamber ( $xx\text{ mm}$  diameter and  $xx\text{ mm}$  long). The solid is grown to a known height and a stress is applied by a tubular PZT along the cylindrical axis. The observed small change in height of the solid at the wall is linearly proportional to the applied stress. The solid height decreases under compressive stress but does not change under tensile stress. The response of the solid on compressive stress is consistent with the expected quadratic dependence on strain. (2) Interferometric techniques are being developed for observing the solid  $^4\text{He}$  surface profile. A laser light source is brought into the low temperature region via single mode optical fiber. The interference pattern is transmitted back out of the low temperature apparatus via optical fiber bundle. The solid  $^4\text{He}$  growth chamber will be equipped with two PZT's such that stress can be applied from orthogonal directions. Orthogonally applied stress is expected to induce surface instability with island-like deformation on a grid pattern. Apparatus design and progress of its construction are described.

## I. Motivation

Stress-driven instability or Grinfeld instability (GI) [1] arises from a general phenomenon of nature that a non-hydrostatically stressed solid can decrease elastic energy by rearrangement of their material particles in the vicinity of the phase boundary by processes such as melting-freezing, evaporation-sublimation and surface diffusion. GI is intimately related to phenomena of practical importance such as pattern formation in epitaxial crystal growth, surface reaction rate on pre-stressed solids, surface cracking and corrosion. Quantum crystals of  $^4\text{He}$  provide an excellent testing ground for GI effects. For investigation of interface related phenomena, the solid/liquid interface of  $^4\text{He}$  below 2 K has many advantages such as small latent heat, rapid melting and freezing and superfluid heat conduction. The ultimate goal of our research is to study the instability of solid surface morphology under externally applied stresses. Stripe and island patterns are expected to form at the interface under uniaxially applied stress and orthogonally applied stress, respectively.

The GI sets in only beyond a certain threshold stress. If the applied stress does not exceed the threshold value,  $^4\text{He}$  solid/liquid interface reacts to the stress by lowering its height. A simple interdigital capacitor solid height detector is being developed to check this effect. For observing the interfacial pattern, an optical interferometer is being built using optical fiber technology. Progress in both of these studies is presented in this report.

## II. Simplified Explanation of Grinfeld Instability

Imagine that a cubic solid body is divided up into cells as shown in Fig. 1a. In equilibrium and with no external forces applied onto the solid, the cells are all identical small cubes. When an external force is applied on the vertical faces along x-axis as shown in Figure 1c, each cell stretches along x-axis. Work is done on the solid and the elastic energy of the solid increases by an amount  $E_{\text{reg}}$ . Now, let's imagine that one cell in Figure 1c, by fluctuation, moves up onto the originally horizontal surface and makes a "bump" and a "hole" as shown in Figure 1e. If the elastic energy is to be maintained constant, the shape of the bump and the hole must keep the same shape as before moving. And for the bump to keep its shape, the same forces per unit area along the horizontal direction must be maintained

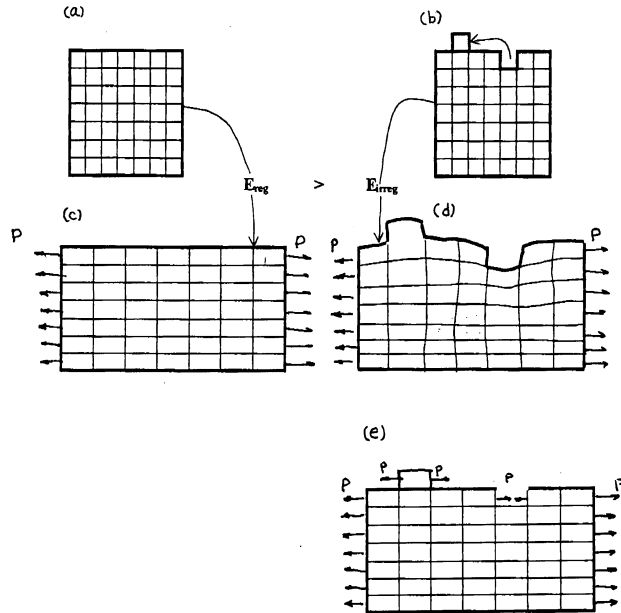


Figure 1

along the x-axis. Then, the elastic energy of the solid in Fig. 1c and Fig. 1e would be the same. Note, however, that there are no direct external horizontal forces acting neither on the bump nor on the sides of the hole. In the absence of the external forces to maintain the original shape, the bump and the hole proceed to “relax” towards a shape such as shown in Fig. 1d. The relaxation proceeds because the elastic energy is reduced in the process. The net increase of the elastic energy of the body in Fig. 1d,  $E_{\text{irreg}}$ , is less than  $E_{\text{reg}}$ . Thus the shape in Fig. 1d is more favorable than that in Fig. 1c. This is the physical origin of Grinfeld Instability.[2]

The first qualitative observations of GI are thought to be made by Bodensohn et al[3] on a rapidly cooled helium-4 crystals. More systematic measurements with externally controlled stress were carried out later by Torii and Balibar[4] who demonstrated the appearance of surface corrugation beyond a certain threshold stress.

### III. Apparatus and Preliminary Results

#### 1. Interdigital Capacitor Level Detector and Solid Growth Chamber

Consider a rectangularly shaped slab of solid  $^4\text{He}$  at its melting pressure at low temperature in equilibrium with superfluid liquid phase. Imagine that a uniaxial stress is applied on the solid. To maintain equilibrium, the chemical potentials of the solid and liquid must remain equal. Thus, the solid melts and the interface lowers by  $\Delta H$ . If solid  $^4\text{He}$  can be considered isotropic[5],  $\Delta H$  is given by[4,6]:

$$\Delta H = \frac{(1-\nu)\delta^2}{2Y^2 g(r_c - r_L)}. \quad \text{Eq. 1}$$

Here,  $\delta$  is the applied strain on the solid,  $\tilde{n}_c = 0.1908 \text{ g/cm}^3$  the density of solid,  $\tilde{n}_L = 0.1729 \text{ g/cm}^3$  the density of liquid, and  $Y = 3 \times 10^8 \text{ dyne/cm}^2$  the Young's modulus of solid,  $\nu = 1/3$  the Poisson's ratio,  $g$  the acceleration of gravity. The gravitational acceleration constant plays an important role. Note that the change in height is independent of the direction of the applied stress. So the interface height lowers under both tension and compression applied to the solid.

As an important test of understanding, we carried a preliminary study to check the expected change in height of solid  $^4\text{He}$  to which a uniaxial stress is externally applied. The apparatus for this study is shown in Figure 2. A

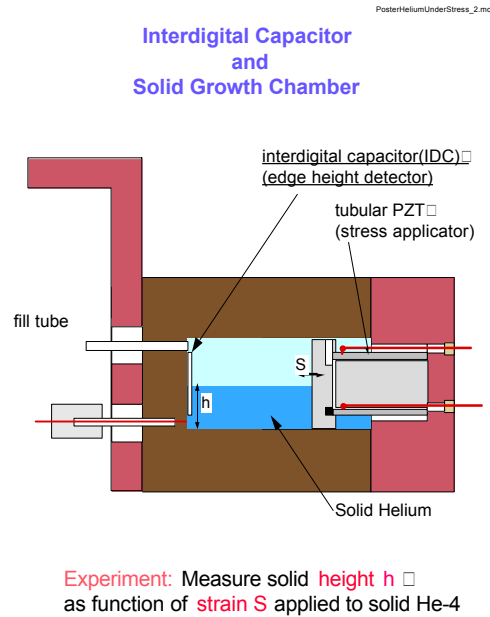


Figure 2

simple interdigital capacitor[7] for detecting the solid height is located at the end of a cylindrical chamber ( length  $L = 19.8$  mm and diameter = xx mm) in which solid  $^4\text{He}$  is grown. Note that the volume of the growth chamber is much greater than our previous one[7]. Measured changes in capacitance directly give the changes in height of the solid at the edge. The minimum detectable change in height is  $0.5 \mu\text{m}$  at present. The temperature of the chamber can be lowered to 1.2 K. Smooth growths of solid height can be observed repeatedly as helium is fed into the growth chamber from a gas handling panel at room temperature. Strains are given to the solid by moving the plunger plate attached to a tubular piezoelectric transducer(PZT)[8]. The length of the PZT is varied by the externally applied voltage between the inner and outer electrodes on it.

A typical result at  $T = 1.2$  K is shown in Figure 3. The solid was grown to about half way up the growth chamber by slowly feeding in helium. The crystal orientation relative to the growth chamber is not known. The observed change in height is shown in Figure 3 as function of the applied voltage to PZT. The positive applied voltage corresponds to the case of solid under compression. When negative voltages are applied to the solid (now under tension), observed changes are not reproducible and show little change in height.

The applied strain is given by:

$$d = \frac{d_{32}lV_{pzt}}{tL} \quad \text{Eq. 2}$$

where  $d_{32} = 0.33 \times 10^{-7}$  mm/V is the piezoelectric constant,  $l = 9.5$  mm the length of PZT,  $t = 1.0$  mm the thickness of tubular PZT,  $L = 19.8$  mm the length of cylinder (and hence solid  $^4\text{He}$ ) and  $V_{pzt}$  the applied voltage to PZT. Substituting Eq. (2) into Eq. (1) gives the expected change in height shown in Figure 3.

As expected, the data indicate lowering of height as compression is applied.

However, it cannot be claimed, particularly in the negative strain side, that the height decreases in proportion to the square of applied strain. The scatter in data is large. The scatter is in part caused by the irreproducible relaxation in height often observed after a change in applied voltage is made. Some stick-slip motion of solid at the interdigital capacitor surface could cause this irreproducibility. The small response for negative voltage indicates that solid detaches from the plunger surface. The plunger is

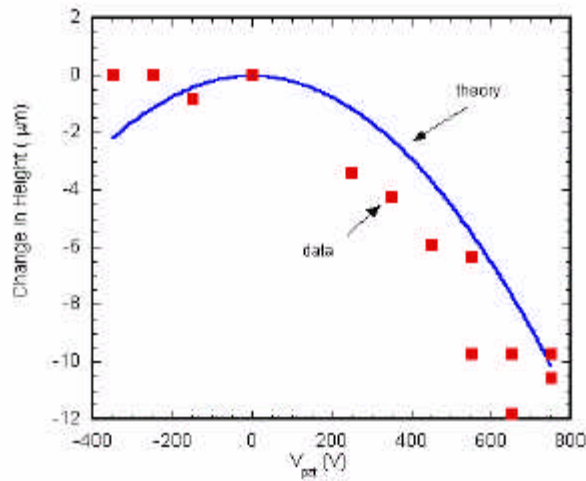


**Figure 3**

made of machined stycast 1266 which is likely to have roughness of at least  $10\text{ }\mu\text{m}$ . A glass plate has been used as a plunger surface which also produced results which depend on the direction of strain.[9] Studies are needed to find material and/or surface conditions for pulling on the surface of solid  $^4\text{He}$  without detachment.

## 2. Interferometer Apparatus

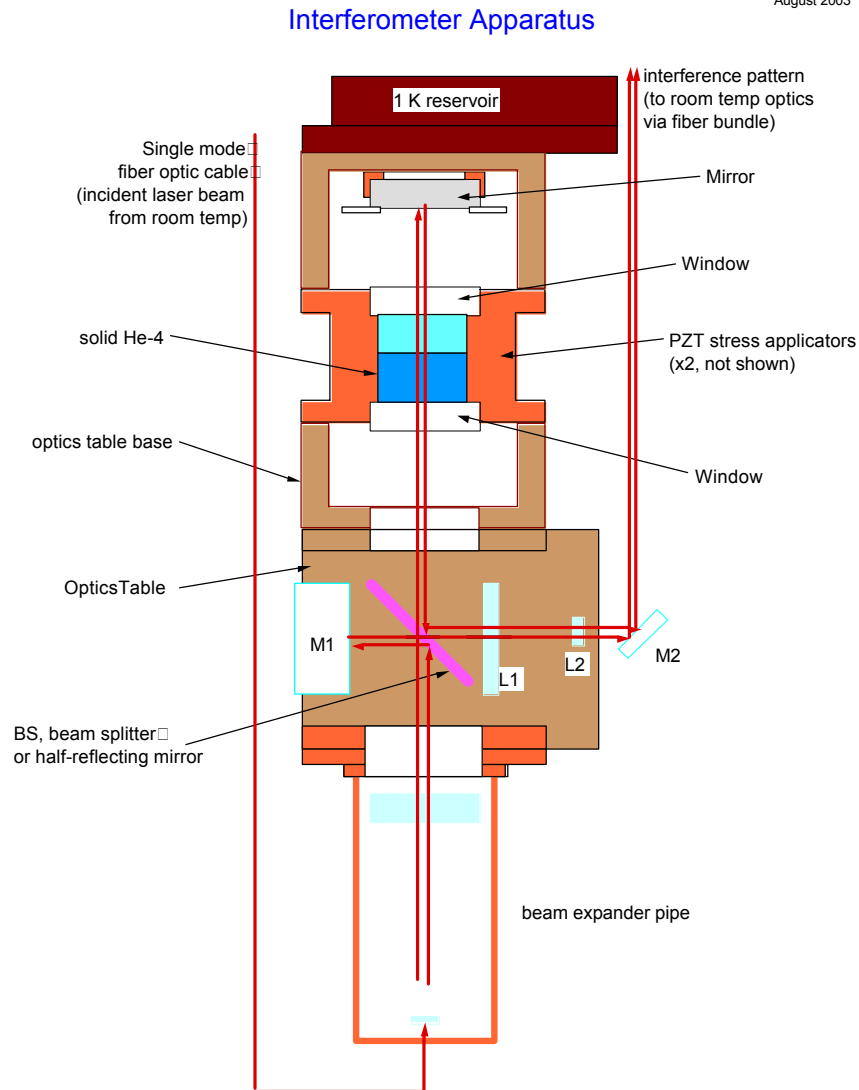


**Figure 4**

A schematic of the low temperature section of our optical apparatus for directly observing the liquid solid interface is shown in Figure 4. A single mode optical fiber brings the incident He-Ne laser beam down to the beam expander pipe. The expanded beam is split by a beam splitter plate. The reflected beam from the splitter is directed to the mirror M1. The beam reflected from M1 acts as the reference beam. The transmitted beam from the splitter moves up through the solid growth chamber (whose cross section is a  $17.8 \times 10.1\text{ mm}^2$  rectangle and the depth is xx mm) and returns back to the splitter



after reflecting from the upper mirror. The beam interferes with the reference beam and its image is transmitted up into room temperature optics via fiber bundle image conduit (diameter = 3 mm, about  $5 \times 10^4$  individual fibers).

The image transmitted through the conduit is monitored by a monochrome video camera. A photograph of the low temperature part of the optical system is shown in Figure 5. Pumping on the “1 K reservoir” pot reduces the temperature of the solid growth chamber filled with liquid helium to 1.2 K when the incident laser beam is continuously left on. The reflecting mirror M2 (see Figure 4) is visible in front of the beam splitter holder.

The interference fringe pattern may be analyzed to determine the liquid/solid interface height profile  $H(x,y)$ . The phase shift from that at some reference position between the two interfering beams may be written as:

$$\Delta f(x, y) = \frac{2p}{\lambda} [\Delta D_B(x, y) + 2(n_s - n_L)\Delta H(x, y)], \quad \text{Eq. 3}$$

where  $\Delta D_B(x,y)$  is the “background” path length shift arising from the variation in the distance between M1 and mirror in Figure 4. The difference in indices of refraction of solid and liquid is  $(n_s - n_L) = 0.034$ . For the wavelength of 630 nm for He-Ne laser, there is one fringe shift per 96  $\mu\text{m}$  of change in height  $\Delta H$ .

An example of interference pattern is shown in Figure 6. Here, the chamber is cooled to 1.3 K and filled with liquid pressurized to 5 bars. Since there is no solid, the interference pattern is set by the spatial variation in  $\Delta D_B(x,y)$ . The outline of the chamber is shown by red lines. When the pressure is increased up to the melting pressure, irreproducible initial formation of solid can be seen in the interference pattern near the end of the fill tube. Subsequent to the initial seeding of solid, interference patterns similar to that shown in Figure 7 are often observed. The interference pattern indicates formation of a flat rectangular plateau of solid surface. The spacing of the fringes within the plateau shows that there is a 30  $\mu\text{m}$  difference in height of solid along the long ends of the plateau. Presumably the solid surface height decreases towards the edges of the solid growth chamber. There should be interference pattern corresponding to these sloping surfaces. The expected pattern between the apparent edge of the plateau and the chamber boundary is not visible in the video image probably owing to lack of adequate focusing.

## IV. Conclusion

An interdigital capacitor level detector has been developed for observing changes in the height of solid  $^4\text{He}$  under uniaxial stress. Preliminary studies show compressive stresses lowers the solid height as expected, but the quadratic dependence on the magnitude of stress is not clearly demonstrated. Tensile stresses do not produce lowering of solid height contrary to expectation. Interferometric observations on solid growth patterns in a rectangular chamber have been made. Solids were formed by feeding helium into the chamber at constant temperature or by cooling at constant pressure. In the first method, a flat solid surface could be observed almost reproducibly. PZTs will be

incorporated in the near future into the chamber for applying external stresses onto the solid.

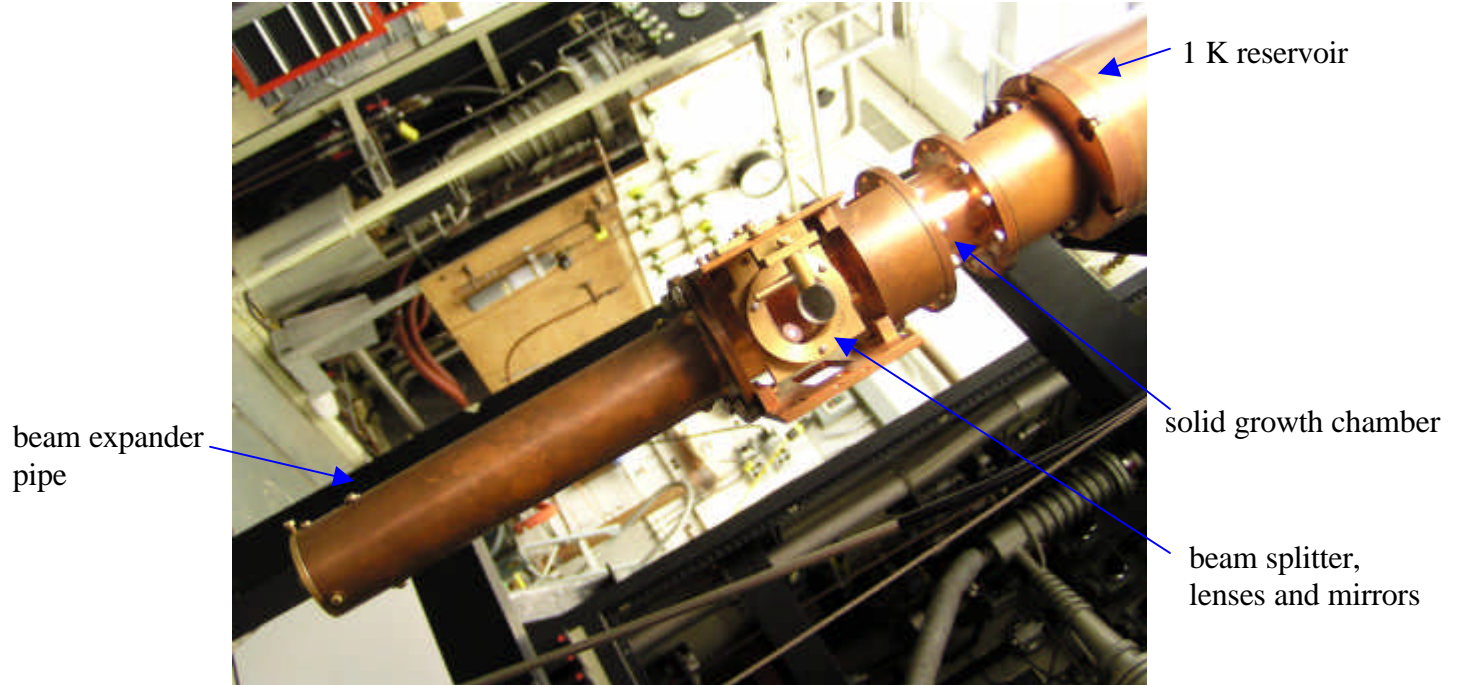


**Figure 5**

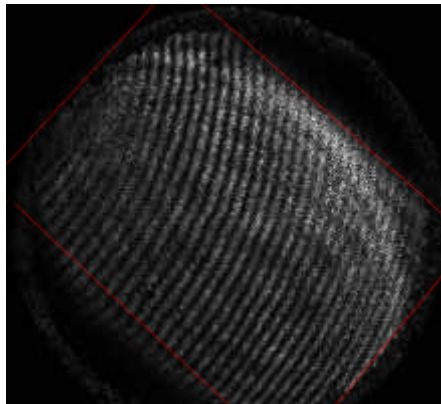


**Figure 6**

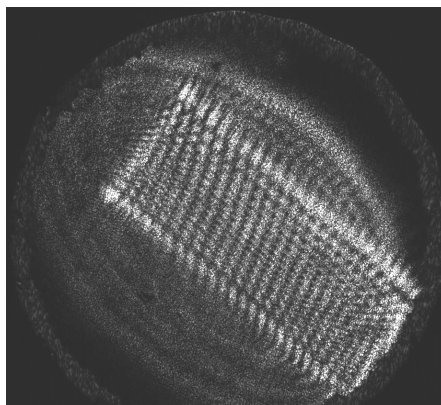


**Figure 7**

## Acknowledgement

We have enjoyed numerous discussions with Misha Grinfeld who patiently explained to us the origin of Grinfeld instability using the pictures in Fig. 1. We wish to thank Sebastien Balibar for useful discussions. This research is supported by NASA grant NAG3-2868.

## References

\* Present address: Department of Applied Physics, Tokyo Institute of Technology, Ookayama, Meguro-ku, Tokyo, Japan.

<sup>1</sup> M.A. Grinfeld, Dokl. Akad. Nauk. SSSR **290**, 1358(1986), (Sov. Phys. Dokl. **31**, 831(1987)).

<sup>2</sup> P. Nozieres, “*Solids Far From Equilibrium*,” ed. by C. Godereche, Cambridge University Press, 1991.

<sup>3</sup> J. Bodenson, K. Nicolai and P. Leiderer, Z. Phys. B **64**, 55(1986).

<sup>4</sup> R.H. Torii and S. Balibar, J. Low Temp. Phys. **89**, 391(1992).

<sup>5</sup> H.J. Maris and T.E. Huber, J. Low Temp. Phys. **48**, 99(1982).

<sup>6</sup> S. Balibar, D.O. Edwards and W.F. Saam, J. Low Temp. Phys. **82**, 119(1991).

<sup>7</sup> J. Fay, W. Jian, M. Gershenson and H. Kojima, Physica **329-333**, 413(2003).

<sup>8</sup> Pzt by Staveley, type EBL #2.

<sup>9</sup> S. Balibar, private communication.

## Measurements of the Coexistence Curve Near the $^3\text{He}$ Liquid-Gas Critical Point

Inseob Hahn

Jet Propulsion Laboratory, California Institute of Technology

April 14, 2003

The shape of the liquid-gas coexistence curve of  $^3\text{He}$  very near the critical point ( $-2 \times 10^{-6} < t < -5 \times 10^{-3}$ ) was measured using the quasi-static thermogram method. The study was performed in Earth's gravitational field using two different height calorimetry cells, both originally designed for simultaneous measurements of the isochoric heat capacity, isothermal compressibility, and PVT. The heights of two cells were 0.5 mm and 4.8 cm. The uncertainty in measuring the phase transition temperature was typically  $\pm 2 \mu\text{K}$ . The measured coexistence curve near the critical point was strongly affected by the gravitational field. Away from the critical point, the coexistence curve obtained using this technique was also consistent with the earlier work using the local density measurements of Pittman et al. The recent crossover parametric model of the equation-of-state are used to analyze the height-dependent measured coexistence curves. Data analyses have indicated that microgravity will permit measurements within two additional decades in reduced temperatures beyond the best gravity-free data obtained in Earth-bound experiments.

# **Thermal Conductivity of Liquid $^4\text{He}$ near the Superfluid Transition in Restricted Geometries**

Yuanming Liu

Jet Propulsion Laboratory, California Institute of Technology

April 14, 2003

We present measurements of the thermal conductivity near the superfluid transition of  $^4\text{He}$  in confined geometries. The confinements we have studied include: cylindrical geometries with radii  $L=0.5$  and  $1.0\ \mu\text{m}$ , and parallel plates with  $5\ \mu\text{m}$  spacing. For  $L=1.0\ \mu\text{m}$ , measurements at six pressures were conducted, whereas only SVP measurements have been done for other geometries. For the 1-D confinement in cylinders, the data are consistent with a universal scaling for all pressures at and above  $T_\lambda$ . There are indications of breakdown of scaling and universality below  $T_\lambda$ . For the 2-D confinement between parallel plates, the preliminary results indicate that the thermal conductivity is finite at the bulk superfluid transition temperature. Further analyses are needed to compare the 2-D results with those in bulk and 1-D confinement.

## **Low Temperature Microgravity Physics Facility payload for the ISS**

Don Langford and John Pensinger  
Jet Propulsion Laboratory, California Institute of Technology  
April 14, 2003

The LTMPF Payload is a 182-liter superfluid-helium dewar that will be attached to the JEM-EF facility of the International Space Station after launch in the cargo bay of the Space Shuttle. The LTMPF Payload will provide a major low-temperature research laboratory for Fundamental Physics experiments on the International Space Station. The LTMPF payload will provide instrument temperatures below superfluid helium temperatures and the ISS will provide microgravity to allow the experiments to study condensed matter and gravitational physics. Each flight will be allocated to one condensed matter instrument and one gravitation instrument.

# Paramagnetic Attraction of Impurity-Helium Solids

**E.P. Bernard, R.E. Boltnev\*, V.V. Khmelenko,  
and D.M. Lee**

*Laboratory of Atomic and Solid State Physics, Cornell University,  
Ithaca, NY, 14853 USA*

*\*Branch of Institute of Energy Problems of Chemical Physics,  
Chernogolovka, Moscow region, 142432, Russia*

## INTRODUCTION

Impurity-helium solids are formed when a mixture of impurity and helium gases enters a volume of superfluid helium.<sup>1</sup> Typical choices of impurity gas are hydrogen deuteride, deuterium, nitrogen, neon and argon, or a mixture of these. These solids consist of individual impurity atoms and molecules as well as clusters of impurity atoms and molecules covered with layers of solidified helium. The clusters have an imperfect crystalline structure and diameters ranging up to 90 angstroms, depending somewhat on the choice of impurity. Immediately following formation the clusters aggregate into loosely connected porous solids that are submerged in and completely permeated by the liquid helium.<sup>2,3</sup>

Im-He solids are extremely effective at stabilizing high concentrations of free radicals, which can be introduced by applying a high power RF discharge to the impurity gas mixture just before it strikes the superfluid helium. (Figure 1.) Average concentrations of  $10^{19}$  nitrogen atoms/cm<sup>3</sup> and  $5 \cdot 10^{18}$  deuterium atoms/cm<sup>3</sup> can be achieved this way. Figure 3 shows a typical sample formed from a mixture of atomic and molecular hydrogen and deuterium. Figure 6 shows typical sample formed from atomic and molecular nitrogen. Much of the stability of Im-He solids is attributed to their very large surface area to volume ratio and their permeation by superfluid helium. Heat resulting from a chance meeting and recombination of free radicals is quickly dissipated by the superfluid helium instead of thermally promoting the diffusion of other nearby free radicals. This temperature stability makes Im-He solids an ideal medium in which to study radicals that are involved

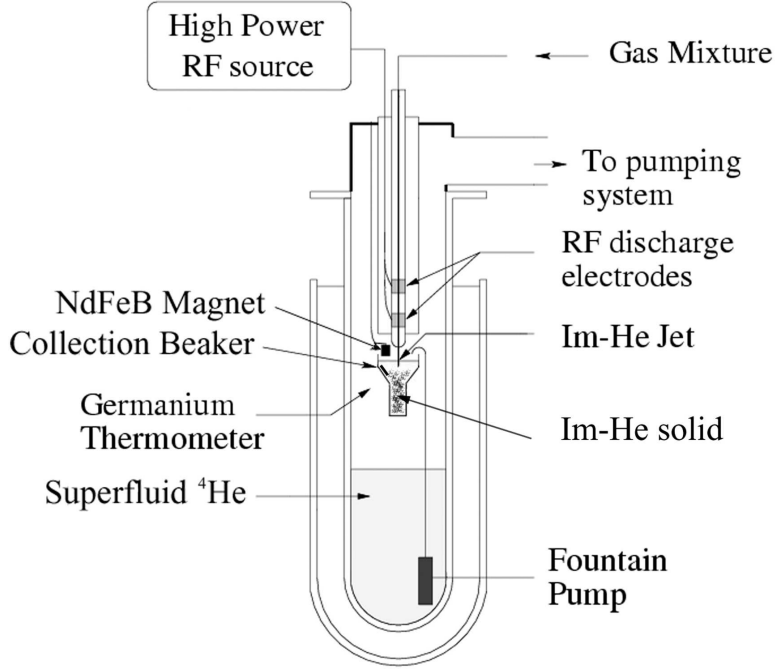


Fig. 1. Experimental apparatus for preparation and paramagnetic lifting of impurity helium solid.

in chemical reactions driven by quantum tunnelling mechanisms as opposed to conventional thermal activation.<sup>4</sup>

### Theory of Experiment

The presence of high concentrations of stabilized radicals in Im-He solids suggests that these samples will have a substantial paramagnetic attraction to regions of high magnetic field. When a permanent magnet is lowered into and withdrawn from a beaker containing an Im-He solid sample, the submerged sample will stick to the magnet if the vertical component of the paramagnetic force exceeds the gravitational force minus the buoyant force provided by the liquid helium that surrounds and permeates the sample:

$$F_{\text{mag}} = \mu n_1 V_c R(\mathbf{B}, T) \nabla \mathbf{B} \cdot \hat{\mathbf{Z}} > (\rho_c - \rho_{\text{He}}) V_c g \quad (1)$$

where  $F_{\text{mag}}$  is the vertical force exerted by the magnet on a sample,  $\mu \simeq \mu_{B g_e J}$  is the magnetic moment of each stabilized radical,  $V_c$  is the total volume occupied by the impurity clusters in a fragment,  $n_1$  is the concentration of stabilized free radicals within volume  $V_c$ ,  $\mathbf{B}$  is the field due to the



## Paramagnetic Attraction of Impurity-Helium Solids

Table 1. Characteristics of gas mixtures and impurity-helium solids.

makeup gases	respective admixture	impurities after discharge	local radical concentration, $n_l$
HD:D <sub>2</sub> :He	1:1:100	H,D,H <sub>2</sub> ,HD,D <sub>2</sub>	$n_l > 2.5 \cdot 10^{20}$
D <sub>2</sub> :He	1:20	D,D <sub>2</sub>	$2.9 \cdot 10^{18} < n_l < 2.5 \cdot 10^{20}$
N <sub>2</sub> :He	1:100	N,N <sub>2</sub>	$8.8 \cdot 10^{18} < n_l < 8.3 \cdot 10^{19}$
N <sub>2</sub> :He	1:200	N,N <sub>2</sub>	$8.8 \cdot 10^{18} < n_l < 8.3 \cdot 10^{19}$

permanent magnet,  $\hat{\mathbf{Z}}$  is the vertical unit vector,  $\rho_c$  and  $\rho_{\text{He}}$  are the densities of the impurity clusters and superfluid helium, and  $g$  is the acceleration of gravity. The field and temperature dependent Brillouin function<sup>5</sup>

$$R(\mathbf{B}, T) = \left(1 + \frac{1}{2J}\right) \coth \left[ \left(J + \frac{1}{2}\right) \left(\frac{\mu \mathbf{B} \cdot \hat{\mathbf{Z}}}{JkT}\right) \right] - \frac{1}{2J} \coth \left[ \frac{\mu \mathbf{B} \cdot \hat{\mathbf{Z}}}{2JkT} \right] \quad (2)$$

accounts for the thermalization of the magnetic moments in the sample, where  $J$  is the angular momentum quantum number of the radicals,  $k$  is Boltzmann's constant and  $T$  is the temperature. Note that  $M_z = \mu n_l R(\mathbf{B}, T)$  and  $M_z = \chi \mathbf{B} \cdot \hat{\mathbf{Z}}$  when  $\mu \mathbf{B} \cdot \hat{\mathbf{Z}}/kT \ll 1$ .

Calculating the force needed to lift samples above the surface of the superfluid helium is complicated by the fact that surface tension causes retention of a substantial amount of liquid helium within the pores of the sample. If the weight and volume of the small amount of helium solidified on the surface of the clusters is ignored, the force needed to withdraw a sample from the helium is:

$$F_{\text{mag}} = \mu n_l V_c R(\mathbf{B}, T) \nabla \mathbf{B} \cdot \hat{\mathbf{Z}} > (\rho_c + \frac{V_p}{V_c} f \rho_{\text{He}}) V_c g \quad (3)$$

where  $V_p$  is the volume of the pores in the sample fragment and  $f = 0.23$  is the degree of saturation of those pores. The porosity  $V_p/V_c$  varies greatly from sample to sample, but X-ray studies suggest that  $V_p/V_c = 150$  is typical of deuterium samples and  $V_p/V_c = 220$  is typical of nitrogen samples.<sup>2,3</sup> Measurements of the volume of liquid helium displaced by impurity-helium solids suggest an estimate of  $f = 0.23$ .<sup>6</sup>

## RESULTS

We formed samples at  $T = 1.5$  K using the four gas mixtures listed in Table 1. Deuterium hydride sample formation and nitrogen sample formation are shown in figures 2 and 5 respectively. Submerged samples within

two to three millimeters of the magnet clung to it tightly in each of the experiments. Fragments of submerged deuterium-helium solid and nitrogen-helium solid are shown clinging to the magnet in figures 4 and 7 respectively. At this distance our magnetic field gradient is about 1 T/cm and  $\mathbf{B} \sim 1/2$  T. However only the smallest fragments of the HD:D<sub>2</sub>:He sample stayed in contact with the magnet as it was lifted above the helium surface. If we make the reasonable assumption that our cluster densities are comparable to those of corresponding bulk frozen impurity gases, we find the ranges for  $n_l$  listed in Table 1.

## CONCLUSION

The experiments show that modest magnetic field gradients ( $\sim 1$  T/cm) can exert substantial forces on impurity helium solids. These techniques may be applied in future experiments to move Im-He solids from place to place or to sort them by the concentrations of radicals within their clusters. Refinements of this experiment using magnets specifically shaped to have constant field gradients could greatly improve our crude estimates of  $n_l$ . To date the formation of pure hydrogen Im-He solids has been hindered by the fact that solid hydrogen floats in superfluid helium. Our group will attempt to form a hydrogen Im-He solid using a magnetic field gradient to counteract the buoyant force and pull the sample into the liquid helium as it is formed.

## ACKNOWLEDGMENTS

This research is supported by NASA grant NAG3-2871 and is based in part on the work of R.E. Boltnev, who was supported by the North Atlantic Treaty Organization under a grant awarded in 2002. We wish to thank Vasiliy Khmelenko for his work on this project.

## REFERENCES

1. E.B. Gordon, V.V. Khmelenko, A.A. Pelmenov, E.A. Popov, and O.F. Pugachev, *Chem. Phys. Lett.* **155**, 301 (1989).
2. S.I. Kiselev, V.V. Khmelenko, D.M. Lee, V. Kiryukhin, R.E. Boltnev, E.B. Gordon, and B. Keimer, *Phys. Rev. B* **65**, 024517 (2002).
3. V.V. Khmelenko, V. Kiryukhin, E.P. Bernard, R.E. Boltnev, S.I. Kiselev, D.M. Lee, (submitted for publication to *Phys. Rev. B*).
4. S.I. Kiselev, V.V. Khmelenko and D.M. Lee, *Phys. Rev. Lett.* **89**, 175301 (2002).

### Paramagnetic Attraction of Impurity-Helium Solids

5. F. Reif, *Fundamentals of Statistical and Thermal Physics* (McGraw-Hill, New York, 1965), p. 259
6. R.E. Boltnev, E.B. Gordon, I.N. Krushinskaya, M.V. Martynenko, A.A. Pelmenev, E.A. Popov, V.V. Khmelenko, A.F. Shestakov, *Fiz. Nizk. Temp.* **23**, 753-756 (1997). [*Low Temp. Phys.* **23** 567-577 (1997).]

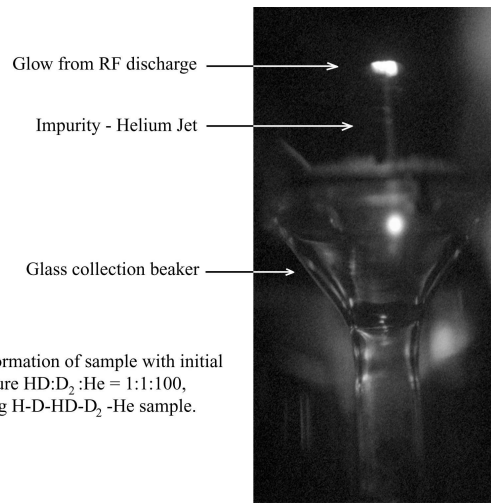


Figure 2.

Right: Formation of sample with initial gas mixture  $\text{HD:D}_2:\text{He} = 1:1:100$ , producing  $\text{H-D-HD-D}_2\text{-He}$  sample.

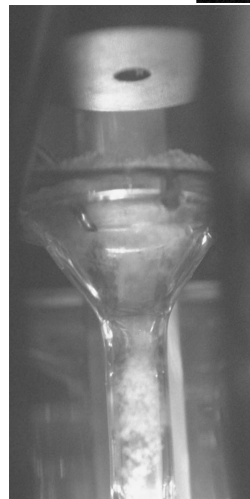


Figure 3.

Left: Stabilized  $\text{H-D-HD-D}_2\text{-He}$  sample submerged in superfluid helium following formation.

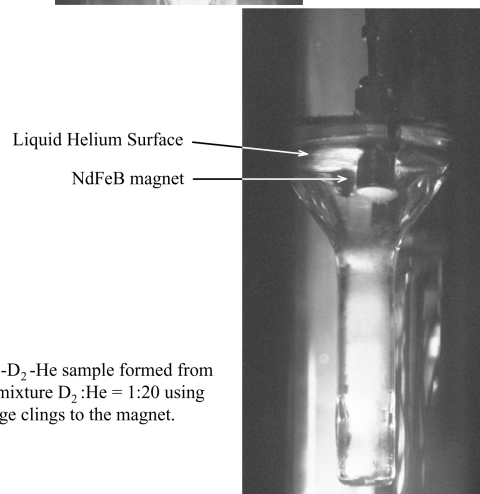
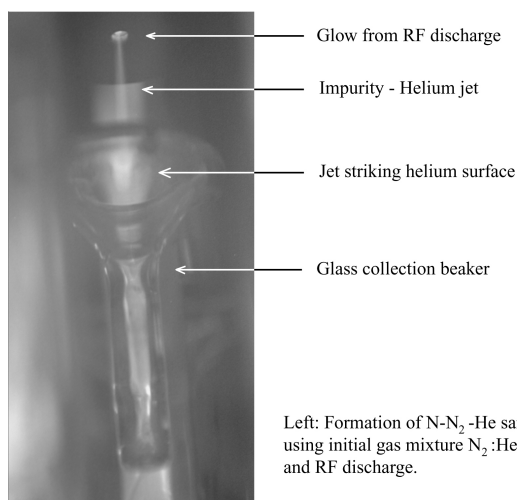


Figure 4.

Right: A  $\text{D-D}_2\text{-He}$  sample formed from initial gas mixture  $\text{D}_2:\text{He} = 1:20$  using RF discharge clings to the magnet.

## Paramagnetic Attraction of Impurity-Helium Solids

Figure 5.



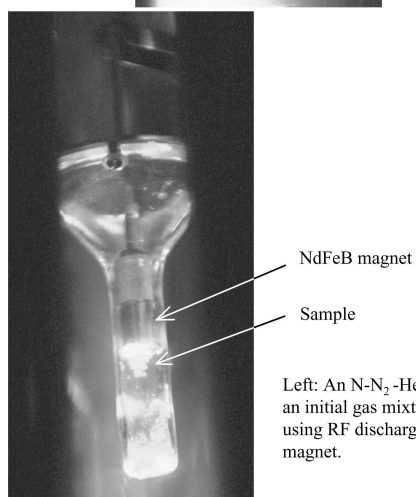
Left: Formation of N-N<sub>2</sub>-He sample using initial gas mixture N<sub>2</sub>:He = 1:200 and RF discharge.

Figure 6.

Right: Stabilized N-N<sub>2</sub>-He sample submerged in superfluid helium following formation.



Figure 7.



Left: An N-N<sub>2</sub>-He sample formed from an initial gas mixture N<sub>2</sub>:He = 1:200 using RF discharge is lifted by the magnet.

## **The Low Temperature Microgravity Physics Facility: Progress And Status**

Melora Larson, John Pensinger, Feng-Chuan Liu, and G. John Dick  
Jet Propulsion Laboratory, California Institute of Technology  
April 14, 2003

The Jet Propulsion Laboratory (JPL) is developing the Low Temperature Microgravity Physics Facility (LTMPF). The LTMPF is a multiple user and multiple flight facility that will provide a long duration low temperature environment for performing state of the art experiments at the International Space Station (ISS). During each mission, two distinct primary experiments will be accommodated. Secondary experiments utilizing the hardware built for the primary experiments will also be accommodated during each mission. Over the past year, much progress has occurred on the LTMPF as the flight hardware has started to be built. Also, many changes have occurred. Last summer, the initial flight of the LTMPF was delayed until early 2008 by a 2-year slip in the delivery of the Japanese Experiment Module (KIBO) Exposed Facility of the ISS, where the LTMPF will be attached when it flies. Finally, the experiments that will fly as part of the first mission have been changed so that one Gravitational and Relativistic experiment and one Low Temperature Condensed Matter experiment will fly on each flight of the LTMPF. Therefore, the experiments that will fly on the initial mission of the LTMPF will be DYNAMX and the Superconducting Microwave Oscillator Experiment (SUMO).

## Coalescence of Liquid Drops

Weijun Yao  
Brown University

When two liquid drops come into contact, a neck forms between them and grows rapidly. We are interested in the very early stage of the coalescence process, which can be characterized by the time dependence of the radius of the neck. The functional dependence of the size of the neck on time depends on the properties of the liquid. Experimentally, we are investigating a liquid in Stokes flow regime where the viscosity provides the principal retarding force to the surface tension. Recently, it has been predicted that the neck radius should change as  $t \ln|t|$  in this regime.

Theoretically, we have studied the situation when the velocity at each point on the surface is proportional to the local curvature and directed normal to the surface. This is the case that should be applicable to superfluid helium at low temperature when the mean free path of the thermal excitations are comparable to the size of liquid drops. For this system, the radius of the neck is found to be proportional to  $t^{1/3}$ . We are able to find a simple expression for the shape of the interface in the vicinity of the neck.

## **A macroscopic realization of the weak interaction**

Arito Nishimori  
Stanford University

A.J.Leggett suggested in 1977 that a permanent electric dipole moment due to the parity-nonconserving electron-nucleon interaction, even though it is extremely small, could be measured in the superfluid  $^3\text{He-B}$  because the moment should be proportional to the size of the sample in this system. If this moment is observed, it will be the first example of a macroscopic realization of the weak interaction. In our planned experiments, a high electric field of up to 6 kV/cm is applied between two parallel electrodes in the  $^3\text{He}$  sample. We expect to observe the NMR frequency of the lowest-lying spin-wave mode trapped by the liquid crystal-like texture of the B phase rotation axis in our geometry. The interaction of the electric field and the macroscopic permanent electric dipole moment, which is oriented along the rotation axis, will cause a small change in the texture and hence a small increase in the frequency of the spin wave mode. Besides the basic ideas, we present the purpose and the design of our first cell that is under construction.



## **Thermally Driven Josephson Effect**

Konstantin Penanen and Talso Chui  
Jet Propulsion Laboratory, California Institute of Technology  
April 14, 2003

Break-throughs in the study of superfluid  $^3\text{He}$  weak links and recent demonstration of Josephson effect in  $^4\text{He}$  are a result of significant advances in ultra-sensitive transducer and nanofabrication technology. However, further progress in the performance of superfluid weak links and quantum rotation interferometry devices depends, in part, on reducing the mechanical noise and increasing the effective duty cycle of such devices. In existing devices, the DC Josephson effect is driven by chemical potential difference produced by a pressure applied across the weak link. We propose a novel drive technique, where the chemical potential is due to a controlled temperature difference. This technique promises to eliminate mechanical shock associated with the switch of the direction of applied pressure and to achieve 100% duty cycle. The thermally driven Josephson effect may also answer outstanding questions about dissipation in superfluid weak links.

## **Progress in Developing a New Field-Theoretical Crossover Equation-of-State**

Joseph Rudnick

Department of Physics and Astronomy, University of California at Los Angeles,  
Los Angeles, CA 90095-1547

and

M. Barmatz and Fang Zhong

Jet Propulsion Laboratory, California Institute of Technology, Pasadena, CA 91109

April 14, 2003

A new field-theoretical crossover equation-of-state model is being developed. This model of a liquid-gas critical point provides a bridge between the asymptotic equation-of-state behavior close to the transition, obtained by the Guida and Zinn-Justin parametric model [J. Phys. A: Math. Gen. 31, 8103 (1998)], and the expected mean field behavior farther away. The crossover is based on the beta function for the renormalized fourth-order coupling constant and incorporates the correct crossover exponents and critical amplitude ratios in both regimes. A crossover model is now being developed that is consistent with predictions along the critical isochore and along the coexistence curve of the minimal subtraction renormalization approach developed by Dohm and co-workers and recently applied to the  $O(1)$  universality class [Phys. Rev. E, 67, 021106 (2003)]. Experimental measurements of the heat capacity at constant volume, isothermal susceptibility, and coexistence curve near the  $^3\text{He}$  critical point are being compared to the predictions of this model. The results of these comparisons will be presented.

# Bose Condensation at $^4\text{He}$ Interfaces

E. W. Draeger

*Lawrence Livermore National Laboratory, 7000 East Avenue, L-415, Livermore, CA 94550*

D. M. Ceperley

*Department of Physics and National Center for Supercomputing Applications,  
University of Illinois Urbana-Champaign, IL 61801*

Path Integral Monte Carlo was used to calculate the Bose-Einstein condensate fraction at the surface of a helium film at  $T = 0.77\text{ K}$ , as a function of density[1]. Moving from the center of the slab to the surface, the condensate fraction was found to initially increase with decreasing density to a maximum value of 0.9, before decreasing. Long wavelength density correlations were observed in the static structure factor at the surface of the slab. A surface dispersion relation was calculated from imaginary-time density-density correlations.

Similar calculations of the superfluid density throughout  $^4\text{He}$  droplets doped with linear impurities  $(\text{HCN})_n$  are presented[2]. After deriving a local estimator for the superfluid density distribution, we find a decreased superfluid response in the first solvation layer. This effective normal fluid exhibits temperature dependence similar to that of a two-dimensional helium system.

## I. BOSE CONDENSATION AT A FREE $^4\text{He}$ SURFACE

It has been suggested[9] that the condensate fraction in the low density region near a  $^4\text{He}$  surface is significantly larger than the value in bulk helium of 0.1[7]. Variational Monte Carlo (VMC) simulations by Lewart and Pandharipande[8] of small ( $N = 70$ )  $^4\text{He}$  droplets using a Jastrow one-body (JOB) trial wave function give evidence for a condensate fraction which approaches unity as the density goes to zero in the helium surface. However, subsequent calculations by Galli and Reatto[10] have shown that the condensate fraction throughout a helium surface computed using VMC is highly sensitive to the choice of trial wave function. They found that calculations performed using a shadow wave function with a glue term (G-SWF) have enhanced density-density correlations at long wavelengths[11], and a maximum condensate fraction of only 0.5. Significant ripplon excitations are expected to reduce the condensate fraction at the surface, as fewer atoms are able to occupy the zero-momentum state. Quantum evaporation experiments[6] can be interpreted as providing evidence of an enhanced condensate fraction.

To avoid the problem of trial function bias and to include finite-temperature effects, we have used Path Integral Monte Carlo (PIMC) to calculate the density-density correlation functions and condensate fraction at the surface of liquid  $^4\text{He}$ . We have also used imaginary-time correlation functions to calculate the dispersion relation of surface excitations in a free helium surface, and find good agreement with experimental thin film measurements.

## II. PIMC SIMULATION

Our simulation system consisted of  $^4\text{He}$  atoms, interacting pair-wise with a very accurate potential[12]. Peri-

odic boundary conditions were used with a box size and initial conditions chosen to favor a double-sided film oriented perpendicular to the  $z$ -axis. To maintain a stable film and minimize finite size effects, we added an external potential determined from the long-ranged part of the interaction potential and the missing atoms from the other side of the slab, so that atoms on each of the two surfaces saw a potential as if they were at the surface of a semi-infinite slab[13].

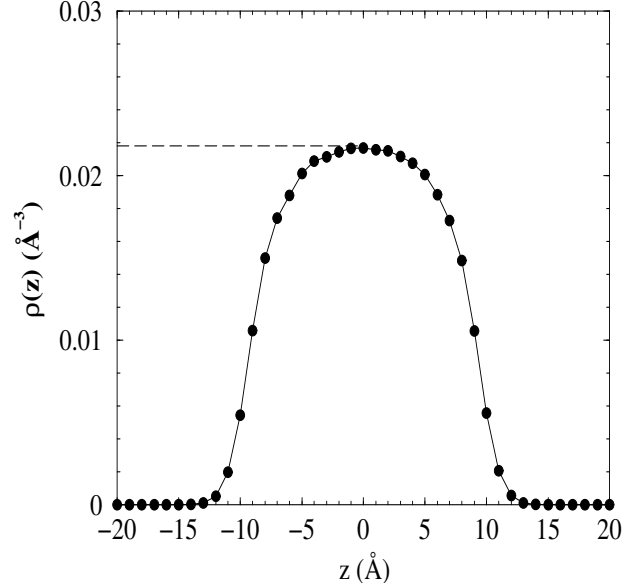


FIG. 1: PIMC density distribution, for an  $N = 432$ ,  $T = 0.77\text{ K}$  semi-infinite  $^4\text{He}$  slab. The  $N = 216$  results are indistinguishable. The dashed line shows the effective helium density felt by atoms at  $z > 0$ .

Most of the calculations were performed with  $T = 0.77\text{ K}$ , with an imaginary time step of  $\tau = 1/20\text{ K}^{-1}$ . We performed simulations of helium slabs containing  $N =$

216 and  $N = 432$  atoms, with dimensions  $24 \times 24 \times 17 \text{ \AA}$  and  $34 \times 34 \times 17 \text{ \AA}$ , respectively. Lower temperature calculations were also done to determine the temperature dependence.

### III. THE STATIC STRUCTURE FACTOR

In order to determine the extent to which ripples are present in a free helium surface, we estimated density-density correlations at the surface[11] with the static structure factor defined as:

$$S(k_{||}; z, z') = \langle \rho_{k_{||}}(z) \rho_{k_{||}}(z') \rangle \quad (3.1)$$

where  $\rho_k(z) \equiv \frac{1}{\sqrt{N(z)}} \sum_i e^{i\mathbf{k} \cdot \mathbf{r}_i} \delta(z_i - z)$ ,  $N(z)$  is the num-

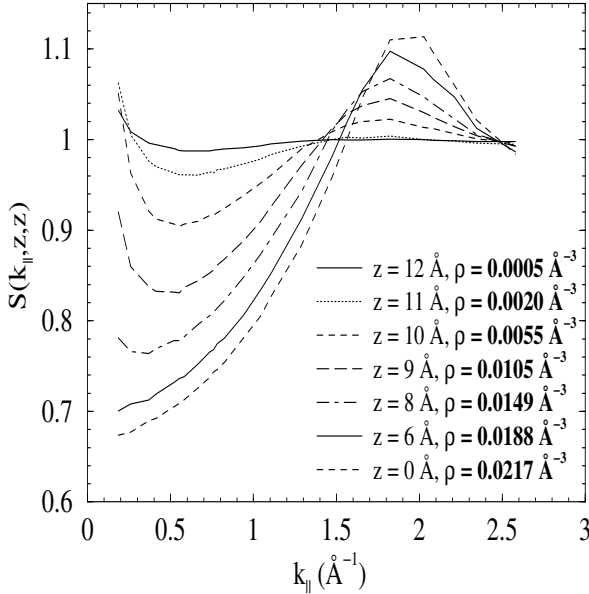


FIG. 2:  $S(k_{||}, z, z)$  vs.  $k_{||}$  throughout the surface region in an  $N = 432$   $^4\text{He}$  slab, calculated with PIMC, for  $T = 0.77$  K.

ber of particles in the bin at position  $z$  and  $k_{||}$  is the wave vector parallel to the surface. This measures the correlation between density fluctuations at vertical positions  $z$  and  $z'$ .

Fig. 2 shows  $S(k_{||}, z, z)$  curves as a function of density  $\rho(z)$ . Each curve is the average of both sides of the slab of eight identical simulations (a total of  $7 \times 10^5$  Monte Carlo passes). At densities of  $\rho(z) = 0.015 \text{ \AA}^{-3}$  and below there is a small enhancement of long-wavelength density-density correlations at  $k_{||} = 2\pi/L = 0.18 \text{ \AA}^{-1}$ , which is evidence for ripples. However, the curves are closer to the VMC calculations of Galli and Reatto which used a JOB trial wave function than those which used the G-SWF form. This does not imply that the JOB trial wave function is well-suited to representing an inhomogeneous helium system such as a helium slab, but

rather the degree to which the G-SWF significantly overestimates the effect of ripples in a free helium surface. Calculations at  $N = 216$  and  $T = 0.77$  K agree with the results of Fig. 2 within statistical error, indicating that finite-size effects are negligible. At  $T = 0.38$  K, we find a measurable decrease in the long-wavelength correlations. Further studies are needed to establish the temperature dependence.

### IV. THE EXCITATION SPECTRUM

The excitation spectrum can be estimated with path integrals using imaginary-time correlation functions[14]. The dynamic structure factor is related to the imaginary-time density-density correlation function by:

$$F(\mathbf{k}, t) = \int_{-\infty}^{\infty} d\omega e^{-t\omega} S(\mathbf{k}, \omega) \quad (4.1)$$

$$= \frac{1}{N} \langle \rho_{\mathbf{k}}(t) \rho_{\mathbf{k}}(0) \rangle. \quad (4.2)$$

To select out the excitations at the free surface, we want to calculate the imaginary-time correlation function of propagating surface modes. W. F. Saam[15] proposed that the lowest quantized hydrodynamic mode (capillary wave) at a free helium surface will have the form

$$\phi_{k0}(\mathbf{r}, t) = \phi_{k0}(z) e^{i\mathbf{k} \cdot \mathbf{r}_{||}} e^{-i\omega_{k0}t} \quad (4.3)$$

where

$$\phi_{k0}(z) \propto e^{-\kappa(k)z} \quad (4.4)$$

and the decay constant  $\kappa(k)$  is defined as

$$\kappa(k) = -b_k + (k^2 + b_k^2)^{1/2} \quad (4.5)$$

$$b_k \equiv \frac{\sigma_0 k^2}{2\rho_0 s^2} \quad (4.6)$$

where  $\sigma_0$  is the zero-temperature surface tension,  $\rho_0$  is the bulk density, and  $s$  is the zero-temperature sound velocity. To calculate the dispersion relations for excitations of this form, we use  $\tilde{\rho}_{\mathbf{k}}$  in Eq. (4.2), defined as

$$\tilde{\rho}_{\mathbf{k}} = \sum_i e^{i\mathbf{k}_{||} \cdot \mathbf{r}_{i||}} \phi_k(z_i) \quad (4.7)$$

where

$$\phi_k(z) = e^{-\kappa(k)(z-z_c)} \quad (4.8)$$

and  $\kappa(k)$  is defined by Eq. (4.5). We defined  $z_c$  as the point in the surface at which the average density was equal to 10% of the bulk density.

Extracting the dynamic structure factor by inverting Eq. (4.1) is ill-conditioned in the presence of statistical noise. It has been shown[16] that a maximum entropy method greatly increases the numerical stability. In the maximum entropy method,  $S(k, \omega)$  is calculated by minimizing the function

$$\mathcal{F}(S, \alpha) = \frac{e^{-(1/2)Q(S)}}{Z_Q} \times \frac{e^{\alpha \zeta(S)}}{Z_{\zeta}} \quad (4.9)$$

where  $Q(S)$  is the "likelihood" of the PIMC data given an  $S$  and  $\zeta(S)$  is the entropy of a given  $S(k, \omega)$  defined with respect to some default model, with  $\alpha$  an adjustable parameter (also optimized).

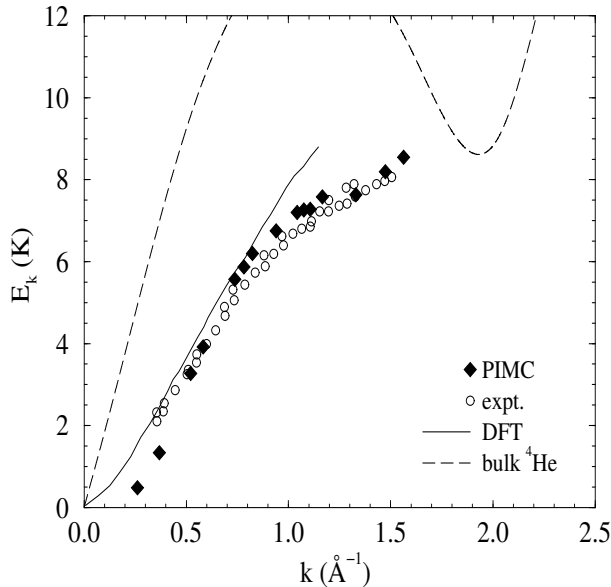


FIG. 3: Dispersion relation of free surface excitations. The results calculated from PIMC and maximum-entropy inversion (filled diamonds) for an  $N = 216$ ,  $T = 0.77$  K  $^4\text{He}$  slab are compared with the experimental thin film data (open circles) of Lauter *et al.* and the DFT results (solid line) of Lastrì *et al.* Also shown is the dispersion relation of bulk  $^4\text{He}$  at SVP (dashed line).

The dispersion energy for a given value of  $k$  can be determined from the position of the maximum value of  $S(k, \omega)$ . Boninsegni and Ceperley[17] found that the position of the main  $S(k, \omega)$  peaks for liquid helium agree quite well with experiment, despite significant broadening of the excitation spectrum caused by the maximum entropy procedure. The dispersion energy of the surface excitations as estimated using this procedure are shown in Fig. 3. The two lowest data points, at  $k < 0.5$  Å $^{-1}$ , had significant fitting error and are only qualitatively reliable. Otherwise, we see excellent agreement with the experimental thin film data of [3], including the curvature of the ripplon branch toward the roton minimum, proposed as evidence for roton-ripplon hybridization[18, 19].

## V. THE BOSE-EINSTEIN CONDENSATE FRACTION

We define the condensate fraction in the slab geometry by the fraction of atoms at a given value of  $z$  having precisely  $k_{\parallel} = 0$ . (Because  $[k_{\parallel}, z] = 0$ , we can measure the momentum parallel to the surface simultaneously with the  $z$ -position.) The momentum distribution at a dis-

tance  $z_0$  from the center of the slab is given by

$$n_{\mathbf{k}_{\parallel}}(z_0) = \frac{1}{(2\pi)^2} \int d\mathbf{r}_{\parallel} e^{-i\mathbf{k}_{\parallel} \cdot \mathbf{r}_{\parallel}} n(\mathbf{r}_{\parallel}; z_0) \quad (5.1)$$

where the off-diagonal single particle density matrix is:

$$n(\mathbf{r}; z) = \frac{1}{\rho(z)Z} \int d\mathbf{r}_1 \cdots d\mathbf{r}_N \rho(\mathbf{r}_1, \mathbf{r}_2, \cdots \mathbf{r}_N, \mathbf{r}_1 + \mathbf{r}, \mathbf{r}_2, \cdots \mathbf{r}_N; \beta). \quad (5.2)$$

and  $\rho$  is the many-body density matrix,  $Z = \text{Tr}(\rho)$  is the partition function, and  $r_{\parallel} \equiv |\mathbf{r}_{\parallel} - \mathbf{r}'_{\parallel}|$ . This function can be calculated from PIMC[20] by performing simulations with a single open path. We fix the endpoints of the open path at  $z = z_0$ , and calculate the distribution of end-to-end distance  $n(r_{\parallel}; z_0)$ . The condensate fraction at a given point in the surface is:

$$n_0(z_0) = \frac{n(r_{\parallel} \rightarrow \infty; z_0)}{n(r_{\parallel} \rightarrow 0; z_0)}. \quad (5.3)$$

Using PIMC, we calculated  $n(r_{\parallel}, z)$  throughout the slab. Nonlinear least-squares fitting was used in the region of  $r_{\parallel} < 1.5$  Å to get an estimate of  $n(r_{\parallel} = 0, z)$ , and  $n(r_{\parallel} \rightarrow \infty, z)$  was calculated by averaging over the region at large  $r_{\parallel}$  where  $n(r_{\parallel}, z)$  is flat. At the lowest densities, it is not clear whether the  $n(r)$ 's have reached their asymptotic limit within the finite simulation box. Thus, for those densities, (for  $N = 216$  below  $\rho(z) = 0.001$  Å $^{-3}$ ) our results are upper bounds to the condensate fraction.

The condensate fraction  $n_0(z)$  is plotted as a function of average density  $\rho(z)$  in Fig. 5, for both  $N = 216$  and  $N = 432$  helium slabs. As one moves through the surface, the condensate fraction initially increases with decreasing density, due to the decreased zero-point motion from helium-helium interactions, reaching a maximum value of  $0.93(3)$  at  $\rho(z) = 0.002$  Å $^{-3}$ . As the average density decreases below this point, the condensate fraction begins to decrease, further evidence for correlated density fluctuations due to ripplons at the surface. This is in qualitative agreement with the G-SWF VMC calculations of Galli and Reatto. However, the G-SWF trial wave function significantly overestimates the degree to which ripplons are present in the surface.

Our results support the model of a free helium surface with ripplons, in which the condensate fraction reaches a maximum at an intermediate density in the liquid-vacuum interface, before decreasing at lower densities. Experimental probes of the surface will indeed see an enhanced condensate fraction as proposed by Griffin and Stringari[9].

## VI. LOCAL SUPERFLUIDITY DENSITY ESTIMATOR

In this section, a microscopic Path Integral Monte Carlo (PIMC) estimator of the local contribution to the

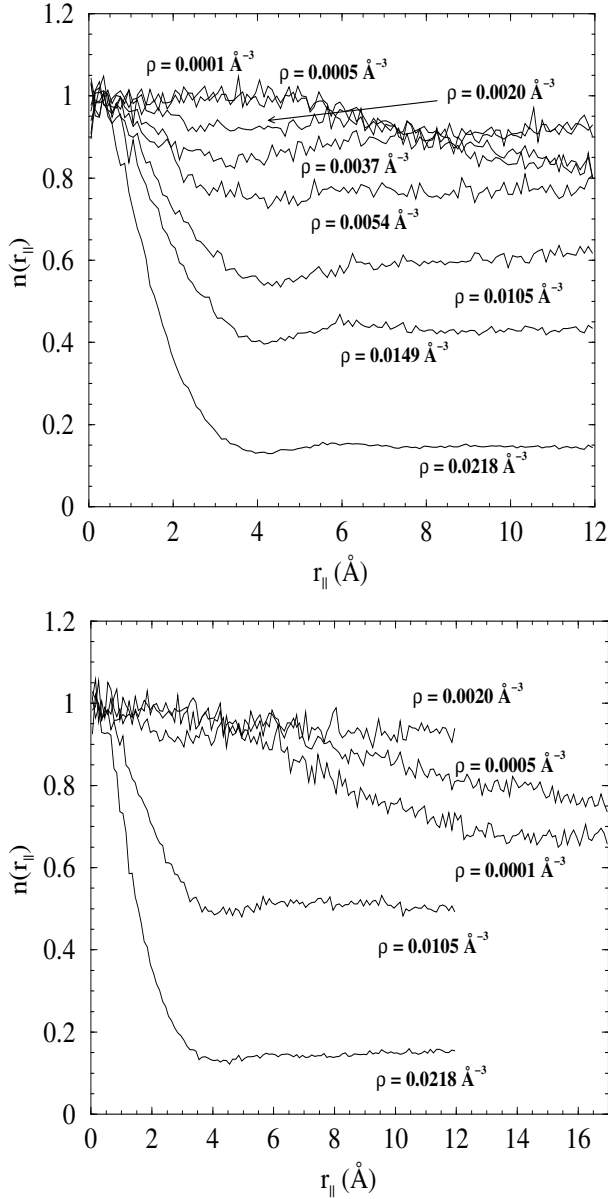


FIG. 4:  $n(r_{||}, z)$  vs  $r_{||}$ , throughout the surface region of  $N = 216$  (top) and  $N = 432$  (bottom)  $^4\text{He}$  slabs at  $T = 0.77$  K, calculated with PIMC. The slab dimensions were  $24 \times 24 \times 17$  Å and  $34 \times 34 \times 17$  Å respectively. Density labels correspond to  $z = 0, 8, 9, 10, 10.5, 11, 12, 13$  Å for  $N = 216$ , and  $z = 0, 9, 11, 12, 13$  Å for  $N = 432$ .

total superfluid response is presented. The superfluid density can be defined in terms of the response of the system to an imposed rotation. In imaginary-time path integrals, it is manifested by particle exchange over length scales equal to the system size. Although superfluid response (like conductivity) is not itself a local property, it is possible to calculate a local contribution to the total response. In PIMC, the total superfluid response along the axis of rotation  $\hat{n}$  is proportional to the square of

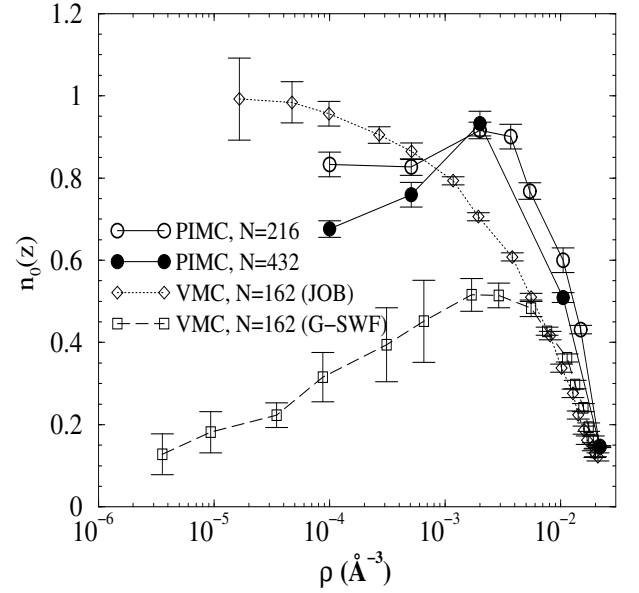


FIG. 5: Condensate fraction vs. density throughout the surface region of a  $T = 0.77$  K  $^4\text{He}$  slab. Also shown are the VMC calculations of Galli and Reatto.

total projected area of the imaginary-time paths[24]:

$$\frac{\rho_s}{\rho} \Big|_{\hat{n}} = \frac{2m \langle A_{\hat{n}}^2 \rangle}{\beta \lambda I_c}, \quad (6.1)$$

where  $\lambda = \hbar^2/2m$ ,  $\beta = 1/k_B T$  and  $I_c$  is the classical moment of inertia. To define a local superfluid density we write:

$$\begin{aligned} \rho_s(\mathbf{r})|_{\hat{n}} &= \frac{2mN}{\beta \lambda I_c} \langle \int d\mathbf{r}' A_{\hat{n}}(\mathbf{r}) A_{\hat{n}}(\mathbf{r}') \rangle \\ &= \frac{2mN}{\beta \lambda I_c} \langle A_{\hat{n}}(\mathbf{r}) A_{\hat{n}} \rangle, \end{aligned} \quad (6.2)$$

where  $\mathbf{A}(\mathbf{r})$ , related to the local angular momentum operator, is defined as

$$\mathbf{A}(\mathbf{r}) \equiv \frac{1}{2} \sum_{i,k} (\mathbf{r}_{i,k} \times \mathbf{r}_{i,k+1}) \delta(\mathbf{r} - \mathbf{r}_{i,k}) \quad (6.3)$$

and  $A_{\hat{n}}$  is the  $\hat{n}$ -component of the total area of all the particles. Since  $\mathbf{A}\mathbf{r}$  integrates to the total area, the local superfluid response exactly integrates to the total response.

Two types of contributions to the local superfluid density can be distinguished based on the connectivity of the instantaneous paths: contributions of particles on the same chain, which on the average must be positive, and contributions of particles on different exchange cycles. By reversing the order of one exchange cycle the contribution from different cycles will change sign; if the cycles are spatially separated, the magnitude of the contribution will be unaffected, so that their contribution is much smaller. They will however increase the statistical

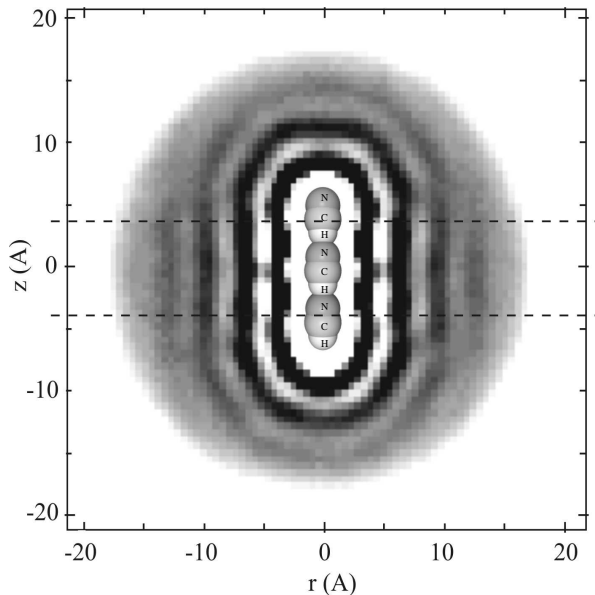


FIG. 6: Average number density of an  $N = 500$   ${}^4\text{He}-(\text{HCN})_3$  droplet at  $T = 0.38$  K. The grey scale saturates at  $\rho = 0.03 \text{ \AA}^{-3}$  (black). The dashed lines define the cylindrically-symmetric region used for averaging superfluid density.

noise of the superfluid density. Numerically we find that the same cycle contribution accounts for roughly 80% of the total superfluid density in the systems presented in this paper.

The local superfluid density estimator used by Kwon and Whaley[23] defined the effective normal fluid induced by the anisotropic molecule-helium interaction potential in terms of the average number density distribution of paths in exchange cycles of fewer than six atoms. Although qualitatively interesting, this estimator is not the superfluid response to an imposed rotation, as there is no direct relation between the number of atoms in a permutation cycle and its area.

## VII. SUPERFLUIDITY OF HELIUM DROPLETS WITH MOLECULAR IMPURITIES

Molecules confined in helium nanodroplets have been shown to exhibit excitation spectra with clearly resolved rotational fine structure consistent with that of a free rotor, though with an increased moment of inertia. Grebenov *et al.*[21] have shown that only a few layers of  ${}^4\text{He}$  coating the molecule are required to decouple the impurity from the droplet and achieve free rotation. Callegari *et al.*[22] have suggested that the increased moment of inertia is due to the hydrodynamic response of the impurity rotating through the anisotropic helium density immediately surrounding the molecule. Kwon and Whaley[23] have proposed a model in which a microscopic normal fluid is induced in the first solvation layer by the anisotropy of the molecule-helium interaction.

In order to test our estimator, PIMC simulations were performed on  $N = 128$  and  $N = 500$   ${}^4\text{He}$  droplets doped with  $(\text{HCN})_3$  isomers. Nauta and Miller[32] found that HCN molecules in helium droplets self-assemble into linear chains spaced roughly  $4.4 \text{ \AA}$  apart. The HCN molecules in our simulations were fixed along the  $z$ -axis with this spacing. An imaginary time-step of  $1/20 \text{ K}^{-1}$  was used. With cylindrical symmetry and precise experimental data over a range of isomer lengths, this system is well-suited for studying superfluidity at a molecular interface.

The number density of a doped helium droplet at  $T = 0.38$  K is shown in Fig. 6. The two-dimensional areal density of the first solvation layer was  $0.12 \text{ \AA}^{-2}$ , which is still in the liquid phase for thin  ${}^4\text{He}$  films at these temperatures [25]. Even if the density were large enough to be solid in a 2D film, the curved geometry of the film around the HCN molecule could frustrate crystalline order, keeping the first solvation layer in a dense liquid state.

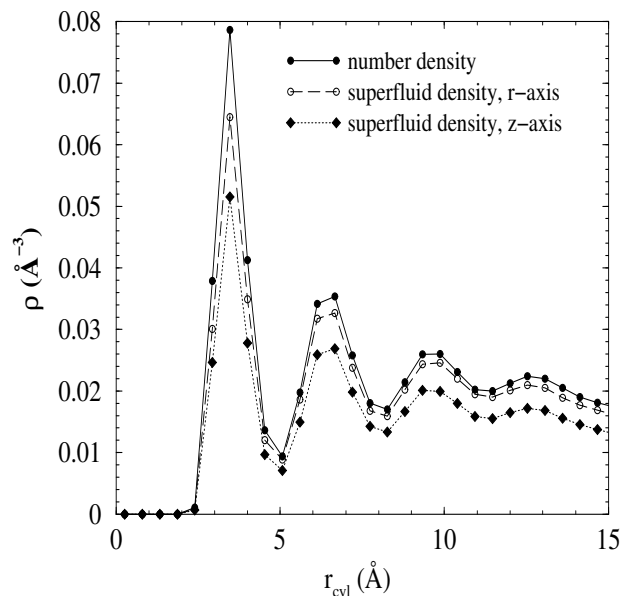


FIG. 7: Superfluid and number density distributions, averaged over the cylindrically-symmetric region of an  $N = 500$   ${}^4\text{He}-(\text{HCN})_3$  droplet at  $T = 0.38$  K.

We define the change in the moment of inertia due to the helium as the contribution due to the normal fraction in the first layer rotating rigidly with the impurity:

$$\Delta I = \int_{v(\xi)} d\mathbf{r} m_4 r_{\perp}^2 (\rho(\mathbf{r}) - \rho_s(\mathbf{r})) \quad (7.1)$$

where  $v(\xi)$  is the volume of helium a distance  $\xi$  away from the surface of the molecule,  $r_{\perp}$  is the radial distance from the axis of rotation in cylindrical coordinates. Both the estimated statistical error and the uncertainty due to the cut-off were on the order of 10%. The moment of inertia due to the effective normal fluid in the first solvation layer calculated using our PIMC local superfluid

density estimator is in reasonable agreement with the experimental value of  $\Delta I = 1240 \text{ amu } \text{\AA}^2$  [31], within error bars. We also find that  $\Delta I$  is effectively independent of temperature below

$T = 1.0 \text{ K}$ . This is because the dominant contribution to the moment of inertia comes from the induced normal fluid at the ends of the isomer, which is almost completely due to anisotropy in the molecular potential.

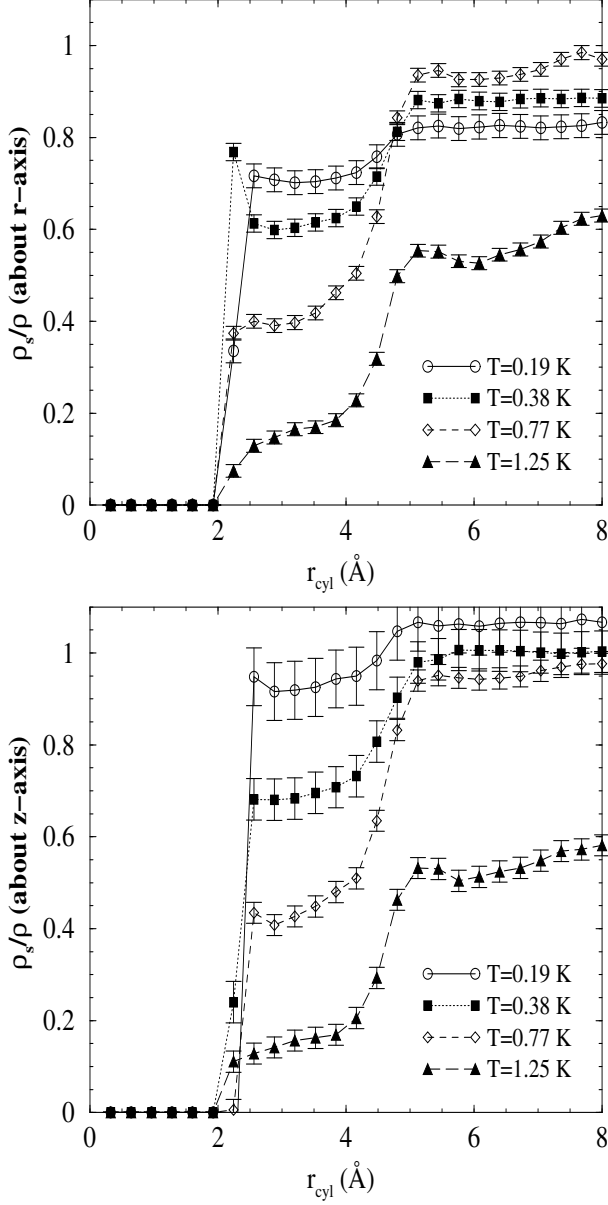


FIG. 8: Superfluid density fraction distributions, averaged over the cylindrically-symmetric region of an  $N = 128$   $^4\text{He}-(\text{HCN})_3$  droplet at  $T = 0.19, 0.38, 0.77$ , and  $1.25 \text{ K}$ . The top graph shows superfluid response about the radial axis, the bottom graph shows superfluid response about the molecule axis.

To quantify the reduced superfluid response in the first layer, we averaged over the cylindrically-symmetric re-

gion of the  $^4\text{He}-(\text{HCN})_3$  droplet, defined as the region between  $z = -3.5 \text{ \AA}$  and  $z = 3.5 \text{ \AA}$  (see Fig. 6). The results of this averaging are shown in Fig. 7. Taking the ratio of the superfluid density to the number density clearly shows a reduced superfluid response in the first layer for rotation about both the radial axis and the molecular axis. At zero temperature, there can be no “normal” density for rotation about the molecular axis because of the cylindrical symmetry, so this reduction must be due to thermal excitations.

Shown in Fig. 8 is the temperature dependence of the superfluid density in the first solvation layer, determined for  $N = 128$   $^4\text{He}-(\text{HCN})_3$  droplets at  $T = 0.19, 0.38, 0.77$ , and  $1.25 \text{ K}$ . At first glance, this result appears to contradict known properties of liquid helium; the superfluid density of bulk helium at  $0.75 \text{ K}$  is  $1.000(1)$ . Theoretical studies of pure  $N = 128$  helium clusters show a superfluid transition roughly in agreement with the bulk lambda transition [26]. Pure droplets like those produced for use in scattering experiments, with several thousand atoms at  $T = 0.38 \text{ K}$ , should have a superfluid fraction very close to unity. However, the helium in the first layer coating the impurity molecule more closely resembles a two-dimensional system than a three-dimensional system, because the motion of the helium atoms is restricted by the He-HCN potential to be primarily on the cylindrical surface circumscribing the  $(\text{HCN})_3$  impurity. Two-dimensional helium films have been shown to have a Kosterlitz-Thouless type of superfluid transition at temperatures significantly lower than  $T_\lambda$  [27, 28]. The reduction in the transition temperature is due to the reduced dimensionality, increasing the phase space for long wavelength fluctuations, and the lowering of the “roton” gap. A similar temperature-dependent reduction in the superfluid response of the first layer of helium surrounding the ends of the isomer was not observed.

To extract the average superfluid density fraction in the first layer from the distributions plotted in Fig. 8, we integrate over the superfluid density and number density in the first layer and take the ratio:

$$\frac{\rho_s}{\rho} = \frac{\int_0^{r_1} dr_{\text{cyl}} \rho_s(r_{\text{cyl}})}{\int_0^{r_1} dr_{\text{cyl}} \rho(r_{\text{cyl}})}, \quad (7.2)$$

where  $r_1$  is the position of the density minimum between the first and second solvation layers. The average superfluid density in the first solvation layer as a function of temperature is shown in Fig. 10. The transition is very broad due to the small number of atoms ( $\sim 30$ ) in the first layer. It shows the onset of superfluidity at roughly  $1 \text{ K}$ . The superfluid density about the molecule axis ( $z$ -axis) goes to unity as the temperature goes to zero, as the density is symmetric about this axis. The normal fluid response from rotating about the radial axis ( $r$ -axis) combines both thermal effects and effective normal fluid induced by rotating through the anisotropic



helium density, and because of this, does not go to zero at  $T = 0$  K [22].

We have determined that only a small fraction of the particles in the first layer are localized (not permuting) at  $T=0.38$  K and below, as shown in Fig. 9. Though many of the permutations are between atoms within the same layer, the first layer is not cut off from the rest of the fluid. Below 1 K, the majority of the atoms in the droplet are part of exchange cycles with atoms in both the first layer and the rest of the droplet. However, in terms of excitations, the first layer is well represented as a 2D superfluid.

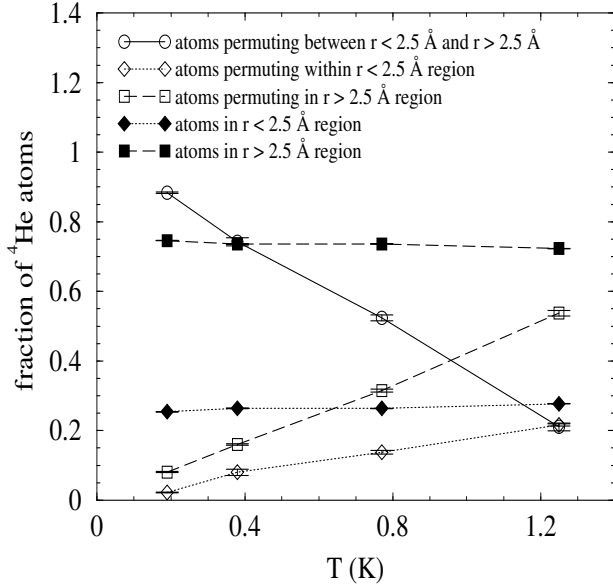


FIG. 9: Exchange behavior of the first layer (defined as  $2.5 \text{ \AA}$  or less from the surface of the  $(\text{HCN})_3$  isomer) as a function of temperature. A permutation cycle was considered to be part of the first layer if more than  $M/2$  consecutive time slices were contained within it, where  $M$  is the number of imaginary time slices per atom.

To compare the effects of density on the thermally-induced normal fluid in the first layer, we calculated the superfluid density distribution for  $N = 128$   $^4\text{He}$ - $(\text{HCN})_3$  droplets at  $T=0.19, 0.38, 0.77$ , and  $1.25$  K, with a  $^4\text{He}$ -HCN interaction reduced by a factor of two in order to reduce the density in the first solvation layer. The density in the first layer decreased by  $\sim 15\%$ , corresponding to an average coverage of  $0.10 \text{ \AA}^{-2}$ . The difference in coverage caused a 20% reduction in the superfluid response about the radial axis at  $T=0.19$  K and  $T=0.38$  K. At higher temperatures, the superfluid response was unchanged within the estimated error bars. The superfluid response about the molecule axis (z-axis) was unchanged within error bars. This is further evidence that the normal response in the first layer is due to both the anisotropy of the molecular potential and thermal excitations.

Using PIMC and a local superfluid density estimator, we find that the first solvation layer surrounding an  $(\text{HCN})_3$  isomer has significant thermal excitations at temperatures as low as  $T=0.19$  K, with a superfluid transition temperature similar to that of a two-dimensional system. It remains to be seen how strongly these thermal excitations are present in droplets with different dopants; this is the first observation of thermal excitations in a helium droplet at such low temperatures. Although we find this effect only makes a small contribution to the moment of inertia of this system, it may explain the anomalous Q branch observed in helium droplets doped with long linear impurities. The role of thermal excitations could also be tested by varying the temperature of the droplet, by adding  $^3\text{He}$  atoms.

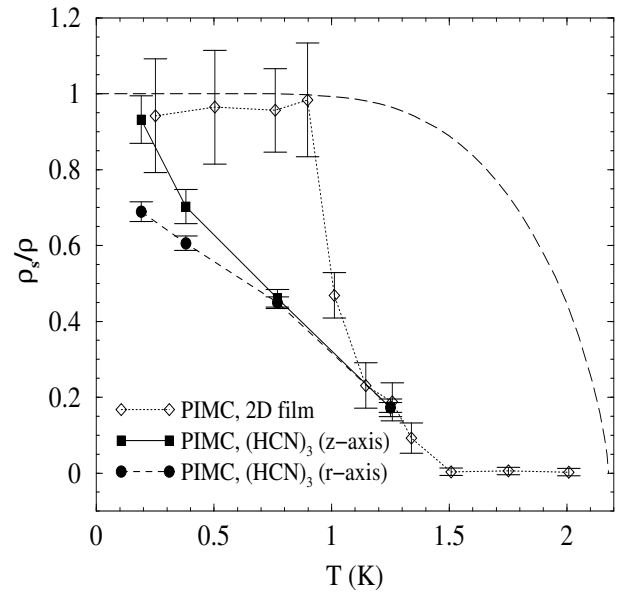


FIG. 10: Superfluid density fraction of the cylindrically-symmetric portion of the first layer of an  $N = 128$   $^4\text{He}$ - $(\text{HCN})_3$  droplet vs. temperature, calculated using Eq. (7.2). The first layer in these systems has an estimated coverage of  $\sigma = 0.12 \text{ \AA}^{-2}$ . Superfluid response about both the molecule axis (solid squares) and radial axis (solid circles) are presented. Also shown are the PIMC results of Gordillo et al (open diamonds), for a 2D  $^4\text{He}$  film with  $\sigma = 0.051 \text{ \AA}^{-2}$ . For reference, the superfluid transition in bulk  $^4\text{He}$  is included (dashed line).

The authors would like to acknowledge K. Lehmann and B. Whaley for useful discussions. The computations were carried out at NCSA and the IBM cluster at the Materials Computation Center, and was supported by the NASA Microgravity Research Division, Fundamental Physics Program. This work was also performed under the auspices of the U.S. Department of Energy by University of California Lawrence Livermore National Laboratory under contract No. W-7405-Eng-48.

- 
- [1] E. W. Draeger and D. M. Ceperley, Phys. Rev. Letts. **89**, 015301 (2002).
  - [2] E. W. Draeger and D. M. Ceperley, Phys. Rev. Lett. **90**, 065301 (2003).
  - [3] H. J. Lauter, H. Godfrin, V. L. P. Frank, and P. Leiderer, Phys. Rev. Lett. **68**, 2484 (1992).
  - [4] D. O. Edwards and W. F. Saam, in *Progress in Low Temperature Physics VII A*, edited by D. F. Brewer (North-Holland, Amsterdam), p. 283, 1978.
  - [5] A. Lastri, F. Dalfovo, L. Pitaevskii, and S. Stringari, J. Low Temp. Phys. **98**, 227 (1995).
  - [6] A. F. G. Wyatt, Nature **391**, 56 (1998).
  - [7] O. Penrose and L. Onsager, Phys. Rev. **104**, 576 (1956).
  - [8] D. S. Lewart, V. R. Pandharipande, and S. C. Pieper, Phys. Rev. B **37**, 4950 (1988).
  - [9] A. Griffin and S. Stringari, Phys. Rev. Letts. **76**, 259 (1996).
  - [10] D. E. Galli and L. Reatto, J. Low Temp. Phys. **113**, 223 (1998).
  - [11] D. E. Galli and L. Reatto, J. Phys. Condens. Matter **12**, 6009 (2000).
  - [12] R. A. Aziz, A. R. Janzen, M. R. Moldover, Phys. Rev. Letts. **74**, 1586 (1995).
  - [13] M. Wagner and D. M. Ceperley, J. Low Temp. Phys. **94**, 161 (1994).
  - [14] D. M. Ceperley, Rev. Mod. Phys. **67**, 279 (1995).
  - [15] W. F. Saam, Phys. Rev. B **12**, 163 (1975).
  - [16] J. E. Gubernatis, M. Jarrell, R. N. Silver, and D. S. Sivia, Phys. Rev. B **44**, 6011 (1991).
  - [17] M. Boninsegni and D. M. Ceperley, J. Low Temp. Phys. **104**, 339 (1996).
  - [18] E. Krotscheck, S. Stringari, and J. Treiner, Phys. Rev. B **35**, 4754 (1987).
  - [19] L. Pitaevskii and S. Stringari, Phys. Rev. B **45**, 13133 (1992).
  - [20] D. M. Ceperley and E. L. Pollack, Can. J. Phys. **65**, 1416 (1987).
  - [21] Grebenev, S., J. P. Toennies and A. F. Vilesov, Science **279**, 2083 (1998).
  - [22] Callegari, C., A. Conjusteau, I. Reinhard, K. K. Lehmann, G. Scoles and F. Dalfovo, Phys. Rev. Lett. **83**, 5058 (1999).
  - [23] Kwon, Y. and K. B. Whaley, Phys. Rev. Lett. **83**, 4108 (1999).
  - [24] Pollack, E. L. and D. M. Ceperley, Phys. Rev. B **36**, 8343 (1987).
  - [25] Bishop, D. J., J. E. Berthold, J. M. Parpia and J. D. Reppy, Phys. Rev. B **24**, 5047 (1981).
  - [26] Sindzingre, P., M. L. Klein and D. M. Ceperley, Phys. Rev. Lett. **63**, 1601 (1989).
  - [27] Ceperley, D. M., and Pollock, E. L., Phys. Rev. B **39**, 2084 (1989).
  - [28] Nyéki, J., R. Ray, V. Maidanov, M. Siqueira, B. Cowan and J. Saunders, J. Low Temp. Phys. **101**, 279 (1995).
  - [29] Gordillo, M. C. and D. M. Ceperley, Phys. Rev. B **58**, 6447 (1998).
  - [30] Kim, K. and W. F. Saam, Phys. Rev. B **48**, 13735 (1993).
  - [31] Nauta, K., private communication (2001).
  - [32] Nauta, K. and R. E. Miller, Science **283**, 1895 (1999).
  - [33] Goyal, S., D. L. Schutt and G. Scoles, Phys. Rev. Lett. **69**, 933 (1992).
  - [34] Pi, M., R. Mayol and M. Barranco, Phys. Rev. Lett. **82**, 3093 (1999).
  - [35] Lehmann, K. K., Mol. Phys. **97**, 645 (1998).
  - [36] Toennies, J. P. and A. F. Vilesov, Annu. Rev. Phys. Chem. **49**, 1 (1998).
  - [37] Atkins, K. M. and J. M. Hutson, J. Chem. Phys. **105**, 440 (1996).
  - [38] Kwon, Y., P. Huang, M. V. Patel, D. Blume and K. B. Whaley, J. Chem. Phys. **113**, 6469 (2000).

## **New propagating mode near the superfluid transition in $^4\text{He}$**

Dmitri A. Sergatskov  
University of New Mexico

We have observed a new temperature-entropy wave that propagates opposite to the direction of a steady heat flux  $Q$  when the helium column is heated from above. This propagating mode is due to non-linear thermoconductance of the helium sample in the self-organized state. Such a mode had been predicted to exist on the self-organized heat transport state for  $Q$  less than about  $100 \text{ nW/cm}^2$ . We confirm that this mode exists in this regime. However, we also observe that it propagates even when the helium is pushed away from the self-organized heat transport state into the normal state.

## **Experiments with helium-4 heated from above, very near the lambda point**

D.A.Sergatskov(1), A.V.Babkin(1), S.T.P.Boyd (1), R.A.M.Lee(2) and R.V. Duncan(1,2)

(1) University of New Mexico

(2) Caltech

We describe an experimental setup and a series of experiments with a column of helium-4 heated from above close to its transition to the superfluid state.

## **A 2-D Piston Effect Solution for the Relaxation in the MISTE Cell**

Mark Weilert

Jet Propulsion Laboratory, California Institute of Technology

April 14, 2003

When a large density stratification is no longer a problem in a microgravity environment, one would like to increase the sample size in order to increase the signal-to-noise ratio for a specific heat measurement. To reduce the equilibration time associated with the large sample size, we designed a cylindrical cell containing a stack of plates that separate the bulk fluid into 60 equally thin layers. To understand the thermal behavior of the whole cell, we analyzed the thermal behavior of a 2-D composite system of a cylindrical near-critical fluid layer in contact with a cylindrical copper plate. In this 2-D analysis, the circumference boundary of the two cylindrical layers is subjected to a step temperature change. The solution of this 2-D composite system includes the piston effect that speeds up the equilibration in the near-critical fluid layer and the pure diffusion in the copper plate. The results of this analysis indicate that the characteristic length for the equilibration of the stacked cell is determined by an effective thickness of a single fluid layer instead of the total height of the cylindrical cell.

## Measurement of Specific Heat Using a Gravity Cancellation Approach

Fang Zhong

Jet Propulsion Laboratory, California Institute of Technology

April 14, 2003

The specific heat at constant volume  $C_v$  of a simple fluid diverges near its liquid-vapor critical point. However, gravity-induced density stratification due to the divergence of isothermal susceptibility hinders the direct comparison of the experimental data with the predictions of renormalization group theory. In the past, a microgravity environment has been considered essential to eliminate the density stratification.

We propose to perform specific heat measurements of  $^3\text{He}$  on the ground using a method to cancel the density stratification. A  $^3\text{He}$  fluid layer will be heated from below, using the thermal expansion of the fluid to cancel the hydrostatic compression. A 6% density stratification at a reduced temperature of  $10^{-5}$  can be cancelled to better than 0.1% with a steady 1.7  $\mu\text{K}$  temperature difference across a 0.05 cm thick fluid layer. A conventional AC calorimetry technique will be used to determine the heat capacity. The minimized bulk density stratification with a relaxation time 6500 sec at a reduced temperature of  $10^{-5}$  will stay unchanged during 1 Hz AC heating. The smear of the specific heat divergence due to the temperature difference across the cell is about 0.1% at a reduced temperature of  $10^{-6}$ . The combination of using High Resolution Thermometry with a 0.5 nK temperature resolution in the AC technique and the cancellation of the density stratification will enable  $C_v$  to be measured down to a reduced temperature of  $10^{-6}$  with less than a 1% systematic error.